FERMILAB-THESIS-2023-09

MEASUREMENT OF THE TOTAL CROSS-SECTION OF MUON NEUTRINO CHARGED-CURRENT COHERENT PION PRODUCTION IN NOVA NEAR DETECTOR

by

Kuruppumullage Don Chatura Dilshan Kuruppu

Bachelor of Science (Honours)
University of Colombo 2012

Submitted in Partial Fulfillment of the Requirements

for the Degree of Doctor of Philosophy in

Physics

College of Arts and Sciences

University of South Carolina

2023

Accepted by:

Roberto Petti, Major Professor

Jonathan Paley, Committee Member

Alexey Petrov, Comittee Member

Pawel Mazur, Comittee Member

Ann Vail, Dean of the Graduate School

DEDICATION

To my dear wife, Chethana Johannas who made many sacrifices for the sake of love including her graduate studies to see my success. The U.S. Embassy in Sri Lanka denied her student VISA multiple times even after getting accepted by the Western Illinois University under article 214(b) because I was taking longer time to graduate. My PhD thesis is based on the NOvA experiment and was made to run roughly 15 years.

Acknowledgments

I would like to express my heartfelt gratitude and appreciation for your invaluable contributions towards the successful completion of my PhD thesis. Your guidance, support, encouragement, and expertise have been instrumental in shaping my research journey.

To the NOvA collaborators, I am immensely grateful for the opportunity to work alongside such a passionate group of scientists. Your knowledge and collaboration have been critical in advancing our understanding of neutrino oscillations and the properties of the neutrino. It has been an honor to be a part of such a collaborative and dynamic research team.

To my Ph.D. committee, I am grateful for your guidance, feedback, and expertise throughout the entire process of my doctorate studies. My Ph.D. supervisor: Prof. Roberto Petti for all your motivations, pushing me towards completion when I was hit at the lowest point of my life. I would also like to thank Dr. Jonathan Paley from Fermi National Laboratory for directing me to right resources to get help and answers in an efficient manner. Prof. Matthias Schindler and Prof. Alexey Petrov for everything you have done to make sure I get paid to continue this important research work. I appreciate the time and effort you dedicated to reading and providing constructive feedback on my thesis.

In conclusion, I would like to thank each and every one of you for your unwavering support and encouragement. I am honored and grateful to have had the opportunity to work with such outstanding individuals, and I will carry the knowledge and skills I gained with me throughout my career.

ABSTRACT

Charged Current (CC) coherent neutrino-nucleus pion production is characterized by small momentum transferred to the nucleus, which is left in its ground state. Despite the relatively large uncertainties on the production cross-section, coherent production of mesons by neutrinos represents an important process, as it can shed light on the structure of the weak current and can also constitute a potential source of background for modern neutrino oscillation experiments and searches for Beyond Standard Model (BSM) physics. This Ph.D. thesis presents a new measurement of CC coherent pion production in the NOvA near detector at the Fermi National Accelerator Laboratory (Fermilab). The analysis is based on the use of both particle identification and kinematic selection criteria based on Convolutional Neural Networks (CNN) to achieve a selection purity of 60%. Given the energy range 1-5 GeV accessible with the available NOvA exposure in the NuMI beam, the results will also be relevant for future neutrino experiments like the Deep Underground Neutrino Experiment (DUNE).

TABLE OF CONTENTS

List of Tables

LIST OF FIGURES

Chapter 1

Introduction to Neutrino Physics

1.1 Standard Model Physics

The Standard Model (SM) is the most established theoretical model, which describes the interaction between the elementary particles at the most fundamental level and could explain almost all the experimental data observed. The Standard Model contains two types of particles: bosons and fermions.

1.1.1 Bosons

Bosons are elementary particles with integer spins that satisfy the Bose-Einstein statistics. In the SM these are of two types (a) vector gauge bosons with spin one (gluon (g), photon (γ), $W^{\pm}$, Z^{0}) and (b) scalar Higgs boson with spin zero. The gluon is a massless vector boson that mediates strong interaction. Quantum chromodynamics (QCD) is the theory of strong force with the coupling strength represented by the QCD coupling constant α_s. This interaction is responsible for the strong binding of quarks inside the hardons. The strong force, as well as the electromagnetic, weak, and gravitational forces, are the four elemental forces of our nature. Electromagnetic interactions can be well explained by quantum electrodynamics (QED) and the corresponding coupling strength is represented in terms of the fine structure constant (α). The massless photon is the carrier of this interaction. The mediators for weak force are the $W^{\pm}$ and Z^{0} bosons. This interaction allows quarks to change their flavors with each other. The strength of this force is represented by the Fermi constant (G_F). The gravitational force is the weakest fundamental force and is mediated by gravitons. Graviton is an exceptional hypothetical gauge boson with spin 2, which is not part of the SM and has no experimental proof so far. A summary of the fundamental interactions is presented in 8.4.

Table 1.1 Summary of fundamental interactions in the SM.

Forces	Gauge Group	Mediator	Range (m)	Coupling Strength
Strong	$SU(3)_C$	gluon	$\leq 10^{-15}$	<1
Electromagnetic	U(1)Y	Photon	infinity	1/137
Week	$SU(2)_L$	$W^{\pm}$, Z^0	10^{-18}	10^{-6}
Gravitational	...	graviton	infinity	10^{-39}

Glashow, Salam, and Weinberg unified the electromagnetic and weak forces [1–3] into the electroweak interaction, which again combines with the strong interaction to form a single unifying model, named the Standard Model. SM is represented by the $SU(3)_C \times SU(2)_L \times U(1)_Y$ gauge group, where $SU(3)_C$ is for strong interaction, where C stands for color charge, $SU(2)_L$ is for weak interaction, where L implies the coupling of $W^{\pm}$, Z^0 bosons with only left-handed fermions, and $U(1)_Y$ stands for hypercharge interaction with $Y = 2(Q - T3)$ as hypercharge. The masses of the fermions and bosons are measured experimentally. However, the SM gauge symmetry imposes on the SM particles that they are massless. Then, how do $W^{\pm}$, Z^0 bosons get mass? The answer to this puzzle is the Higgs mechanism [4–7], where spontaneous symmetry breaking of $SU(2)_L \times U(1)_Y \rightarrow U(1)_{em}$ occurs. As a result of the symmetry breaking, the vacuum expectation value (VEV) of the Higgs scalar field is found to be zero, which will give masses to the weak gauge bosons. The interactions of the Higgs scalar field with fermions provide masses for them. This Higgs field, which was discovered in 4th July 2012 by the ATLAS and CMS Collaboration [8, 9]. In Table 1.2, we list the properties of SM particles in the $SU(3)_C \times SU(2)_L \times U(1)_Y$ gauge group.

1.1.2 Fermions

Fermions are odd half-integral spin subatomic particles that make up matter and obey Fermi-Dirac statistics. These are further categorized into quarks and leptons, which are elementary particles with no substructure. Each group of leptons and quarks is classified into three generations.

Quarks

There exist six flavors of quarks, namely, up (u), down (d), charm (c), strange (s), top (t) and bottom (b). Quarks of different flavors combine with each other to form hadrons, which in general are of two types (a) baryons, which have a triquark state and (b) mesons, which are made up of a quark and an antiquark. Baryons are associated with baryon quantum numbers, which should be conserved in the SM. The problem arising in the triquark state associated with the Pauli-exclusion principle gave birth to a new quantum number called a “color charge, which is of three types, namely red (R), green (G), and blue (B). The corresponding antiquarks have anticolors as the composite particles should be colorless.

Leptons

Similarly to quarks, leptons also have six flavors which consist of charged leptons namely electron (e), muon (μ), tau (τ) and the corresponding neutral leptons known as electron neutrino (ν_e), muon neutrino (ν_μ), tau neutrino (ν_τ). Leptons are color-singlet and do not carry any color quantum number. Each family of leptons is linked to the corresponding lepton number L_i.

1.2 Physics Beyond Standard Model

Though the SM of elementary particle physics is a profound and proficient theory, it fails to explain many physical phenomena like matter-antimatter asymmetry, neutrino

Table 1.2 Quantum numbers of SM particles under gauge symmetry $SU(3)_C \times SU(2)_L \times U(1)_Y$.

	Fields	$SU(3)_C$, $SU(2)_L$, $U(1)_Y$
Leptons	$L_L = \begin{pmatrix} e \\ \nu_e \end{pmatrix}_L, \begin{pmatrix} \mu \\ \nu_\mu \end{pmatrix}_L, \begin{pmatrix} \tau \\ \nu_\tau \end{pmatrix}_L$ e_R, μ_R, τ_R	(1, 2,-1/2) (1, 1,-1)
Quarks	$\begin{pmatrix} u \\ d \end{pmatrix}_L, \begin{pmatrix} c \\ s \end{pmatrix}_L, \begin{pmatrix} t \\ b \end{pmatrix}_L$ u_R, c_R, t_R d_R, s_R, b_R	(3, 2, 1/6) (3, 1, 2/3) (3, 1, -1/3)
Higgs	H	$(1, 2, 1)$

mass, and gravitational force, and it does not have any component of dark matter and dark energy etc. These failures of SM imply that there should be new physics beyond SM. The most general demerits of SM include the following unresolved puzzles:

- The elementary particles are organized into three families. But there is no proper reason for the existence of only 3 generations. So, an interesting question arises here: 'Why are there only three families of leptons and quarks?'

- We do not have any idea of why the masses of third-generation particles are more massive than that of the second-generation, which has a comparatively higher mass than the first-generation fundamental particles of the universe. Thus, the next puzzle of the SM is 'why is there a mass hierarchy?'

- Though an equal amount of particle and antiparticle was produced during the time of big-bang, the existence of stars, galaxies and our Universe implies the dominance of matter over antimatter. Here the most existing question arises, "Why the present universe is matter dominated?".

- SM does not have any explanation for the gravitational force, which is the fourth fundamental interaction of nature.

- The components of dark matter and dark energy are absent in the SM, though 95% of our universe belongs to the invisible sector.
- Although neutrinos are massless in the SM, the confirmation of oscillation between different flavors of neutrino implies that they have masses.

These open questions forced physicists to think beyond the SM. Now, theoreticians are building new physics models in order to resolve these problems. Besides these open puzzles, there are many issues in the neutrino sector, which we are going to discuss in the next chapter.

1.3 Overview of Neutrino Physics

Neutrinos, which are among the numerous subatomic particles in the standard model, have a significant presence in our universe. They came into existence soon after the Big Bang and continue to be generated by supernova explosions, star deaths, and nuclear reactions on Earth. Despite approximately one hundred trillion neutrinos passing through our bodies every second, we have limited knowledge of their behavior. As the lightest colorless fermions lack an electric charge, neutrinos only interact weakly with other SM fermions through weak interaction. This weak interaction makes neutrinos the least understood of all fundamental particles. It was not until the emergence of beta-decay puzzles that the scientific community began to uncover the mysteries surrounding neutrinos.

1.3.1 History of Neutrinos

The area of neutrino physics started with the proposal of the existence of a new hypothetical neutral fermion by the theorist Wolfgang Pauli in 1930. Before the prediction on neutrino, beta decay was considered to be a two-body decay process;

$$n^0 \rightarrow p^+ + e \tag{1.1}$$

Since the daughter nuclei are almost at rest, one should expect a discrete energy spectrum for the electron particle due to the energy conservation. However, the distribution of electron energy values is found to be continuous. Furthermore, the direction of the recoiling nuclide was not completely opposite to the direction of the emitted electron. Thus, if beta decay is assumed to be a two-body process, the energy-momentum is not conserved in this process. Since anti-electron neutrino with spin half react and produce two spin half fermions in the nuclear reactor united with protons, creating neutron and positron:

$$\bar{\nu}_e + p^+ \rightarrow n^0 + e^+ \tag{1.2}$$

Afterward, the pair annihilation process occurs, i.e., the positron combines with an electron to produce two gamma rays,

$$e^+ + e^- \rightarrow \gamma + \gamma \tag{1.3}$$

and the neutron is captured by the cadmium nuclei producing a photon

$$n + Cd^{108} \rightarrow Cd^{109} + \gamma \tag{1.4}$$

This was the first experiment, where the anti-electron neutrino was detected, for which Reines and Cowan won the Nobel Prize in 1995. After the observation of K0 mixing in the quark sector, Pontecorvo proposed the possibility of neutrino mixing in 1957. In 1962, a new type of neutrino was discovered at Brookhaven National Laboratory (BNL), showing different behaviors with electrons and muon. This was the discovery of the second neutrino, known as muon neutrino ν_μ for which Lederman, Schwartz, and Steinberger received the Nobel Prize in 1988. Just after the discovery of muon neutrinos, Maki and Sakata developed the theory of oscillation in 1962.

Thereafter, the DONUT experiment has discovered the tau neutrino 2000. In 2015, Takaaki Kajita and Arthur B. McDonald, and others have been awarded the Nobel Prize for their contribution to the discovery of neutrino oscillations, which showed that neutrinos have mass.

1.3.2 Neutrino Oscillations

Neutrinos come in three flavors, and they change flavor as they travel from one place to another irrespective of means by means of the medium through the earth or vacuum. The amount they change depends on how long they have to change. This time is directly related to the distance of the neutrino traveled and the energy of the neutrino itself. Distance is much easier to measure than neutrino energy estimation. Neutrino oscillations occur because neutrino flavor states are a quantum superposition of mass eigenstates.

$$|\nu_\alpha\rangle = \sum_i U_{\alpha i} |\nu_i\rangle \tag{1.5}$$

where, $|\nu_\alpha\rangle$ is the flavor eigenstate, with $\alpha = e, \mu, \tau$ and $|\nu_i\rangle$ is the mass eigenstate and i = 1,2,3. In quantum mechanics, the neutrino can be described either in flavor bases or in mass basis. They are related to a unitary leptonic mixing matrix $U_{\alpha i}$, commonly known as Pontecorvo-Maki-Nakagawa-Sakata (PMNS) matrix. In general, the relation can be written as follows:

$$\begin{pmatrix} \nu_e \\ \nu_\mu \\ \nu_\tau \end{pmatrix} = U \begin{pmatrix} \nu_1 \\ \nu_2 \\ \nu_2 \end{pmatrix} \tag{1.6}$$

1.3.3 Neutrino Oscillations in Vacuum

Let us consider a given neutrino source at position x = 0, and time t = 0. After a certain distance of travel by neutrinos, let us say the position and time are x and t, respectively. One can obtain the evolution of neutrino mass state in time using the Schrodinger equation. The solution of the equation provides a plane wave equation associated with a phase. The mass eigenstate of the neutrino at a point in space-time (x, t) is given by

$$|\nu_\alpha(x,t)\rangle = \sum_{i=1}^{n} U_{\alpha i} |\nu_i(x,t)\rangle = \sum_{i=1}^{n} U_{\alpha i} e^{-i\phi_1} |\nu_i(0,0)\rangle \tag{1.7}$$

Here, ϕ is the phase. The transition amplitude A can be written for α neutrino flavor at space-time (0,0) to β neutrino flavor at later space-time (x,t) is:

$$\begin{aligned} A(\nu_\alpha \to \nu_\beta) &= \langle \nu_\beta(x,t) | \nu_\alpha(x,t) \rangle \\ &= \sum_{i=1}^{n} \sum_{j=1}^{n} U^*_{\beta j} U_{\alpha i} \langle \nu_j(x,t) | \nu_i(0,0) \rangle \\ &= \sum_{i=1}^{n} U_{\alpha i} U^*_{\beta,i} e^{i\phi_i} \end{aligned} \tag{1.8}$$

The transition probability is:

$$\begin{aligned} P_{\alpha,\beta} &= |A(\nu_\alpha \to \nu_\beta)|^2 \\ &= \left| \sum_{i=1}^{n} U_{\alpha i} U^*_{\beta,i} e^{i\phi_i} \right|^2 \\ &= \sum_{i=1}^{n} \sum_{j=1}^{n} U_{\alpha i} U^*_{\beta i} U^*_{\alpha j} U_{\beta j} e^{-i(\phi_j - \phi_i)} \end{aligned} \tag{1.9}$$

Considering neutrino a relativistic particle, the energy E_i of neutrino mass eigenstates ν_i, with mass m_i, can be approximated as:

$$E_i = \sqrt{p_i^2 + m_i^2} \simeq p + \frac{m_i^2}{2E} \tag{1.10}$$

The phase difference tells us about the neutrino mass splitting:

$$\phi_i - \phi_j = (E_i - E_j)\, L - (p_i - p_j)\, x = \frac{\Delta m^2_{ij} L}{2E} \tag{1.11}$$

where:

$$\Delta m^2_{ij} = m_i^2 - m_j^2 \tag{1.12}$$

If the neutrino has two flavors, they are related to a rotation matrix and θ is the mixing angle.

$$U = \begin{pmatrix} \cos\theta & \sin\theta \\ -\sin\theta & \cos\theta \end{pmatrix} \tag{1.13}$$

The oscillation probability of a neutrino ν_α oscillates into ν_β for the two flavor neutrinos is:

$$\mathrm{P}_{\nu_\alpha \to \nu_\beta}\left(\mathrm{E}_\nu\right) = \sin^2 2\theta \sin^2\left(\frac{1.27\Delta m^2_{21}\ \mathrm{L}}{4\mathrm{E}_\nu}\right) \tag{1.14}$$

The probability of neutrino oscillation depends on the L / E ratio and the sinusoidal function. From Eq 1.14 it is evident that neutrino oscillations are actually implying neutrino masses within the measured energy region. If the mass squared difference is zero, the oscillation probability is zero, implying the existence of at least one nonzero neutrino mass state. So far, we have experimentally observed only a mass-squared difference, not the absolute mass of the neutrino. Furthermore, Δm^2 is involved in the sin square, which means that there is no sensitivity of the sign of Δm^2. Again, the mixing angle is involved in terms of $sin^2 2\theta$, in the two-flavor framework, the oscillation amplitude is the same for the mixing angle 40^0 or 50^0. But they resulted differently in the three neutrino oscillation frameworks. Extending the two-flavor neutrino oscillation to the three-flavor oscillation, the 3×3 unitary PMNS matrix U can be expressed as:

$$U = \begin{pmatrix} c_{13}c_{12} & c_{13}s_{12} & s_{13}e^{-i\delta} \\ -c_{23}s_{12} - s_{23}c_{12}s_{13}e^{i\delta} & c_{23}c_{12} - s_{23}s_{12}s_{13}e^{i\delta} & c_{13}s_{23} \\ s_{23}s_{12} - c_{23}c_{12}s_{13}e^{i\delta} & -s_{23}c_{12} - c_{23}s_{12}s_{13}e^{i\delta} & c_{13}s_{23} \end{pmatrix} \tag{1.15}$$

where: $c_{ij} = \cos\theta_{ij}\ and\ s_{ij} = \sin\theta_{ij}$.

One more interesting feature is that charge-parity (CP) violation comes into the picture in the three-flavor neutrino oscillation framework and it is not seen in the two-flavor case. The transition probability of a neutrino ν_α oscillates into ν_β for a

3-flavor neutrino can be expressed using 3 × 3 unitary PMNS matrix U_{ij} as:

$$\begin{aligned} P_{\nu_\alpha \to \nu_\beta} &= \delta_{\alpha\beta} - 2 \sum_{i>j} \mathrm{Im}\left[U^\star_{\beta j} U_{\alpha j} U_{\beta i} U^\star_{\alpha i}\right] \sin \frac{\Delta m^2_{ji} L}{2E} \\ &+ 4 \sum_{i>j} \mathrm{Re}\left[U^\star_{\beta j} U_{\alpha j} U_{\beta i} U^\star_{\alpha i}\right] \sin^2 \frac{\Delta m^2_{ji} L}{4E} \end{aligned} \tag{1.16}$$

1.3.4 Neutrino Oscillations in Matter

When electron neutrinos propagate through matter they interact with the electron content of the matter because neutrinos interact with their corresponding leptons. Electron neutrinos interact with electrons in matter under both charged and neutral current processes, but for other flavors, only neutral current interactions are possible. Thus, the flavor experiences an asymmetric potential, the so-called Wolfenstein term, which is popularly known as the Mikheyev- Smirnov-Wolfenstein (MSW) effect [10]. For simplicity, starting with 2-flavor, the MSW effect can be expressed according to the Schrodinger equation:

$$\begin{aligned} i\frac{d}{dL}\begin{pmatrix} \nu_e \\ \nu_\mu \end{pmatrix} &= \left(U \begin{pmatrix} \frac{m_1^2}{2E} & 0 \\ 0 & \frac{m_2^2}{2E} \end{pmatrix} U^* + V_{cc} \begin{pmatrix} 1 & 0 \\ 0 & 0 \end{pmatrix} \right) + \begin{pmatrix} \nu_e \\ \nu_\mu \end{pmatrix} \\ &= \frac{1}{4E} \begin{pmatrix} -\Delta m^2 \cos 2\theta + 4EV_{cc} & \Delta m^2 \sin 2\theta \\ \Delta m^2 \sin 2\theta & \Delta m^2 \cos 2\theta \end{pmatrix} \begin{pmatrix} \nu_e \\ \nu_\mu \end{pmatrix} \end{aligned} \tag{1.17}$$

where $V_{cc} = \pm\sqrt{2} G_F \rho_e$, G_F is the Fermi constant, ρ_e is the electron number density, and the positive and negative signs are for neutrinos and anti-neutrinos, respectively.

The effective Hamiltonian in the mass basis can be derived from the diagonalization of the effective Hamiltonian in the flavor basis through a unitary matrix:

$$U_M^T \mathcal{H}_F U_M = \mathcal{H}_M \tag{1.18}$$

Here, $\mathcal{H}_F$ is effective Hamiltonian flavor basis, U_M is the effective mixing matrix in matter:

$$U_M = \begin{pmatrix} \cos\theta_M & \sin\theta_M \\ -\sin\theta_M & \cos\theta_M \end{pmatrix} \tag{1.19}$$

and $\mathcal{H}_M$ is effective Hamiltonian in mass basis, expressed as:

$$\mathcal{H}_M = \frac{\Delta m^2}{4E} \begin{pmatrix} -1 & 0 \\ 0 & 1 \end{pmatrix} \tag{1.20}$$

Simplifying Eq 1.20 and Eq 1.19, the effective mass-squared differences and mixing angles can be expressed as:

$$\Delta m_M^2 = \sqrt{\left(\Delta m^2 \cos 2\theta \mp 2EV_{cc}\right)^2 + \left(\Delta m^2 \sin 2\theta\right)^2} \tag{1.21}$$

$$\tan 2\theta_M = \frac{\tan 2\theta}{1 \mp \frac{2EV_{cc}}{\Delta m^2 \cos 2\theta}} \tag{1.22}$$

where Δm^2 and θ represent the split and mixing angle in vacuum. The matter effect modifies the oscillation parameters on the basis of the matter density and neutrino energy. When $cos 2\theta = 2EV_{cc}$ it is found that $\Delta m_M^2 = \Delta m^2$, which leads to resonance. This resonance corresponds to the electron number density as:

$$\begin{aligned} V_{cc} &= \sqrt{2} G_F \rho_e \\ &= \frac{\Delta m^2 \cos 2\theta}{2E} \\ \rho_{res} &= \frac{\Delta m^2 \cos 2\theta}{2\sqrt{2} G_F E} \end{aligned} \tag{1.23}$$

At resonance, the effective mixing angle becomes maximal (45^0) which leads to an amplification of the oscillation probabilities. The matter effect will be significant if neutrinos pass through more dense material, for example, at the core of the Sun. This method is used to fix the mass ordering of neutrinos in solar neutrino mixing and long-baseline neutrino oscillation experiments to find the mass ordering of ν_3. Furthermore, as positive and negative signs denote neutrino and antineutrino, respectively, the oscillation probability will also be different, so there is an expected charge-parity asymmetry. The oscillation probability for muon neutrinos oscillating into electron neutrinos is:

$$\begin{aligned}
P_{\nu_\mu \to \nu_e} &= \sin^2\theta_{23}\sin^2 2\theta_{13}\frac{\sin^2\left(\Delta m^2_{31} \mp aL\right)}{\left(\Delta m^2_{31} \mp aL\right)^2}\Delta m^4_{31} \\
&+ \sin 2\theta_{23}\sin 2\theta_{13}\sin 2\theta_{12}\frac{\sin\left(\Delta m^2_{31} \mp aL\right)}{\left(\Delta m^2_{31} \mp aL\right)}\Delta m^2_{31}\frac{\sin(\mp aL)}{(\mp aL)}\Delta m^2_{21} \\
&\Big(\cos\Delta m^2_{32}\cos\delta \mp \sin\Delta m^2_{32}\sin\delta\Big) \\
&+ \cos^2\theta_{23}\sin^2 2\theta_{12}\frac{\sin^2(\mp aL)}{(\mp aL)^2}\Delta m^4_{21}
\end{aligned} \tag{1.24}$$

where $a = \frac{G_F \rho_e}{\sqrt{2}}$ and the signs minus and plus are for neutrinos and antineutrinos, respectively.

1.3.5 Importance of Cross-section

Neutrino oscillation experiments do not measure the oscillation probability, but rather the event rate. Therefore, we need to measure the number of neutrinos as a function of the neutrino energy at near and far detectors. The number of neutrinos at the near detector is the convolution of flux, cross-section, and detection efficiency of the near detector:

$$\mathrm{N}^{\mathrm{ND}}_{\nu_\alpha}\left(\mathrm{E}_\nu\right) \propto \phi\left(\mathrm{E}_\nu\right) \times \sigma\left(\mathrm{E}_\nu\right) \times \epsilon^{\mathrm{ND}}\left(\mathrm{E}_\nu, \mathrm{T}_\alpha, \Theta_\alpha \ldots\right) \tag{1.25}$$

The flux ($\phi(E_\nu)$) is defined as the number of neutrinos produced by the accelerator per cm^2, per energy, for a given number of protons on target. The probability of interaction of the neutrinos in the material of the detector is known as the cross-section ($\sigma(E_\nu)$) and efficiency (ϵ) corrects for events which we lose during selection (threshold, acceptance, containment, etc.). Due to the convolution of flux and cross-section, even if there is a high correlation between flux, cross-section, and detector efficiency between near and far detectors, it will not remove all dependencies. The event rate approximately can be written as :

$$\frac{\mathrm{N}^{FD}_{\nu_\beta}}{\mathrm{N}^{ND}_{\nu_\alpha}} \approx \frac{\phi^{FD}_{\nu_\beta}\left(\mathrm{E}_\nu\right)}{\phi^{ND}_{\nu_\alpha}\left(\mathrm{E}_\nu\right)} \times \frac{\sigma^{FD}_{\nu_\beta}\left(\mathrm{E}_\nu\right)}{\sigma^{ND}_{\nu_\alpha}\left(\mathrm{E}_\nu\right)} \times \frac{\epsilon^{FD}_{\nu_\beta}}{\epsilon^{ND}_{\nu_\alpha}} \times \mathrm{P}_{\nu_\alpha \to \nu_\beta}\left(\mathrm{E}_\nu\right) \tag{1.26}$$

The oscillated flux at the far detector is not the same as the un-oscillated flux measured at the near detector, as the far detector sees a point source of neutrino beam, whereas near detector sees a broad spectrum of neutrino source. Also, the acceptance of particles is different at both the near and far detectors, efficiency calculation depends on the simulated particles from an event generator which is based on the neutrino-nucleus interaction model. The dependence of efficiency on the kinematics of the final state, which is driven by cross-section, and the different model predicts different particle multiplicity in the final state, which gives birth to uncertainty. The uncertainty does not cancel exactly due to the difference in the near- and far-detectors.

1.3.6 NEUTRINO KINEMATICS

Before moving on to various neutrino-nucleus interactions, we need to familiarize ourselves with the neutrino kinematics notation, which has widespread use throughout this dissertation. In general, the neutrino interacts with a target nucleus that produces a lepton or neutrino depending on the type of interaction (charged current or neutral current) and a messy final state particle (Figure 1.1). Let us consider the four-momentum of the incoming neutrino $k(E_\nu, \vec{p_\nu})$ and the outgoing leptons be $k'(E_l, \vec{p_l})$, the target nucleus four-momentum $p(E_N, \vec{p_N})$ and the final-state hadrons, $p'(E_H, \vec{p_H})$. q is the four-momentum transferred between the neutrino-lepton system and the square of this transfer (q^2) is Lorentz invariant and is usually used as

$$Q^2 = -q^2 \tag{1.27}$$

which determines what final states are available to an interaction and mostly depends on the neutrino energy.

$$\begin{aligned} q^2 &= (k' - k)^2 \\ &= (E_l - E_\nu)^2 - (\overrightarrow{p_l} - \vec{p}_\nu)^2 \\ &= -Q^2 \end{aligned} \tag{1.28}$$

The energy transfer will be $\nu = E_\nu - E_l$. The fraction of the initial neutrino's energy transferred by the interaction is defined as inelasticity (y) and represented as

$$\begin{aligned} y &= \frac{p \cdot q}{p \cdot k} \\ &= \frac{E_\nu - E_l}{E_\nu}. \end{aligned} \tag{1.29}$$

in the laboratory frame. The fraction of the target nucleon's momentum carried by the quark is termed as Bjorken scaling variable (x) :

$$\begin{aligned} x &= \frac{Q^2}{2p \cdot q} \\ &= \frac{Q^2}{2M_T\nu}, \end{aligned} \tag{1.30}$$

in laboratory frame. where M_T is mass of the target nucleus. The total invariant mass of the outgoing final-state particles is represented by W and can be written as:

$$\begin{aligned} W^2 &= (p + q)^2 \\ &= M_T^2 + 2M_TE_H - Q^2, \end{aligned} \tag{1.31}$$

where E_H is mass of the hadrons.

1.3.7 NEUTRINO NUCLEUS INTERACTION

The neutrino-nucleus interaction largely depends on the energy of the neutrino; the higher the neutrino energy, the better it can reach the small scale of length. We are dealing with two types of interaction such as charged current (CC) and neutral current (NC) interactions. The interaction process in which neutrino is in and charge lepton is out occurs through the exchange of a charged (W) boson. The flavor of

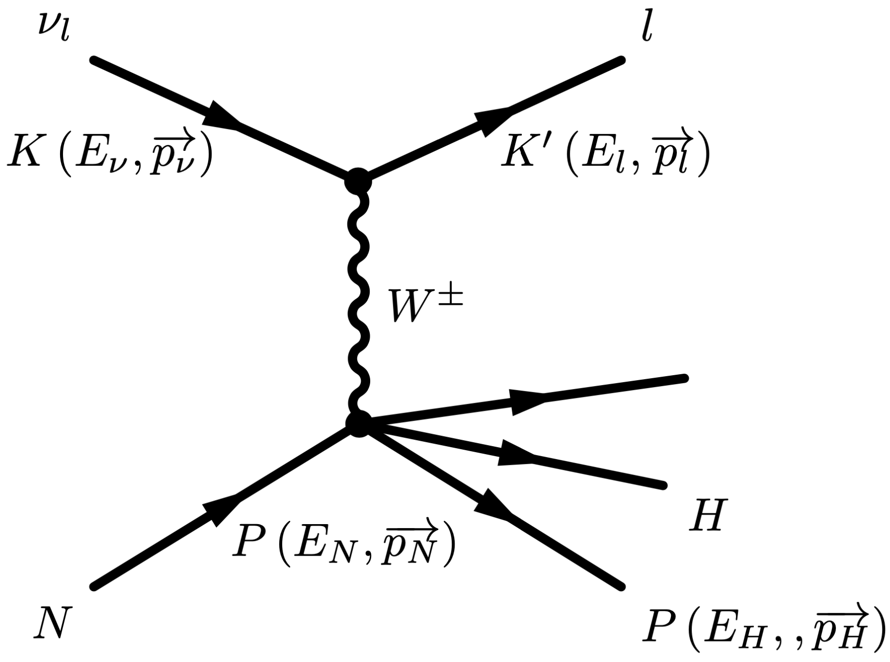

Figure 1.1 The standard neutrino interaction with a target, exiting with a (charged or neutral) lepton and massive hadrons in final state.

the outgoing lepton 'tags' the flavor of the incoming neutrino and the charge of the outgoing lepton determines whether it is neutrino or antineutrino (Figure 1.2). In the NC process, the neutrino is in both the initial and final states since it is mediated by a neutral boson (Z). It is impossible to reconstruct the kinematics of final-state particles in NC interactions, and these typically appear in oscillation measurements as backgrounds.

The inclusive muon neutrino charged-current analysis implies that at least one muon will be among the final-state particles irrespective of the particular interaction process in which it takes care of summing over all possible nuclear final states.

Coherent Scattering (Coh)

Coherent scattering is a process by which a neutrino interacts with a nucleus, the nucleus is not excited to a higher energy state and coherently scatters off the target

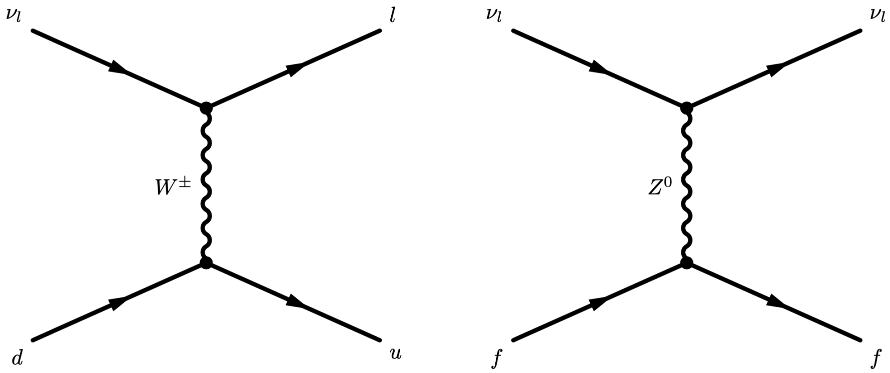

Figure 1.2 Charged Current (left) and Neutral Current (right) neutrino-nucleus interaction process.

nucleus with the small exchange of energy between nucleus and neutrino with single meson (pions, kaons, rho) in the final state. The charge current and neutral current coherent processes are:

$$\begin{aligned} \nu_\mu A \to \mu^- A\pi^+, \bar{\nu}_\mu A \to \mu^+ A\pi^- \\ \nu_\mu A \to \nu_\mu A\pi^0, \bar{\nu}_\mu A \to \bar{\nu}_\mu A\pi^0 \end{aligned} \tag{1.32}$$

The coherent interaction process plays an important role in the $\nu_\mu \to \nu_e$ oscillation analysis. As the final state has π^0, which decays to two photons if any one of the photons is missing from this sample, which can be misidentified as a signal event ν_e. This might occur when a missed photon exits the detector before showering or is not able to produce a shower. Also, the misidentification of charged current coherent π^+ as proton disturbs the reconstruction of neutrino energy in particularly ν_μ disappearance analysis. The coherent scattering process occurs in the low Q^2 region and requires a small momentum transfer to the target nucleus. According to the partially conserved axial current (PCAC) hypothesis, the differential cross section at $Q^2 = 0$ is given by:

$$\left.\frac{d^3\sigma(\nu A \to lA\pi)}{dxdydQ^2}\right|_{Q^2=0} = \frac{G_F^2}{\pi^2} f_\pi^2 M E_\nu (1-y) \left.\frac{\sigma(\pi A \to \pi A)}{dQ^2}\right|_{E_\nu y = E_\pi}, \tag{1.33}$$

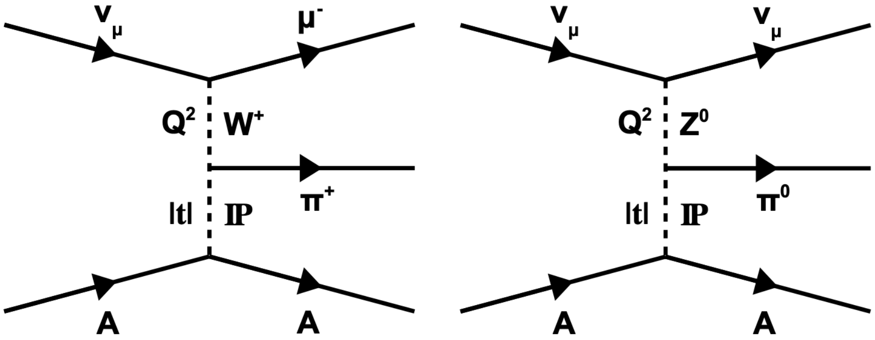

Figure 1.3 CC (left) and NC (right) neutrino-nucleus coherent pion production in the PCAC picture [11].

where x, y are the Bjorken scaling variables, G_F is the weak coupling constant, f is the pion decay constant, M is the mass of the nucleon, and Q^2 is the square of the four-momentum transferred to the target nucleus. At $Q^2 \neq 0$, the cross-section is dipole dependent, and the cross-section is calculated from measured data on total and inelastic pion scattering from protons and deuterium.

RESONANCE PION PRODUCTION (RES)

In this process, meson production is performed in the final state through the excitation of the nucleon into a resonant state. The resonant states are unstable and further decay to mesons and nucleons. A charged lepton is produced in the case of charge current interaction (Figure 1.4). It is more active at the invariant mass W < 2 GeV and contributes more in the neutrino energy range $0.5 - 3$ GeV. The intermediate resonance state is Δ_{33} (1232) in the lower neutrino energy that produces single pions and in the higher neutrino energy range the higher mass resonances are $P_{11}(1440), S_{11}$ (1535) and $D_{13}(1520)$ which decay to multiple pions, kaons, and photons in addition to single pions. Examples of different channels of charge current and neutral current resonance processes are:

$$\nu_\mu n \to \mu^- n\pi^+, \bar{\nu}_\mu p \to \mu^+ p\pi^-$$

$$\nu_\mu n \to \mu^- p\pi^0, \bar{\nu}_\mu p \to \mu^+ n\pi^-$$

$$\nu_\mu p \to \mu^- p\pi^+, \bar{\nu}_\mu n \to \mu^+ n\pi^0$$

$$\nu_\mu p \to \nu_\mu p\pi^0, \bar{\nu}_\mu p \to \bar{\nu}_\mu p\pi^0$$

$$\nu_\mu n \to \nu_\mu n\pi^0, \bar{\nu}_\mu n \to \bar{\nu}_\mu n\pi^0$$

$$\nu_\mu p \to \nu_\mu n\pi^+, \bar{\nu}_\mu p \to \bar{\nu}_\mu n\pi^+$$

$$\nu_\mu n \to \nu_\mu p\pi^-, \bar{\nu}_\mu n \to \bar{\nu}_\mu p\pi^-$$

The double differential cross-section for a single meson production is given by:

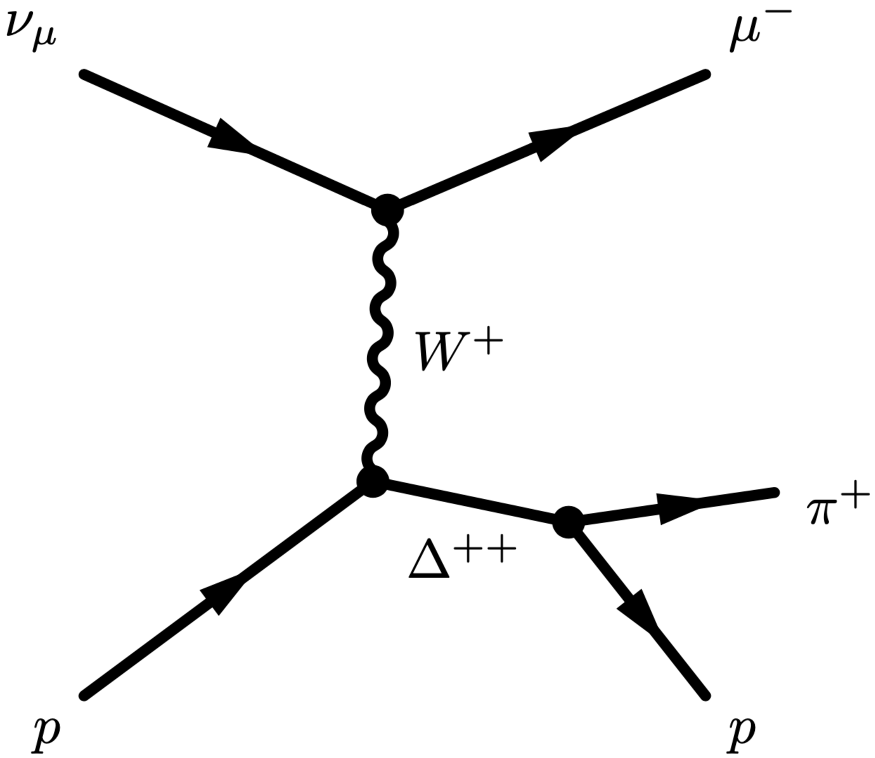

Figure 1.4 Charged current resonance neutrino-nucleus interaction process.

$$\frac{d^2\sigma}{dQ^2 d\nu} = \frac{1}{32\pi M E_\nu^2} \frac{1}{2} \sum_{spins} \left| T\left(\nu N \to l N^*\right) \right|^2 \delta\left(W^2 - M^2\right), \tag{1.34}$$

where M is the mass of the initial state of the nucleon, ν is the energy transfer, $T\left(\nu N \to l N^*\right)$ is the amplitude of a given resonance production, and W is the hadronic invariant mass. The amplitude is calculated using the FKR model [12].

Quasi-elastic Interaction (QE)

The neutrino scatters elastically off the nucleon, ejecting a nucleon from the target and a charged lepton in the final state with an exchange of W boson in the charge current process, whereas, in the anti-neutrino scattering, a proton is converted into a neutron.

$$\begin{gathered} \nu_\mu n \to \mu^- p, \\ \bar{\nu}_\mu p \to \mu^+ n \end{gathered} \tag{1.35}$$

In the charged current interaction process the "quasi" term arises because the neutrino changes its identity to a charged lepton and the neutron can change into a proton by switching from d quark to u quark. In general, the quasi-elastic term refers to the events that are close to the quasi-elastic peak in lepton kinematics. However, for a neutral current process, it is simply termed elastic scattering.

QE interaction plays a central role in the neutrino energy of $\sim$ 2GeV and is commonly used as signal events in many neutrino oscillation experiments operating in this energy range. In this process, a muon can be clearly detected in the final state.

According to Llewellyn-Smith formalism [13] neutrino-nucleon quasi-elastic cross-section is expressed as:

$$\frac{d\sigma}{dQ^2_{QE}} \begin{pmatrix} \nu_l n \to l^- p \\ \bar{\nu}_l p \to l^+ n \end{pmatrix} = \frac{M^2 G_F^2 \cos^2\theta_c}{8\pi E_\nu^2} \left\{ A\left(Q^2\right) \mp B\left(Q^2\right) \frac{s-u}{M^2} + C\left(Q^2\right) \frac{(s-u)^2}{M^4} \right\} \tag{1.36}$$

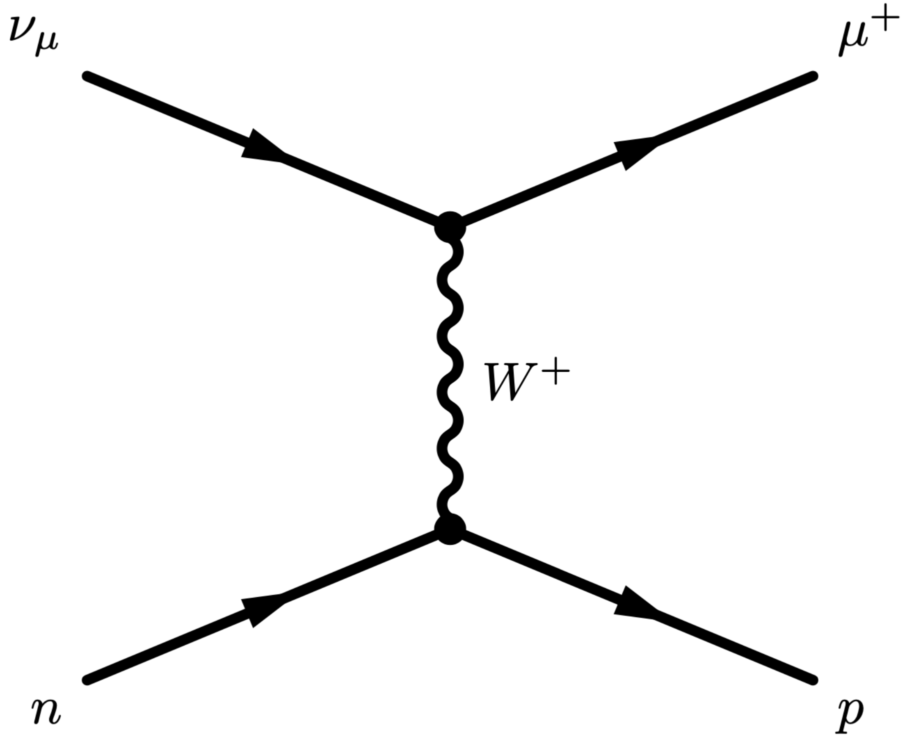

Figure 1.5 Quasi-elastic charged current neutrino-nucleus interaction process.

where the sign of the B term is negative for neutrinos and positive for anti-neutrinos. M is the average nucleon mass (939 MeV).θ_C is the Cabbibo angle ($\cos\theta_C =$ 13 0.9742). Here, s and u are Mandelstam variables. E_ν the incoming neutrino energy. A, B, and C are combinations of hadronic form factors.

$$\begin{aligned}
A\left(Q^2\right) =& \frac{m_\mu^2 + Q^2}{M^2}\left\{\left(1+\frac{Q^2}{4M^2}\right)F_A^2 - \left(1-\frac{Q^2}{4M^2}\right)F_1^2\right.\\
&+\frac{Q^2}{4M^2}\left(1-\frac{Q^2}{4M^2}\right)(\xi F)^2 + \frac{Q^2}{M^2}\operatorname{Re}\left(F_1^*\xi F_2\right) - \frac{Q^2}{M^2}\left(1+\frac{Q^2}{4M^2}\right)\left((F)_A^3\right)^2 -\\
&\left.\frac{\mu^2}{4M^2}\left[\left|F_1+\xi F_2\right|^2 + \left|F_1+2F_p\right|^2 - 4\left(1+\frac{Q^2}{4M^2}\right)\left(\left((F)_A^3\right)^2 + F_p^2\right)\right]\right\}\\
B\left(Q^2\right) =& \frac{Q^2}{M^2}\operatorname{Re}\left[F_A^*\left(F_1+\xi F_2\right)\right] - \frac{\mu^2}{M^2}\operatorname{Re}\left[\left(F_1-\tau\xi F_2\right)F_V^{3*} - \left(F_A^* - \frac{Q^2}{2M^2}F_p\right)F_A^3\right],\\
C\left(Q^2\right) =& \frac{1}{4}\left\{F_A^2 + F_1^2 + \tau\left(\xi F_2\right)^2 + \frac{Q^2}{M^2}\left(F_A^3\right)^2\right\}
\end{aligned} \tag{1.37}$$

Out of six form factors, two are vector (F_1 and F_2), an axial vector (F_A), a pseudoscalar (F_P), and two small second-order terms (F_A^3 and F_V^3).

The vector form factors (F_1 and F_2) can be expressed considering the conserved vector current hypothesis (CVC) [14], [15] in terms of the form factors.

$$\begin{aligned} F_1\left(Q^2\right) &= \frac{G_E^V\left(Q^2\right)+\frac{Q^2}{4M^2}G_M^V\left(Q^2\right)}{1+\frac{Q^2}{4M^2}}. \\ \xi F_2\left(Q^2\right) &= \frac{G_M^V\left(Q^2\right)-G_E^V\left(Q^2\right)}{1+\frac{Q^2}{4M^2}} \end{aligned} \tag{1.38}$$

where G_M^V and G_E^V are the electron scattering form factors and are represented by

$$\begin{aligned} G_E^V\left(Q^2\right) &= G_E^p\left(Q^2\right)-G_E^n\left(Q^2\right), \\ G_M^V\left(Q^2\right) &= G_M^p\left(Q^2\right)-G_M^n\left(Q^2\right), \end{aligned} \tag{1.39}$$

where G_E^p and G_E^m are the electric form factors of the proton and neutron, G_M^p and G_M^n are the magnetic form factors of the proton and neutron. The behavior of the form factor changes according to Q^2 and can be measured by electron scattering experiments. When $Q^2 = 0$, the electric form factors correspond to the electric charge of the proton (1) and neutron (0), however, the magnetic form factors correspond to the magnetic moments of the proton and neutron. At $Q^2 > 0$, the form factors are determined via dipole approximation, and nucleon charge is distributed exponentially $\rho(r) = \rho_0 e^{-Mr}$ and the dipole form factor can be obtained from Fourier transformation as:

$$\begin{aligned} G_D\left(Q^2\right) &= \frac{1}{\left(1+\frac{Q^2}{4M_V^2}\right)^2}, \\ G_E^p\left(Q^2\right) &= G_D\left(Q^2\right), \\ G_E^n\left(Q^2\right) &= 0, \\ G_M^p\left(Q^2\right) &= \mu_p G_D\left(Q^2\right), \\ G_M^n\left(Q^2\right) &= \mu_n G_D\left(Q^2\right), \end{aligned} \tag{1.40}$$

where M is the mass of the nucleon, M_V is the vector mass = 0.843 GeV $\cdot \mu_p = 2.79$ and $\mu_n = -1.91$ are the magnetic moments of the proton and neutron, respectively.

The pseudo-scalar form factor (F_V) is related to the axial form factor (F_A) and can be expressed as

$$\begin{aligned} F_P\left(Q^2\right) &= \frac{2M^2}{Q^2+m_\pi^2} F_A\left(Q^2\right), \\ F_A\left(Q^2\right) &= \frac{g_A}{\left(1+\frac{Q^2}{M_A^2}\right)^2}, \end{aligned} \tag{1.41}$$

F_A is parameterized as a dipole. The average axial mass constant $M_A = 1.014 \pm 0.014\mathrm{GeV/c}^2$ was extracted by Bodek et al. [16] and the best axial vector constant $g_A = 1.267$ and is known from beta decay experiments. More details of M_A can be found in Ref. [17].

Deep-inelastic Scattering (DIS)

In this interaction process, the neutrino scatters a quark in the nucleon, producing a messy hadronic system in the final state. As the neutrino has enough energy to interact at the quark level in the nucleons, it is termed as "deep". Beyond the resonance interaction range, the DIS interaction range is at the invariant mass $W \geq 2GeV$ and at high momentum transfer of $Q^2 \geq 1GeV^2$.

The intermediate state between the resonance process and the DIS process is called shallow inelastic scattering (SIS). In the DIS interaction, as it is occurring in high neutrino energy, most of the energy is transferred to the hadronic system and a small energy goes to the lepton, so we detect a short track length of muon. Examples of charge current and neutral current DIS interaction processes are as follows:

$$\begin{aligned} &\nu_\mu N \to \mu^- X, \bar{\nu}_\mu N \to \mu^+ X \\ &\nu_\mu N \to \nu_\mu X, \bar{\nu}_\mu N \to \bar{\nu}_\mu X, \end{aligned} \tag{1.42}$$

where N is the nucleon bound inside a nucleus and X is the hadrons in the final state.

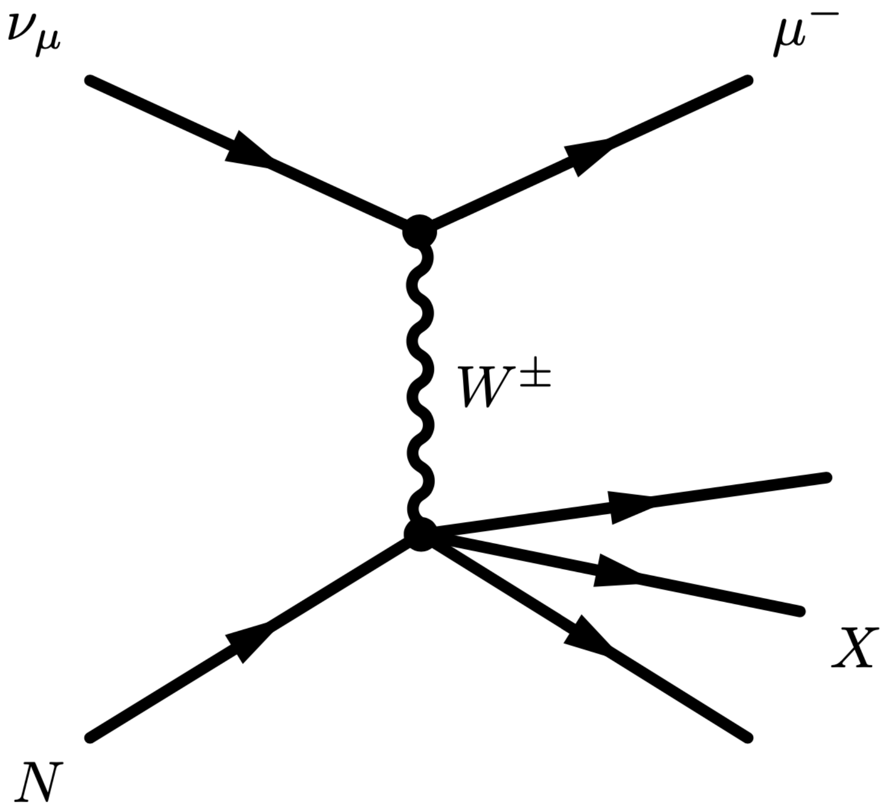

Figure 1.6 Charged current DIS neutrino-nucleus interaction process.

The double-differential cross-section for this interaction is determined as follows:

$$\frac{d^2\sigma}{dxdy} = \frac{G_F^2 M E_\nu}{\pi}\left[\left(1 - y + \frac{y^2}{2} + C_1\right) F_2(x) \pm y\left(1 - \frac{y}{2} + C_2\right) xF_3(x)\right], \tag{1.43}$$

where x, y are the Bjorken scaling variable as defined in the 2.4 and C_1, C_2 depend on these variables and defined as:

$$\begin{aligned} C_1 &= \frac{M_l^2(y-2)}{4ME_\nu x} - \frac{Mxy}{2E_\nu} - \frac{M_l^2}{4E_\nu^2}, \\ C_2 &= -\frac{M_l^2}{4MxE_\nu}, \end{aligned} \tag{1.44}$$

where M_l and M are the mass of the final-state lepton and nucleons, respectively. The $F_2(x), xF_3(x)$ are the nucleon structure functions calculated using the parton distribution function [18].

MESON EXCHANGE CURRENT (MEC)

There is another process beyond the above processes that currently draws more attention in the neutrino scattering community. In this process, when a neutrino communicates with nucleons through W, it is absorbed by nucleons and knocking out two-nucleon and two-hole pairs (2p-2h) through an exchange of a meson (Figure 1.7).

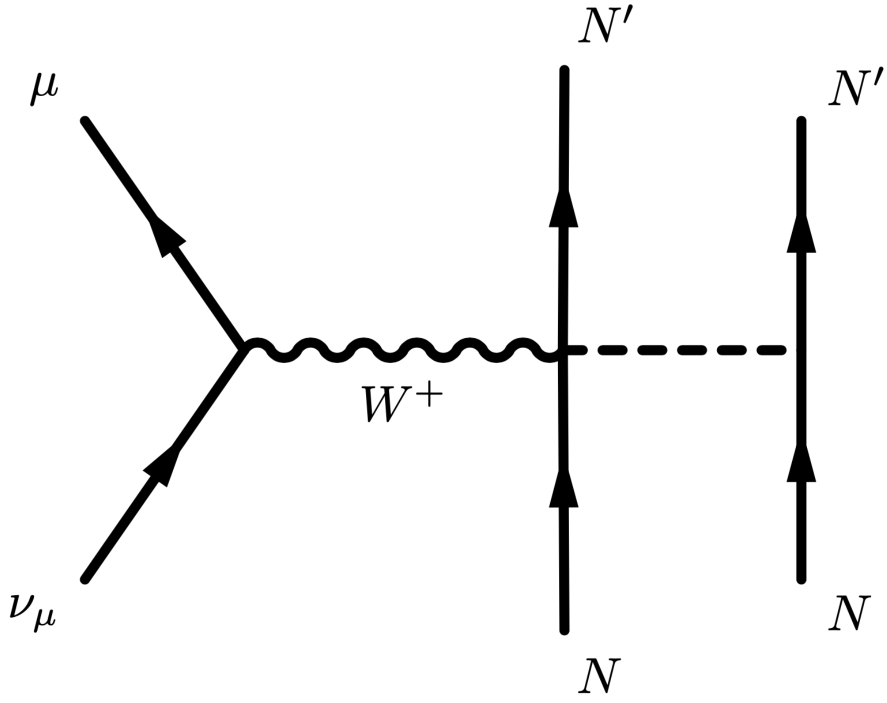

Figure 1.7 Charged current meson exchange current neutrino-nucleus interaction process.

There is also a possibility of producing 3p-3h in the final state, so overall this is called np-nh or multi-nucleon excitation. Today, excitation of multi-nucleon and charged lepton in the final state except the pion absorption is termed quasi-elastic-like events. The excitation of 2p-2h was first proposed by Delorme and Ericson in the neutrino scattering process [19]. This process has a significant contribution to neutrino-nucleus scattering, and the community agrees that meson exchange currents are needed to explain the neutrino QE data. However, there are several phenomenological approaches by Lalakulich, Mosel et. al. [20], [21], [22], [23] and Bodek et. al. [24] and the most competitive theoretical approach by Martini et. al [25], [26], [27], [28], [29], Nieves et. al. [30], [31], [32], [33], [34] and Amaro et. al. [35], [36], [37], [38], [39], [40], [41], [42] to address the contributions of np-nh to the neutrino-nucleus cross section.

1.3.8 NUCLEAR EFFECTS

Almost all modern neutrino detectors are made of heavy nuclei. Much of the uncertainty on cross-section models is due to poorly understood nuclear effects. This systematic uncertainty is one of the biggest uncertainties for the oscillation experiments such as NOvA, T2K, and future long-baseline experiments DUNE and Hyper-Kamiokande. In these accelerator-based experiments, the neutrino beam energy ranges from hundreds of MeV to a few GeV. Using such neutrino energies, a neutrino can probe the structure of the nucleus at the nucleon level. The effects of the nuclear environment on neutrino interactions are substantial, and some of them are discussed below.

RELATIVISTIC FERMI GAS (RFG) MODEL

According to the Pauli exclusion principle, no two identical fermions can occupy the same state. In nuclei, there will be many protons and neutrons that are distributed by Fermi-Dirac statistics. Nucleons occupy states in Fermi gas (all the nucleons are noninteracting and all states are filled up in the same order) up to Fermi level. In the Fermi gas model, nucleons move independently within the nuclear volume in a constant binding potential generated by all nucleons. This is known as the Fermi motion. The Fermi momentum is denoted by k_F. Another term called Pauli blocking is related to the Relativistic Fermi Gas model, in which nucleons cannot achieve the momentum state that is already occupied, so it should have a momentum above Fermi momentum. When an interaction with a neutrino transfers enough energy to put a nucleon above the Fermi level and binding energy, the nucleon is ejected and the rest of the nucleons remain as spectators, otherwise it is Pauli blocked, the reaction is suppressed, and the kinematic distributions are modified due to Pauli blocking.

In general, the above approach of the relativistic Fermi gas model is known as the Global Fermi Gas (GFG) model. In the case of GFG, the nucleus is assumed as a box of constant nuclear density and the momentum distribution is the size of the nucleus, defined as:

$$p_F^{GFG} = \frac{\hbar}{r_0}\left(\frac{9\pi N}{4A}\right)^{1/3}, \tag{1.45}$$

where $N(A-Z)$ is the number of neutrons and, for proton, the momentum distribution is replaced by Z instead of N. A is the atomic mass and $R = r0A^{1/3}$ in the radius of the Fermi sphere (the energy state occupied by nucleons with momentum space in the sphere) and the value of $r_0 = 1.25 \pm 0.20 fm$. The minimal extension of the RFG model is called the local Fermi Gas (LFG) model, where Fermi momentum and binding energy (the amount of energy needed to exit the nucleon from the nucleus) depend on the radial position in the nucleus, following the density profile of the nuclear matter.

$$p_F^{LFG} = \hbar\left(3\pi^2\rho(r)\frac{N}{A}\right)^{1/3}, \tag{1.46}$$

where rho is the nuclear density depending on the radius (distance from the center of the nucleus). This distribution arises from the electron scattering data [43]. The comparative distribution of LFG and GFG is shown. The use of a local Fermi gas model will affect the final-state nucleon energy distribution [44] as well as the cross-section.

SHORT RANGE CORRELATION (SRC)

The Relativistic Fermi Gas model is used to describe the nuclear effects in the QE region, which is based on the simplest independent particle model called the Fermi

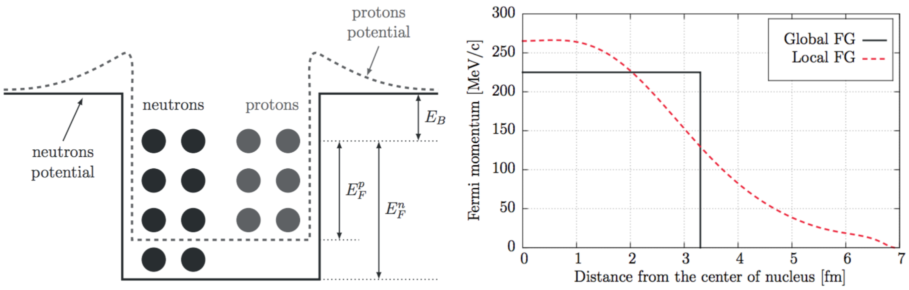

Figure 1.8 Cartoon of a potential wall (left) and a comparison of Local Fermi Gas and Global Fermi Gas model (right). Both figures are reprinted from [45].

gas model. Here all the nucleons in the nucleus are degenerate, or in other words, nucleons are uncorrelated. If we think that nucleons in the nucleus are correlated, and the distance between two nucleons is very short $(< 15fm)$ there is an involvement of a mechanism called short-range correlation [46] in which strong short-range forces get to increase their relative momentum (more than Fermi momenta) and impel the two nucleons far off-shell. A nucleon involved in this process is about 20% of the time, and most of the time, participation in correlation is proton-neutron [47], [47].

The short-range correlation generates two high-energy isosinglet nucleons with opposite isospins and an isotriplet component which can contribute to proton-proton, proton-neutron, and neutron-neutron pairs. More details can be found in ref. [48].

Random Phase Approximation (RPA)

The Random Phase Approximation (RPA) method has been developed to understand the long-range correlation between nucleons in the nucleus, it also outlines the collective excitation of the nucleus. Collective excitations of different momenta are orthogonal and phases can be treated randomly, so it is termed as “Random Phase”. The RPA is a non-perturbative method to describe the complexity of many-body interactions. So far RPA has been studied in the QE regime where there is a knockout of a single nucleon and one of the great successes is the prediction of collective surface vibrations, called giant resonances in the energy range that are between 0.015 and 0.030 GeV [49].

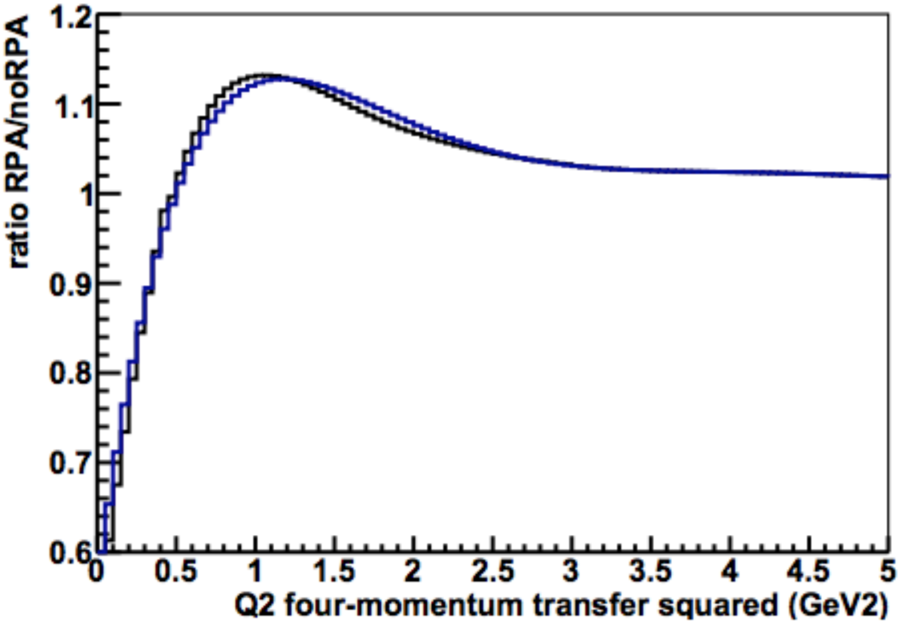

Figure 1.9 Ratio of RPA/noRPA for GENIE neutrino events with the full central weighting as a function of four-momentum transfer squared. This figure is taken from Ref. [50]

RPA also considers modification of electroweak coupling strengths, due to the presence of strongly interacting nucleons in the nucleus in comparison to its free nucleon coupling strength [51]. RPA corrections strongly decrease as the neutrino energy increases. RPA is strongly suppressed at low four-momentum transfer (it shows that nucleons are embedded in nuclear potential); also there is mild enhancement at higher four-momentum transfer (almost no RPA effect increases as Q^2 increases, which means that if high energy is transferred to the nucleus, then nucleons, quarks might be free) is shown in Figure 1.10). A variant of RPA, called continuum RPA, takes into account that the final nucleon is in the continuum.

FINAL STATE INTERACTIONS (FSI)

Initially, when a neutrino interacts with one of the nucleons, it generates hadrons (pions, protons, etc.) by ejecting a final-state charged lepton exiting from the nucleus. The hadronic shower again scatters and rescatters with the rest of the nucleons inside the dense nuclear matter before exiting the nucleus. This changes the kinematics, multiplicity, and charge of the hadrons in the final state described. FSI effects on the topology of events reconstruction. For example, if we see a muon and a proton in the final state and no pions in the detector, we cannot tell if this was a real CCQE event or a RES event where the pion has been reabsorbed in the nucleus. It resulted in CC-RES events showing up as CCQE-like ($CC0\pi$) events.

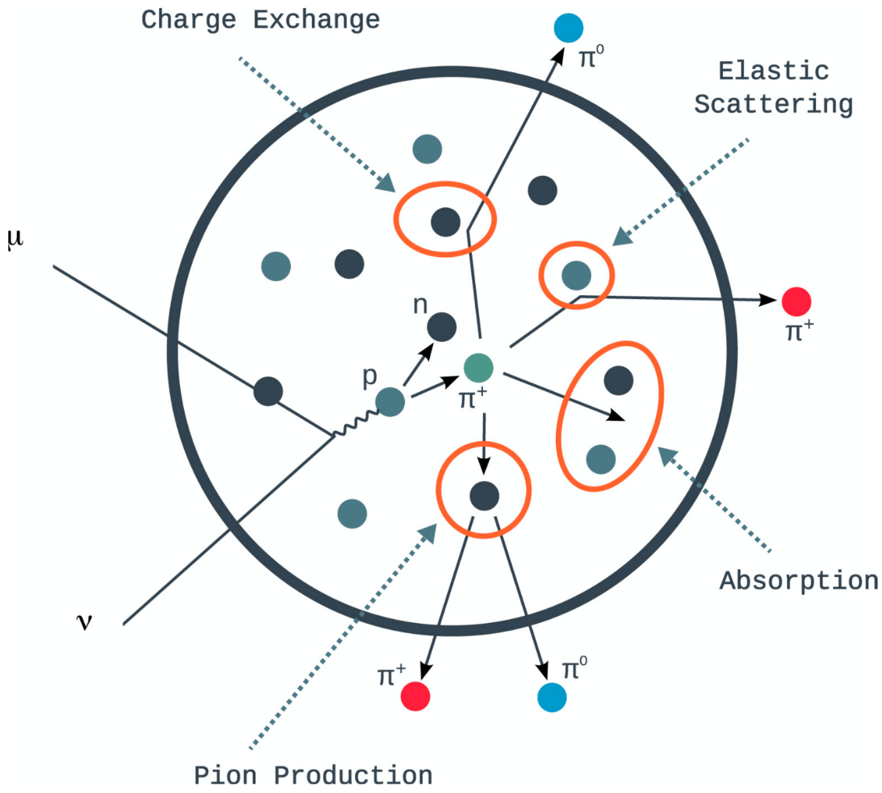

Figure 1.10 Diagram of a final state interaction reprinted from Ref. [52]

One more important thing is that the neutrino energy is unknown when it is entering the nucleus. The neutrino energy is reconstructed from the final-state particles that we observe in our detector. It is also happening that some energy gets lost in the rescattering in the nucleus and cannot be reconstructed. Therefore, FSI has impact on neutrino calorimetric energy reconstruction. FSI can be estimated by computing a mean free path for scattering (λ) of the struck nucleon,

$$\lambda(r) = [\sigma\rho(r)]^{-1}$$

where $\rho(r)$ is the nuclear density, σ is the scattering cross section between nucleon and nucleon.

1.4 Motivation

The main objective of this analysis is to measure the total cross-section of the charge current coherent pion production. The process of charged-current (CC) coherent neutrino-nucleus pion production is characterized by minimal momentum transfer to the nucleus, leaving it in its ground state. Despite the inherent uncertainties in the production cross section, coherent meson production by neutrinos is significant, as it offers insights into the structure of the weak current and can serve as a potential background source for modern neutrino oscillation experiments and searches for physics beyond the Standard Model (BSM). This Ph.D. thesis presents a novel measurement of CC coherent pion production in the NOvA near detector at the Fermilab facility. The analysis utilizes Convolutional Neural Networks (CNN) for both particle identification and kinematic selection criteria, achieving a selection purity of 60%. The energy range of 1-5 GeV covered by the available NOvA exposure in the NuMI beam makes the results valuable for future neutrino experiments like the Deep Underground Neutrino Experiment (DUNE).

1.5 Thesis Overview

This chapter delves into the particle composition of the SM, while also highlighting its triumphs and shortcomings, highlighting the existence of potential novel physics, and providing an overview of physics and neutrino-nucleus interactions. The subsequent chapter, Chapter 2, primarily elaborates on the theories governing Coherent Meson production by neutrinos. In Chapter 3, we provide a concise overview of the NOvA experiment. Chapter 4 outlines the simulation chain employed in the NOvA experiment, followed by the reconstruction and calibration processes in Chapter 5. A detailed explanation of the analysis and its outcomes is presented in Chapter 6 and later chapters.

CHAPTER 2

COHERENT PION PRODUCTION BY NEUTRINOS

Before moving on to theoretical models of coherent pion interaction, it is essential to define the notation.

2.1 WEAK INTERACTION SCATTERING

Before we talk about any theoretical models of coherent meson interaction, let us define some notations used in this chapter.

- p_ν and p_μ: The incoming neutrino and the outgoing lepton's four-momentum.
- E_ν and E_μ: The incoming neutrino and outgoing lepton's energy.
- p and p': The four-momentum of the initial and final state of the hadronic system.
- q: The four-momentum transfer (out of the leptonic system).
- ν: Energy transfer out of the leptonic system.
- Q^2: The negative square of the four-momentum transfer.
- M: The target mass.

In the previous chapter, we have already defined Bjorken x and y as follows:

$$\begin{aligned} y &= \frac{\nu}{E_\nu} \\ x &= \frac{Q^2}{2p \cdot q} = \frac{Q^2}{2M\nu} \end{aligned} \tag{2.1}$$

2.2 Weak Interaction Scattering Amplitude

In most neutrino oscillation experiments, the mass of the W boson is much larger than the mass of momentum transfer, the scattering amplitude of a neutrino charged current interaction can be expressed as:

$$\mathcal{M} = \frac{G_F}{\sqrt{2}} j_w^\alpha w_\alpha \tag{2.2}$$

Where G_F is the Fermi coupling constant, j_w^α is the weak leptonic current coupled with charged W boson, $\omega\alpha$ is the corresponding hadronic current. The CC leptonic current can be expressed as follows:

$$j_w^\alpha = \bar{\psi}_l \gamma^\alpha \left(1 - \gamma^5\right) \psi_\nu \tag{2.3}$$

The form of the hadronic current is not the same as the leptonic one, since the nucleon/nucleus is not a point particle but a composite system made of quarks and gluons/multiple nucleons. Generally, it is expressed as:

$$w_\alpha = \bar{\psi}_p \gamma^\alpha \left(V_\alpha - A_\alpha\right) \psi_n \tag{2.4}$$

The V_α A_α here are the vector and axial-vector components of the current, respectively. Combining the leptonic and hadronic currents we have:

$$\mathcal{M} = \frac{G_F}{\sqrt{2}} \bar{\psi}_l \gamma^\alpha \left(1 - \gamma^5\right) \psi_\nu \left[V_\alpha - A_\alpha\right] \tag{2.5}$$

.The square of the scattering amplitude gives:

$$\begin{aligned}
|\mathcal{M}|^2 &= \frac{G_F^2}{2} \bar{\psi}_l \gamma^\alpha \left(1 - \gamma^5\right) \psi_\nu \left[V_\alpha - A_\alpha\right] \left\{\bar{\psi}_l \gamma^\beta \left(1 - \gamma^5\right) \psi_\nu \left[V_\beta - A_\beta\right]\right\}^* \\
&= \frac{G_F^2}{2} \bar{\psi}_l \gamma^\alpha \left(1 - \gamma^5\right) \psi_\nu \left[V_\alpha - A_\alpha\right] \left[V_\beta^* - A_\beta^*\right] \bar{\psi}_\nu \gamma^\beta \left(1 - \gamma^5\right) \psi_l \\
&= \frac{G_F^2}{2} \bar{\psi}_\nu \gamma^\beta \left(1 - \gamma^5\right) \psi_l \bar{\psi}_l \gamma^\alpha \left(1 - \gamma^5\right) \psi_\nu \left[V_\alpha - A_\alpha\right] \left[V_\beta^* - A_\beta^*\right] \\
&= \frac{G_F^2}{2} \operatorname{Tr}\left(\psi_\nu \bar{\psi}_\nu \gamma^\beta \left(1 - \gamma^5\right) \psi_l \bar{\psi}_l \gamma^\alpha \left(1 - \gamma^5\right)\right) \left[V_\alpha - A_\alpha\right] \left[V_\beta^* - A_\beta^*\right] \\
&= \frac{G_F^2}{2} \operatorname{Tr}\left(p_\nu \gamma^\beta \left(1 - \gamma^5\right) \left(p_\mu + m_\mu\right) \gamma^\alpha \left(1 - \gamma^5\right)\right) \left[V_\alpha - A_\alpha\right] \left[V_\beta^* - A_\beta^*\right] \\
&\equiv \frac{G_F^2}{2} L^{\alpha\beta} W_{\alpha\beta}
\end{aligned} \tag{2.6}$$

In the middle, the Casimir trick is used. And spins are implicitly summed for incoming neutrino and outgoing lepton by the equation:

$$\sum_{spins} u\bar{u} = \gamma^{\mu} p_{\mu} + m \tag{2.7}$$

Normally, the initial particle spins are averaged, and the final particle spins are summed. But neutrinos are always left-handed(antineutrinos are always right-handed). Also defined:

$$\begin{aligned} L^{\alpha\beta} &= \mathrm{Tr}\left(\not{p}_{\nu}\gamma^{\beta}\left(1-\gamma^{5}\right)\left(\not{p}_{\mu}+m_{\mu}\right)\gamma^{\alpha}\left(1-\gamma^{5}\right)\right) \\ W_{\alpha\beta} &= \left[V_{\alpha}-A_{\alpha}\right]\left[V_{\beta}^{*}-A_{\beta}^{*}\right] \end{aligned} \tag{2.8}$$

Note: the subscripts ν and μ represent the neutrino and the muon, not the four-vector indices. The leptonic tensor can be calculated as:

$$L^{\alpha\beta} = 2\left[\mathrm{Tr}\left(\not{p}_{\nu}\gamma^{\beta}p_{\mu}\gamma^{\alpha} + m_{\mu}\,\mathrm{Tr}\left(p_{\nu}\gamma^{\beta}\gamma^{\alpha}\right) - \mathrm{Tr}\left(p_{\nu}\gamma^{\beta}\gamma^{5}p_{\mu}\gamma^{\alpha}\right) - m_{\mu}\,\mathrm{Tr}\left(\not{p}_{\nu}\gamma^{\beta}\gamma^{\alpha}\gamma^{5}\right)\right)\right] \tag{2.9}$$

The trace of any odd number of gamma matrices will be zero. Therefore, the second trace does not contribute. γ^5 contains an even number of gamma matrices. Therefore, if it is paired with an odd number of gamma matrices, the trace is zero, so the last term does not contribute. After using some "trace theorems" which can be found in most quantum field theory books, we are left with:

$$L^{\alpha\beta} = 8\left[p_{\nu}^{\beta}p_{\mu}^{\alpha} + p_{\nu}^{\alpha}p_{\mu}^{\beta} - \left(p_{\nu}\cdot p_{\mu}\right)g^{\alpha\beta} - i\epsilon^{\alpha\beta\lambda\sigma}\left(p_{\nu}\right)_{\lambda}\left(p_{\mu}\right)_{\sigma}\right] \tag{2.10}$$

If we assume negligible lepton mass we'll have:

$$p_{\nu}\cdot p_{\mu} = \frac{Q^2}{2}\left(m_{\mu}\to 0\right) \tag{2.11}$$

Taking the low limit Q^2, then, the term $\rho_\nu\ \rho_\mu$ vanishes. Since $Q^2 = 2E_\nu E_\mu(1-\cos\theta)$, in the limit $Q^2 \to 0$, $\theta \to 0$, the muon is parallel to the neutrino. So in this limit, $\overrightarrow{p_\nu}\overrightarrow{p_\mu}$ and $\vec{q}$ all three vectors are parallel. Because we are neglecting muon mass for high energies, we can describe the lepton 4-vectors in terms of the 4 -momentum transfer:

$$\begin{aligned} p_\nu &= \left(\frac{E_\nu}{\nu}\right) q \\ p_\mu &= \left(\frac{E_\nu}{\mu}\right) q \end{aligned} \tag{2.12}$$

Therefore, the leptonic tensor can be expressed in terms of q:

$$L^{\alpha\beta} = 8\frac{E_\nu E_\mu}{\nu^2}\left[q^\alpha q^\beta + q^\beta q^\alpha - i\epsilon^{\alpha\beta\lambda\sigma} q_\lambda q_\sigma\right] \tag{2.13}$$

The last term contains an antisymmetric tensor multiplied by a term that is symmetric under the same exchange; so the term will vanish after summation. Therefore, we have our final form of the leptonic tensor as follows:

$$L^{\alpha\beta} = 16\frac{E_\nu E_\mu}{\nu^2} q^\alpha q^\beta \tag{2.14}$$

2.2.1 Hadronic tensor $W_{\alpha\beta}$

One of the fundamental postulates of quantum mechanics is the representation of momentum and energy as derivatives of space and time.

$$\begin{aligned} \vec{p} &\longrightarrow -i\vec{\nabla} \\ E &\longrightarrow i\partial_t \end{aligned} \tag{2.15}$$

Applying this to the classical equation of conservation of energy ($E = p^2/2m + V$), we immediately get the Schrödinger equation, and we can obtain the Klein-Gordon equation by applying it to the relativistic version. A simpler 4-vector way to describe the above relation is:

$$p^\mu = (E, \vec{p}) \longrightarrow i\partial^\mu = i\left(\partial_t, -\vec{\Delta}\right) \tag{2.16}$$

Considering the amplitude for a one-particle pion state with momentum q,

$$\langle 0 \left| J^\alpha(x) \right| \pi\rangle = \left\langle 0 \left| e^{i\hat{P}x} J^\alpha(0) e^{-i\hat{P}x} \right| \pi\right\rangle = \langle 0 \left| J^\alpha(0) \right| \pi\rangle \, e^{-iqx} \tag{2.17}$$

The derivative of this is:

$$\begin{aligned}\partial_\alpha \langle 0 | J^\alpha | \pi \rangle &= \left\langle 0 \left| \partial_\alpha \left(J^\alpha(0) e^{-iqx} \right) \right| \pi \right\rangle = \left\langle 0 \left| -iq_\beta J^\alpha(0) e^{-iqx} \partial_\alpha x^\beta \right| \pi \right\rangle \\ &= \left\langle 0 \left| -iq_\beta J^\alpha \partial_\alpha x^\beta \right| \pi \right\rangle = \left\langle 0 \left| -iq_\beta J^\alpha \delta^\beta_\alpha \right| \pi \right\rangle \\ &= -iq_\alpha \langle 0 | J^\alpha | \pi \rangle \end{aligned} \tag{2.18}$$

from this we can conclude:

$$\partial_\alpha J^\alpha = -iq_\alpha J^\alpha \tag{2.19}$$

which is in accordance with the fundamental postulate in Equation 2.16. Furthermore, the square of the amplitude's derivative is :

$$|\partial_\alpha J^\alpha|^2 = (-iq_\alpha J^\alpha) \left(iq_\beta J^{\beta *} \right) = q_\alpha q_\beta J^\alpha J^{\beta *} = q_\alpha q_\beta W^{\alpha\beta} \tag{2.20}$$

Once we put the final form of the leptonic tensor into the amplitude squared, we'll arrive at:

$$|\mathcal{M}|^2 = \frac{G_F^2}{2} 16 \frac{E_\nu E_\mu}{\nu^2} q^\alpha q^\beta W_{\alpha\beta} = 8 G_F^2 \frac{E_\nu E_\mu}{\nu^2} \left| \partial^\alpha \left(V_\alpha - A_\alpha \right) \right|^2 \tag{2.21}$$

By CVC we have $\partial^\alpha V_\alpha = 0$ at low Q^2, which leaves only the dependence on the axial-vector current in the squared amplitude.

$$|\mathcal{M}|^2 = 8 G_F^2 \frac{E_\nu E_\mu}{\nu^2} \left| \partial^\alpha A_\alpha \right|^2 \left(Q^2 \to 0 \; and \; m_l = 0 \right) \tag{2.22}$$

The PCAC hypothesis relates the divergence of the axial vector current to the amplitude of the pion field, ϕ_π.

$$\partial_\lambda A^\lambda = f_\pi m_\pi^2 \phi_\pi \tag{2.23}$$

According to Adler using PCAC[40] and the Goldberger-Treiman relation we can equate the divergence of the axial-vector current with the corresponding scattering of a pion.

$$\left| \left\langle \beta \left| \partial_\lambda \, A^\lambda \right| \alpha \right\rangle \right|^2 = f_\pi^2 |\mathcal{M}(\pi\alpha \to \beta)|^2 \tag{2.24}$$

putting this into our form of $|\mathcal{M}|^2$, we have:

$$|\mathcal{M}|^2 = 8G_F^2 \frac{E_\nu E_\mu}{\nu^2} f_\pi^2 |\mathcal{M}(\pi\alpha \to \beta)|^2 \tag{2.25}$$

At this point, we have related the weak neutrino interaction to pion nucleus scattering and we are in a good position to calculate the cross-section. According to Fermi's Golden rule on the cross-section for one incoming particle hit on a static target:

$$\begin{aligned} d\sigma &= \frac{|\mathcal{M}|^2}{2E_\nu 2M} \left(\frac{d^3 p_\mu}{(2\pi)^3} \frac{1}{2E_\mu} \right) \left(\frac{d^3 p'}{(2\pi)^3} \frac{1}{2p'_0} \right) (2\pi)^4 \delta^4 \left(p_\nu + p - p_\mu - p' \right) \\ &= \frac{G_F^2}{M\nu^2} f_\pi^2 |\mathcal{M}(\pi\alpha \to \beta)|^2 \left(\frac{d^3 p_\mu}{(2\pi)^3} \right) \left(\frac{d^3 p'}{(2\pi)^3} \frac{1}{2p'_0} \right) (2\pi)^4 \delta^4 \left(p_\nu + p - p_\mu - p' \right) \end{aligned} \tag{2.26}$$

2.2.2 DERIVING $d\sigma$ IN TERMS OF dQ^2 AND $d\nu$

It is possible to express $d\sigma$ in terms of dQ^2 and $d\nu$ rather than $d^3 p_\mu$. By ignoring the lepton mass, we have $Q^2 \approx 2EE'(1 - \cos\theta)$. By taking its derivative:

$$dQ^2 = \left(\frac{\partial Q^2}{\partial \theta} \right) d\theta + \left(\frac{\partial Q^2}{\partial E'} \right) dE' \tag{2.27}$$

The initial energy is assumed to be fixed. Therefore, it's not included here. Now for $d\nu$ we have $d\nu = d\left(E - E'\right) = dE - dE' \to d\nu = -dE'$, The minus sign is a simple matter of changing the integration limits.

$$\int_0^E dE' = -\int_E^0 d\nu = \int_0^E d\nu \tag{2.28}$$

It is easier to understand in the way that when the outgoing lepton has zero energy, then the full energy E has been transferred to the hadronic system. Therefore, it's totally safe to take $d\nu = dE'$ and we multiply both sides with them respectively, we get:

$$dQ^2 d\nu = \left(\frac{\partial Q^2}{\partial \theta} \right) d\theta dE' + \left(\frac{\partial Q^2}{\partial E'} \right) \left(dE'\right)^2 \tag{2.29}$$

The second term is too small to be integrated and we finally have:

$$dQ^2 d\nu = \left(\frac{\partial Q^2}{\partial \theta}\right) d\theta dE' = \left(2EE' \sin\theta\right) d\theta dE' \tag{2.30}$$

For d^3p we have:

$$\begin{aligned} d^3p &= |\vec{k}|^2 d|\vec{k}| d\Omega \approx E'^2 dE' d\Omega = 2\pi E'^2 dE' \sin\theta d\theta \\ &= \pi \frac{E'}{E} dQ^2 d\nu \end{aligned} \tag{2.31}$$

Use this equation to replace d^3p_μ then, We have:

$$d\sigma = \frac{G_F^2 E_\mu dQ^2 d\nu}{2\pi^2 \nu E_\nu} f_\pi^2 \left[\frac{|\mathcal{M}(\pi\alpha \to \beta)|^2}{2M 2\nu} \left(\frac{d^3p'}{(2\pi)^3} \frac{1}{2p_0'}\right) (2\pi)^4 \delta^4\left(p_\nu + p - p_\mu - p'\right)\right] \tag{2.32}$$

Now we want to replace the amplitude of the pion scattering process with the cross-section of it. We will have the same target α with 4-momentum p = (M, 0, 0, 0), the same final hadron state β with 4-momentum p', and an initial pion with 4-momentum $(p_\nu - p_\mu)$. We are going to make an assumption that the relative velocity can be approximated as unity when either the initial pion is off-shell by an amount on the order of its mass or we are assuming a very high energy pion where its mass is negligible. To reiterate, we must take the 4-vector of the initial pion to be the difference of the lepton 4-vector.

$$p_\pi = p_\nu - p_\mu \tag{2.33}$$

Also,

$$E_\pi = yE_\nu \tag{2.34}$$

With this result, we can find out the cross-section for the pion scattering process:

$$d\sigma(\pi\alpha \to \beta) = \left[\frac{|\mathcal{M}(\pi\alpha \to \beta)|^2}{2M 2\nu} \left(\frac{d^3p'}{(2\pi)^3} \frac{1}{2p_0'}\right) \times (2\pi)^4 \delta^4\left(p_\nu + p - p_\mu - p'\right)\right] \tag{2.35}$$

By comparing this cross-section with the neutrino cross-section we arrived a while ago, everything in the brackets are exactly the same, so we finally have:

$$\left.\frac{d^2\sigma(\nu\alpha \to \mu\beta)}{dQ^2 d\nu}\right|_{Q^2 \to 0} = \left(\frac{G_F^2 f_\pi^2 (1-y)}{2\pi^2 \nu}\right) d\sigma(\pi\alpha \to \beta)\bigg|_{E_z = yE_\nu} \tag{2.36}$$

This expression is known as Adler's theorem [53], it relates the weak neutrino-nucleus cross-section to that of the strong pion-nucleus cross-section.

2.2.3 cross-section of Antineutrino

It should be easy to figure out that the antineutrino cross-section is identical to its neutrino counterpart:

$$\sigma(\bar{\nu}\alpha \to \mu\beta) = \sigma(\nu\alpha \to \mu\beta) \tag{2.37}$$

2.2.4 The Neutral Current Cross-Section

For the neutral current, it is required to replace the pion's decay constant due to isospin.

$$f_{\pi^0} = \frac{f_{\pi^\pm}}{\sqrt{2}} \tag{2.38}$$

Therefore, the cross-section simply becomes:

$$\left.\frac{d^2\sigma(\nu\alpha \to \mu\beta)}{dQ^2 d\nu}\right|_{Q^2 \to 0} = \left(\frac{G_F^2 f_\pi^2 (1-y)}{4\pi^2 \nu}\right) d\sigma(\pi\alpha \to \beta)\Big|_{E_z = yE_\nu} \tag{2.39}$$

The NC cross-section is simply half of the CC cross-section. This quantity is often given in terms of Bjorken variables x and y. From the definition of x and y, we have:

$$\begin{aligned} Q^2 &= 2M\nu x \\ \nu &= E_\nu y \end{aligned} \tag{2.40}$$

By taking the derivatives of them we'll have $(dE_\nu = 0)$:

$$\begin{aligned} dQ^2 &= 2M\nu dx + 2Mx d\nu \\ \nu &= E_\nu dy \end{aligned} \tag{2.41}$$

so, we'll have:

$$\begin{aligned} dQ^2 d\nu &= (2M\nu dx + 2Mx d\nu)\,(E_\nu dy) \\ &= (2ME_\nu y dx + 2MxE_\nu dy)\,(E_\nu dy) \\ &\overset{(dy)^2=0}{=} 2ME_\nu^2 y dx dy \end{aligned} \tag{2.42}$$

By taking this into the cross-section equation and after some organization, we finally have our cross-section:

$$\left.\frac{d^3\sigma\left(\nu\alpha \to \nu\pi^0\alpha\right)}{dxdydt}\right|_{Q^2=0} = \left(\frac{G_F^2 f_\pi^2 M E_\nu (1-y)}{2\pi^2}\right)\left[\frac{d\sigma(\pi\alpha \to \pi\alpha)}{dt}\right]_{E_\pi = yE_\nu} \tag{2.43}$$

2.2.5 Rein and Sehgal Model

The cross-section for coherent pion production is derived from Adler's PCAC theorem. So far, we assumed that $Q^2 = 0$. Rein and Sehgal model [54] extended it to non-zero Q^2, and used pion-nucleon scattering to model the pion-nucleus cross section. Rein and Sehgal introduced a form factor to transit the cross section from zero Q^2 to non-zero Q^2 :

$$\frac{d^3\sigma\left(\nu\mathcal{A} \to \nu\pi^0\mathcal{A}\right)}{dxdydt} = \left(\frac{G_F^2 f_\pi^2 M E_\nu (1-y)}{2\pi^2}\right)\left(\frac{M_A^2}{M_A^2 + Q^2}\right)^2\left[\frac{d\sigma(\pi\mathcal{A} \to \pi\mathcal{A})}{dt}\right] \tag{2.44}$$

In order to model the pion-nucleus cross section, the authors used forward pion-nucleon scattering:

$$\frac{d\sigma(\pi\mathcal{A} \to \pi\mathcal{A})}{d|t|} = A^2\left|F_\mathcal{A}(t)\right|^2 \left.\frac{d\sigma\left(\pi^0 N \to \pi^0 N\right)}{d|t|}\right|_{t=0} \tag{2.45}$$

where $F_\mathcal{A}(t)$ is the nuclear form factor and A is the number of nucleons within the nucleus. With the optical theorem, we have the following.

$$\frac{d\sigma(\pi N \to \pi N)}{d|t|} = \frac{1}{16\pi}\left[\sigma_{\text{tot}}^{\pi^0 N}\right]^2\left(1 + r^2\right); \quad r = \frac{\operatorname{Re}\left(f_{\pi N}(0)\right)}{\operatorname{Im}\left(f_{\pi N}(0)\right)} \tag{2.46}$$

$f_{\pi N}(0)$ is the forward amplitude $\pi - N$ and $\sigma_{\text{tot}}^{\pi^0 N}$ gives the total cross section for the scattering $\pi - N$. The nuclear form factor is modeled with an exponential:

$$|F_{\mathcal{A}}(t)|^2 = e^{-b|t|} F_{abs}; \quad b = \frac{1}{3}R^2; \quad R = R_0 A^{1/3} \tag{2.47}$$

Here F_{abs} representing the effects of pion absorption in the nucleus. R is the nuclear radius and R_0 is 1.12fm. By combining all the above, we have our final R.S. formula:

$$\frac{d\sigma}{dxdyd|t|} = \frac{G_F^2 M}{2\pi^2} f_\pi^2 A^2 E_\nu (1-y) \frac{1}{16\pi} \left[\sigma_{\text{tot}}^{\pi^0 N}(E_\nu y)\right]^2 \left(1+r^2\right) \left(\frac{M_A^2}{M_A^2+Q^2}\right)^2 e^{-b|t|} F_{abs} \tag{2.48}$$

The absorption factor can be estimated by

$$F_{abs} = e^{-<x>/\lambda} \tag{2.49}$$

where $< x >$ is the average path length traversed by a π^0 produced in the nucleus, and λ is the absorption length defined in terms of the inelastic cross-section of the pion-nucleon and the nuclear density ρ by $\lambda^{-1} = \sigma_{\text{inel.}}\, \rho$ where $\rho = A\left(4/3\pi R^3\right)^{-1}$. Finally, we get:

$$F_{abs} = e^{-\frac{9A^{1/3}}{16*R_0^2}\sigma_{\text{inel}}} \tag{2.50}$$

Rein Sehgal model agrees very well with data for neutrino energy above 2GeV. This is adequate for the precision required on coherent pion cross-section measurement. However, for precise oscillation measurements, the neutrino energy centers around only a few GeV, correction of Rein Sehgal model or different methods are needed for this low-energy challenge.

2.2.6 Berger Sehgal model

The Berger-Sehgal model [55] is proposed to address the low-energy problem suffered by the Rein and Sehgal model. In the resonance region, the derivation 2.45 and

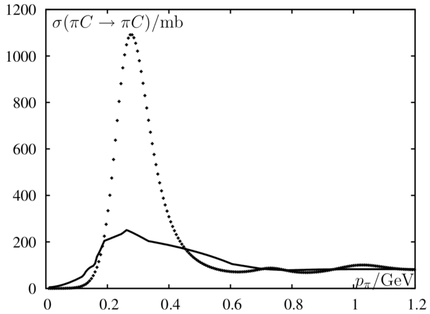

T_π GeV	A_1 mb/GeV^2	b_1 1/GeV^2
0.076	11600	116.0
0.080	14700	109.0
0.100	18300	89.8
0.148	21300	91.0
0.162	22400	89.2
0.226	16400	80.8
0.486	5730	54.6
0.584	4610	55.2
0.662	4570	58.4
0.776	4930	60.5
0.870	5140	62.2

Figure 2.1 Total elastic pion Carbon cross section versus pion laboratory momentum. Left: The dotted line represents the Rein-Sehgal model, and the solid line represents the Berger-Sehgal model by fitting with the pion carbon data. Right: The fitting result of the coefficients A_1,b_1 of the Berger-Sehgal equation. Ref. [55]

2.50 based on a simple classical ansatz may not be a valid estimation of pion-nucleus scattering. To circumvent the uncertainties in modeling nuclear processes, Berger's model directly appeals to data on pion nucleus elastic scattering. They found that the elastic πp cross section can be simply parametrized by:

$$\frac{d\sigma(\pi\mathcal{A} \to \pi\mathcal{A})}{d|t|} = A_1 e^{-b_1 t} \tag{2.51}$$

where coefficients A_1, b_1 can be fitted by external data. The result based on the fitted equation is shown in Figure 2.1, in comparison with the Rein-Sehgal model's prediction. It is clear that the cross-section from Berger Sehgal's fitting with pion Carbon data is much below the Rein Sehgal model and when P_π approaches 1GeV, the two curves become consistent which justifies the ansatz. It also suggests that the Rein Sehgal model fails in the region of the Δ resonance, but may be a valid description at higher energies.

CHAPTER 3

THE NOvA EXPERIMENT

The NOvA experiment (NuMI Off-axis ν_e Appearance) involves two detectors, namely the near detector and the far detector. It is a long baseline oscillation experiment that utilizes a high-intensity neutrino source provided by Fermilab's Neutrinos at the Main Injector (NuMI) [56]. The purpose of placing the two detectors at a significant distance is to observe neutrino oscillation phenomena.

The near detector (ND) is located 1km downstream from the neutrino source. Its main role is to measure the composition of the neutrino beam before oscillation occurs, since it is close to the source where neutrinos have not had the opportunity to oscillate. Additionally, the near detector offers an excellent opportunity for cross-section measurements. On the other hand, the far detector is located 810 km away from the neutrino source in Ash River, Minnesota. Its purpose is to measure the oscillated neutrinos.

Both detectors have similar functionality but differ in size. The NuMI beam can produce both neutrinos and antineutrinos. The oscillation probability for neutrinos and antineutrinos is different, primarily due to the matter effect. By comparing the appearance probability in neutrinos and antineutrinos, it is possible to determine whether the mass ordering is normal or inverted. Furthermore, the discrepancy in oscillation probability between neutrinos and anti-neutrinos allows measurement of the charge-parity (CP) violating phase, denoted δ. This chapter provides a detailed description of the NuMI beams and the design of the NOvA detector.

3.1 NuMI Neutrino Beam

3.1.1 Fermilab Accelerator Complex

The neutrino beam produced by Fermilab's accelerator complex (depicted in Figure 3.1) is considered to be the most potent in this particular scenario. It serves as the source for various neutrino experiments conducted at Fermilab.

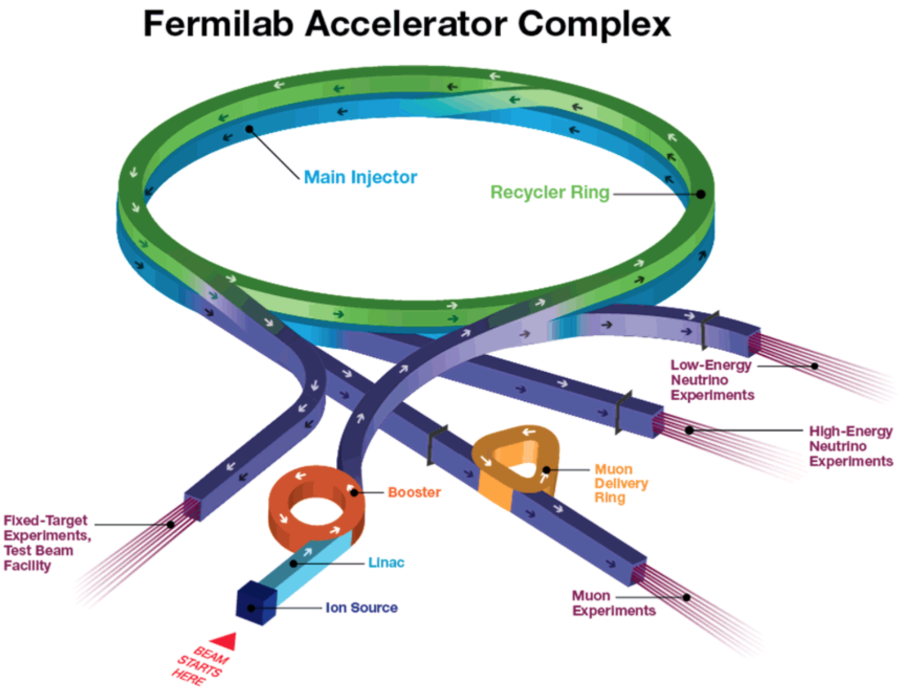

Figure 3.1 Fermilab accelerator complex

First, negative hydrogen atoms are created and accelerated to a kinetic energy of 0.4 GeV in the Linear Accelerator (LINAC). These negatively charged hydrogen atoms are then converted into positively charged hydrogen atoms (protons) by passing through a carbon foil before being sent into the booster ring, where they are accelerated to a kinetic energy of 8 GeV. The selected protons from the booster are directed into the Main Injector (MI) synchrotron accelerator, which accelerates them to 120 GeV over a circumference of 3.3 km. The proton beam is extracted from the MI and bent 58 mrad downward towards the MINOS detectors.

Initially, the NuMI beam was designed for the MINOS on-axis neutrino experiment. However, to achieve the desired beam power of 700 kW for the NOvA experiment, upgrades were made to the Fermilab accelerator complex. The detailed descriptions can be viewed in NOvA TDR [57]. The beam power was increased by reducing the cycle time from 2.2 to 1.33 seconds in the MI, achieved by adding two radio frequency (RF) cavities to accelerate the protons at a higher rate. The antiproton storage ring from the Tevatron era was transformed into the recycler storage ring. Protons from the Booster are first injected into the Recycler, which then feeds them into the MI. Improvements were made to the slip-stacking process in the recycler to increase the beam intensity of the NuMI beam.

In the slip-stacking process, the initial six proton bunches from the Booster enter the recycler and are decelerated by reducing the RF pulse. Then, six new bunches from the booster are introduced to the recycler, resulting in two bunches with different energies that slip with respect to each other. At a tuned RF frequency, the two bunches overlap, creating larger bunches before the next bunches are introduced. Finally, these bunches are extracted into the MI, and the intensity of each bunch or spill is (value) protons within a 10-microsecond beam window.

3.1.2 NuMI Beamline

The NuMI beamline originates from Fermilab in Batavia, IL and travels towards the MINOS detector hall before extending to Minnesota and eventually exiting Earth. The beam consists of protons with a kinetic energy of 120 GeV, which results in the production of high-energy mesons that further decay into energetic neutrino fluxes. The protons interact with a segmented graphite target consisting of 47 rectangular pieces (fins) stacked together. Each fin is 20.0 mm long and separated by a space of 0.3 mm, resulting in a total target length of 95.4 cm. The target has a density of $1.78 g/cm^3$.

To enhance the proton-target interactions, the target is water-cooled using two stainless steel pipes surrounding the fins. The hadrons emerging from the target are focused through two parabolic-shaped magnetic horns, which cancel out the transverse momentum of the hadrons. The magnetic horn is a coaxial conductor sheet made of aluminum and filled with a low-density gas like air, helium, or argon. A current of 200 kA is passed through the horn, creating a 1/R magnetic field, as per Ampere's law. This field focuses charged particles of a specific sign, while deflecting particles of the opposite sign. By adjusting the current, it is possible to focus on either positively charged particles, resulting in neutrinos upon decay, or negatively charged particles to produce antineutrinos.

The focused charged particles are allowed to decay within a decay pipe that is 675 m long and has a radius of 1 m. The decay of hadrons produces neutrinos and charged leptons. Following the decay pipe, the particles pass through a hadron monitor consisting of a water-cooled aluminum absorber, followed by three ionization chambers that monitor the muons. These components are spaced between rocks. Only the neutrinos continue towards the MINOS building. The schematic view of the NuMI beamline can be seen in Figure 3.2.

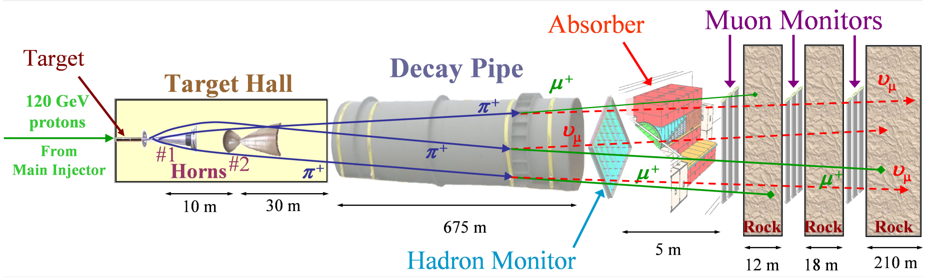

Figure 3.2 Fermilab accelerator complex

3.1.3 Off-Axis Detectors

Within the decay pipe, charged hadrons undergo decay processes that result in the production of muon neutrinos. Specifically, positive pions (π^+) decay into positive muons (μ^+) and muon neutrinos (ν_μ) according to the process $\pi^+ \rightarrow \mu^+ + \nu_\mu$, with a branching ratio of 99.98%. Similarly, positive kaons (K^+) decay into a positive muon and a muon neutrino with a branching ratio of 63.55%: $K^+ \rightarrow \mu^+ + \nu_\mu$.

In the rest frame of the decaying particles, the decay of pions and kaons is isotropic, resulting in the production of monoenergetic neutrinos. However, in the laboratory frame, considering relativistic kinematics, the neutrino flux (Φ) can be expressed as a function of the angle and the cross-sectional area (A) of the detector located at a distance (L):

$$\Phi = \left(\frac{2\gamma}{1+\gamma^2\theta^2}\right)^2 \frac{A}{4\pi L^2} \tag{3.1}$$

The energy spectra of neutrino (E_ν) as a function of pion energy and an angle is given by:

$$E_\nu = \frac{0.43E_\pi}{1+\gamma^2\theta^2} \tag{3.2}$$

In the given equation, θ represents the angle between the outgoing neutrino and the direction of the decaying meson. The parameter γ is defined as the ratio of the energy (E_π) of the meson to its rest mass (m_π). The relationship between the neutrino energy (E_ν) and the energy of the meson (E_π) is dependent on the off-axis angle, as illustrated in Figure 3.3.

Figure 3.3 depicts the relationship between E_ν and E_π for various off-axis angles. The red curve in the figure represents the off-axis angle chosen for the NOvA detectors, which is optimized to enhance the sensitivity to the oscillation of muon neutrinos into electron neutrinos.

By selecting an off-axis angle of 14.6 milliradians, the NuMI beams produce a narrow range of neutrino energy spectra, as illustrated in the left figure of Figure

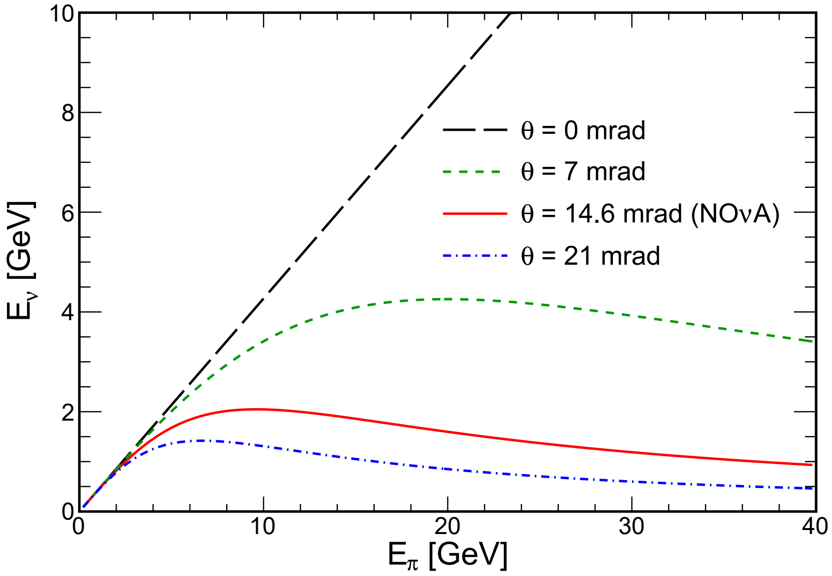

Figure 3.3 Plot of neutrino energy and pion energy for different off-axis angles.

3.4. This off-axis angle has several advantages: it suppresses neutral current events, increases the statistics of signal events (specifically ν_μ charged current events) at the desired energy range, and reduces background interference. In neutral current events, where the outgoing neutrino cannot be detected and carries away energy, it appears as a lower energy electron neutrino charged current event. By reducing high-energy neutral current events, the purity of muon neutrino charged current events is improved by minimizing background from charged pions. Additionally, high-energy neutral current events can mimic our signal electron neutrino events in the detector, so minimizing neutral current events overall increases the signal-to-background ratio.

The NuMI beamline (described in Subsection 3.1.2) can operate in neutrino or antineutrino mode by switching the polarity of the horn. In neutrino mode, the wrong-sign component in the near detector is approximately 1.8% for neutrino energies in the range of 1-3 GeV. The background of $\nu_e + \bar{\nu} e$ is around 0.7%, while the remaining approximately 97.5% consists of $\nu \mu$ events in the 1-3 GeV energy region, as shown in the right figure of Figure 3.4.

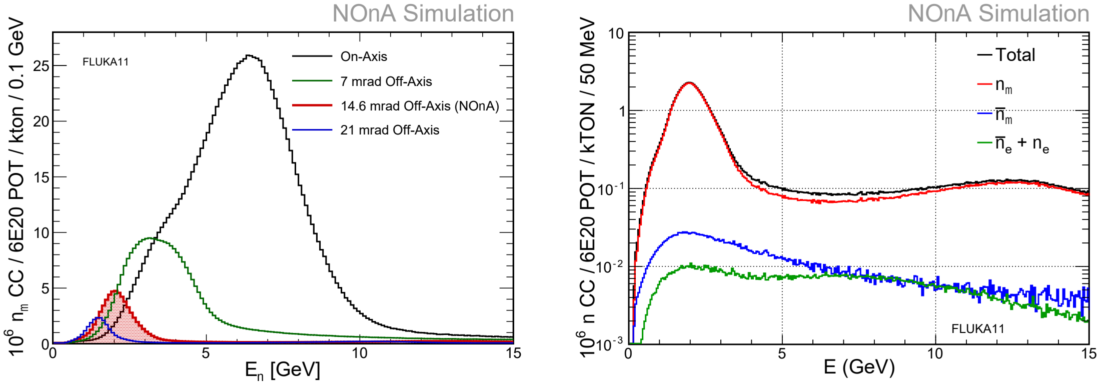

(a) (b)

Figure 3.4 The neutrino energy spectra for near detector for various off-axis angles and the y-axis represents expected number of charged current ν_μ events (a) and the flux times cross-section for different neutrino components in the NuMI beam as a function of neutrino energy (b).

3.2 THE NOvA DETECTORS

The NOvA long baseline neutrino oscillation experiment utilizes two detectors, which are identical in structure and data acquisition architecture. One detector is located at Fermilab, while the other is located 810 km away in Ash River, MN. Both detectors are positioned 14.6 mrad off-axis from the center of the neutrino beam. This similarity in physical structure and data acquisition design plays a crucial role in mitigating the effects of systematic uncertainties.

3.2.1 THE CELLS

Both detectors consist of reflective PVC tubes (cells) (Figure 3.7 (b)) filled with liquid scintillator. Each cell is equipped with a single fiber, representing a pixel of the detector. A module consists of 32 cells, as shown in Figure 3.5.

The 16 cells make a PVC extrusion (Figure 3.6) and two of the 16 cells are glued together to form a module.

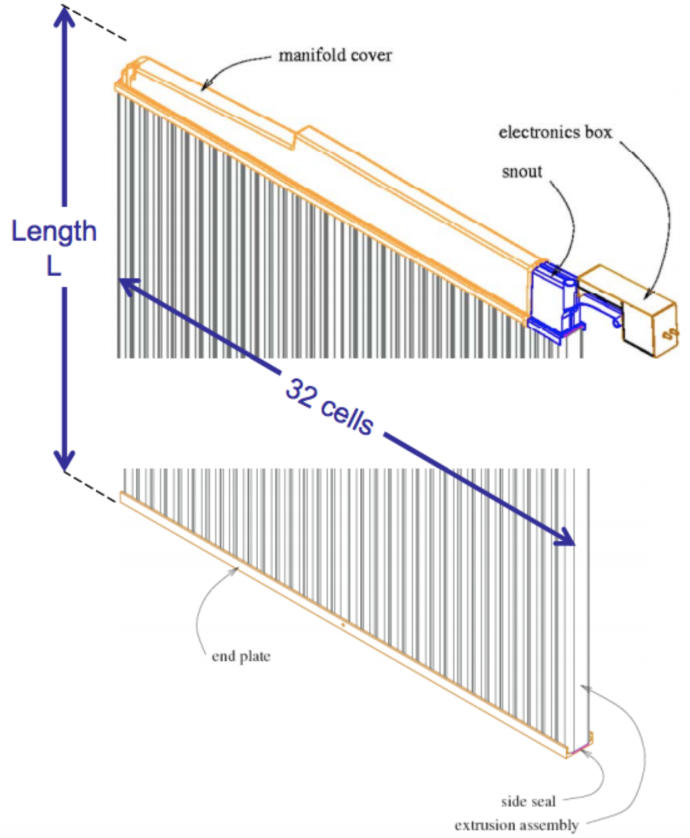

Figure 3.5 A plane created by connecting 32 plastic PVC cells.

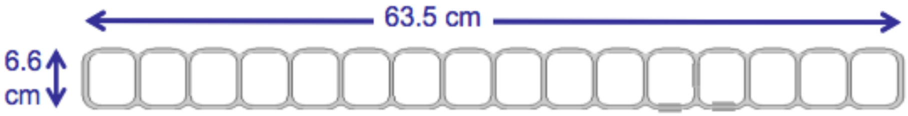

Figure 3.6 Extruded PVC Cell array.

A plane is formed by connecting a series of modules, with 12 modules in the Far Detector and 3 modules in the Near Detector. The cells have a cross section of 3.6 cm by 5.6 cm and a length of 4.2 m in the Near Detector (ND), while in the Far Detector (FD) they are 15.2 m long. To enable three-dimensional particle tracking, cells are stacked in alternating horizontal and vertical planes. Each cell is coated with titanium dioxide, serving as a reflective agent to enhance light collection in the scintillator. Inside the cell, a wavelength-shifting fiber is looped to collect light produced by the interaction of a charged particle with the liquid scintillator. Fiber ends are connected to a single pixel of an avalanche photodiode (APD), as shown in Figure 3.9.

3.2.2 The Liquid Scintillator

The liquid scintillator solution used in NOvA consists of various components that contribute to its scintillating properties. It comprises 5% pseudocumene (1, 2, 4-trimethylbenzene), which emits light in the wavelength range of 270-320 nm, and 95% mineral oil, which serves as a solvent. Two wavelength shifters are also included: PPO (2,5-diphenyloxazole), which excites photons in the range of 340-380 nm, and bis-MSB (1,4-bis-(2-methylstyryl)-benzene), which de-excites photons in the range of 390-440 nm. Additionally, the solution contains stadis-425 as an antistatic agent to reduce the risk of fire hazards caused by charge build-up and sparking during the filling process. To prevent the scintillator from yellowing and maintain its transparency over time, an antioxidant, tocopherol (vitamin E), is incorporated. Table 3.1 provides a summary of the composition of the liquid scintillator used in NOvA.

Table 3.1 Composition of liquid scintillator [57].

Component	Purpose	Mass Fraction (%)
Mineral Oil	Solvent	95.8
Pseudocumene	Scintillant	4.1
PPO	Wave Shifter	0.091
bis-MSB	Wave Shifter	0.0013
Stadis-425	Anti-Static agent	0.0003
Vitamin E	Antioxidant	0.0010
Total		100

3.2.3 The APD

APDs play a crucial role in the NOvA experiment by converting photons generated by charged particles passing through the scintillator in the PVC tubes of the detectors into electronic signals. Each APD is connected to a Front End Board (FEB), with one FEB assigned to each APD, which amplifies and reads out the electronic signal. Hamamatsu manufactures the APDs used in the NOvA detector.

The working principle of the APD is as follows: When photons excite electron-hole pairs, a strong electric field, created by a high reverse bias voltage, accelerates these pairs. Through an impact ionization process, highly energetic electrons collide with other electrons, releasing them and creating a chain reaction of free electrons and holes. This avalanche effect results in a significant amplification of the photocurrent. The APD has a quantum efficiency of 85% for light signals with wavelengths in the range of 520-550 nm, allowing for the detection of low intensity light signals in long PVC tubes.

To reduce thermal noise and dark current (current generated in the absence of light), each APD is cooled to a temperature of -15^0C using a thermoelectric cooler (TEC). Cool water continuously flows to remove excess heat. To minimize surface currents, the APD is coated with paralene and dry nitrogen gas flows through a system of tubes to prevent ice formation on the surface. Each APD operates at a voltage of 425V, resulting in a gain of approximately 100. The signal is amplified by integrated circuits, and the FEB digitizes hits above the threshold and reads the analog signal from the APD. Hit information from the FEB is collected by a Data Concentrator Module (DCM).

3.2.4 Far Detector

The far detector consists of a total of 896 planes, comprising 344,064 channels. The active detector mass is 14 kt, with 65% of it composed of a liquid scintillator. The detector is constructed by combining two sets of 32 plane blocks, resulting in a total of 14 diblocks for the far detector.

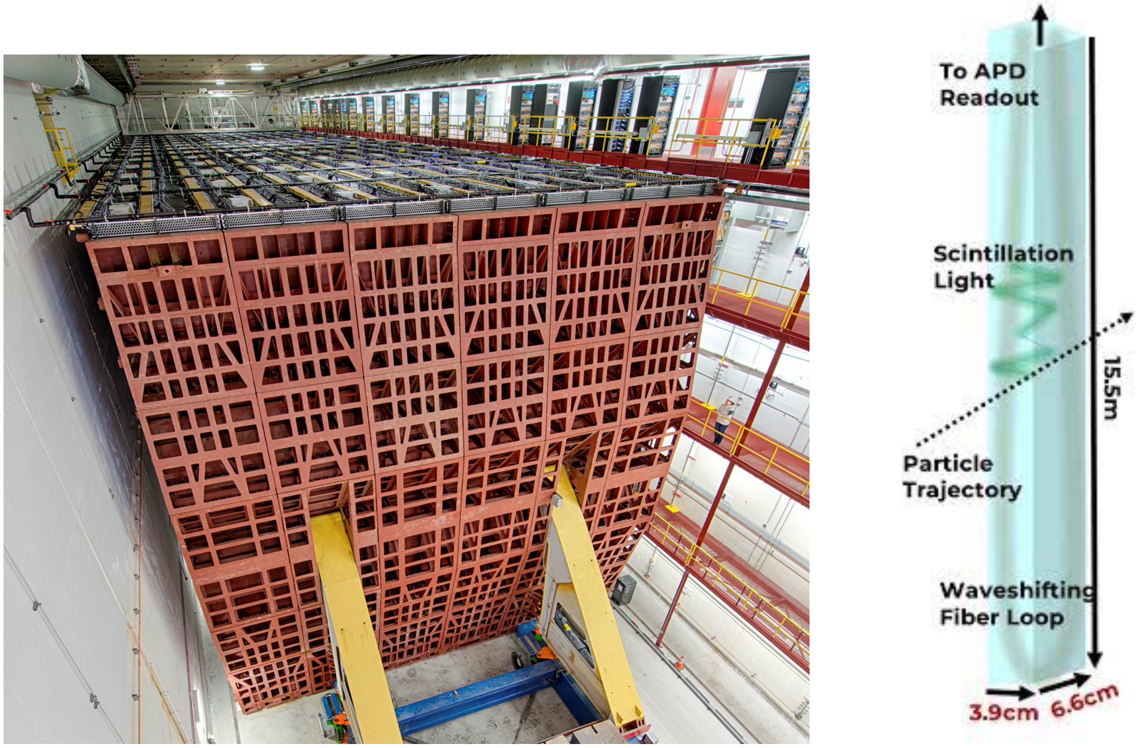

(a) (b)

Figure 3.7 NOvA far detector (a). Schematic diagram of NOvA cell, the walls are made up of PVC with a loop of wavelength shifting fiber is read out by one APD (b).

Each diblock in the far detector is equipped with 12 Data Concentrator Modules (DCMs), each containing 64 Front End Boards (FEBs). As the far detector is located on the surface, it is exposed to 50-70 cosmic rays during each 550-microsecond readout window. The main objective of the far detector is to accurately measure the energy spectra of beam neutrinos by distinguishing between charged-current interactions of muon and electron neutrinos and neutral-current interactions.

3.2.5 Near Detector

The near detector, located 105 meters underground, is specifically positioned at this depth to minimize interactions with cosmic rays. Additionally, its proximity to the NuMI beam, which is directed downward at an angle of 58 milliradians, allows for a significantly higher rate of neutrino interactions compared to the far detector. The purpose of the near detector is to accurately measure the unoscillated spectra of the beam neutrinos, which serves as a prediction for the spectra observed in the far detector. The detector itself has a length of 15.9 meters along the direction of the beam and is divided into two regions. The first region is the active region, measuring 12.67 meters in length, followed by a 3.23-meter-long muon catcher at the downstream end, as depicted in Figure 3.8.

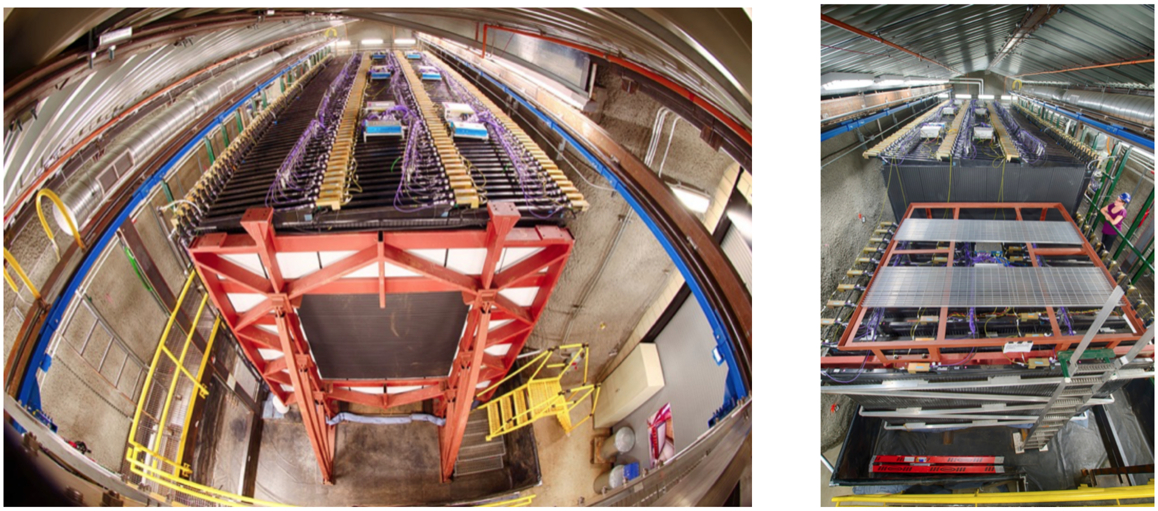
(a) (b)

Figure 3.8 near detector (a) and muon catcher region (b) with steel plates alternating with scintillation planes, whose height is two-thirds that of the active region.

The muon catcher in the near detector is designed to effectively capture muons by employing alternating steel and scintillating planes. The total mass of the near detector is 290 tons, with 130 tons dedicated to the liquid scintillator. The active region, which constitutes the majority of the detector's mass, weighs 193 tons and contains approximately 18,000 channels distributed over 192 planes. Following the active region, there are 22 additional planes and 10 steel planes, each with a thickness of 10 cm. The dimensions of the active region are 3.9 meters in height, 3.9 meters in width and 12.67 meters in length (h x w x l).

The electronics for the active region are divided into three diblocks, with each diblock accommodating two Data Concentrator Modules (DCMs) for both the vertical and horizontal planes. The DCMs are equipped with either 64 or 32 Front End Boards (FEBs) depending on their configuration.

As for the muon catcher, it consists of a periodic arrangement of horizontal and vertical planes made of steel and a liquid scintillator. In this section, there are two DCMs, one for the horizontal module and the other for the vertical module.

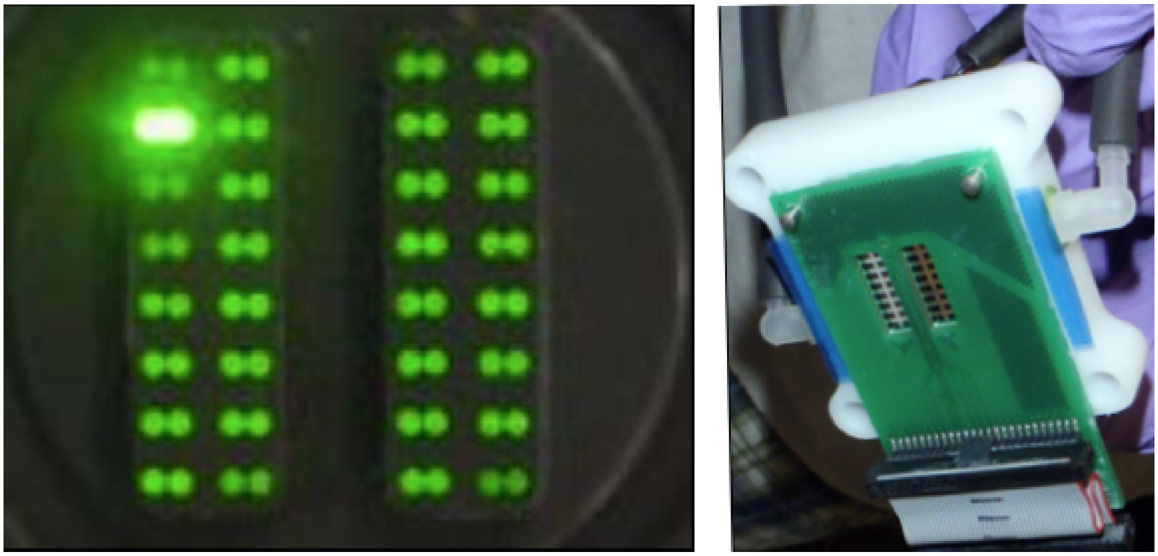
(a) (b)

Figure 3.9 The ends of 32 wavelength-shifting fibers collected at the end of scintillation cells to mount to an APD (a). The front face of an APD will be pressed against the fiber ends (b).

3.3 Overview of Data Acquisition System

The photon signal generated by 32 individual cells is amplified by an Avalanche Photodiode (APD). Each APD is connected to a single Front End Board (FEB) that contains four circuits. The voltage signal from the APD is then sent to an Application Specific Integrated Circuit (ASIC), which shapes the signal to enable timely hit detection. The output of the ASIC is further processed by an Analog-to-Digital Converter (ADC) to digitize the signal and identify hits that exceed the threshold. These threshold-passing hits are directed to a Field Programmable Gate Array (FPGA), where they are assigned a timestamp for each channel. The FPGA also handles the programming of rise and fall times in the ASIC, as well as the threshold in the ADC.

Another important component of FEBs is the Thermoelectric Cooler (TEC), which monitors and maintains the temperature of the APD at -15°C to ensure a stable gain. Each FEB digitizes the hits from 32 individual channels or pixels. A Data Concentrator Module (DCM) is connected to a maximum of 64 FEBs. In the far detector (FD), all 168 DCMs are connected to the maximum number of FEBs, while in the near detector (ND), the 14 DCMs are connected to between 22 and 64 FEBs. The DCM utilizes custom software to continuously collect data from nanoslices and combine them into 50 µs slices called microslices [58]. The FPGA in the DCM coordinates the pooling of data from the FEBs to form nanoslices, and if any header information is missing, the microslice is identified as corrupt.

During the construction of a microslice, the DCM performs integrity checks, and if any check fails, the microslice is flagged as corrupt. Corruption can occur due to various factors such as flipped bits or malfunctioning FEBs, and the exact cause is not always known.

If a DCM consistently generates a significant number of corrupt microslices, it indicates hardware failure, and the DCM is typically replaced. The schematic representation of the Data Acquisition (DAQ) data flow is illustrated in Figure 3.10.

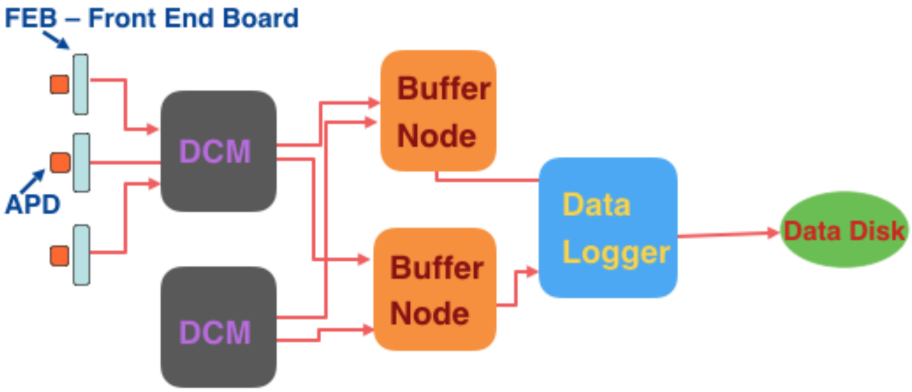

Figure 3.10 Schematic drawing of DAQ data flow.

The Data Concentrator Modules (DCMs) transmit microslices to buffer nodes in a round-robin fashion. Each DCM sends its first microslice to the first buffer node, the second microslice goes to the second buffer node, and so on. DCMs employ a simple algorithm to determine the appropriate buffer node for sending the microslice. The buffer node opens a millislice and collects microslices from each DCM. Once a millislice is complete, it is copied to shared memory, where it can be read by trigger messages from the Global Trigger. Each buffer node maintains a large pool of data, approximately 8GB in size. When a microslice is read out, it is not immediately deleted from the node. Instead, as new microslices arrive, the older ones expire and delete themselves.

If a buffer node does not have any microslices corresponding to a trigger, it will send an empty data block (a set of all triggered microblocks, which are sets of microslices from all DCMs) for that event. All data for a triggered event is sent to a single Data logger. The data logger waits until it receives data from every buffer node before writing the trigger event to the data disk. The data disk has the capability to save an event to multiple streams. In the far detector, the cosmic-ray event rate is high, approximately 100 kHz, since it is located on the surface. In contrast, the rate of beam neutrino events is low, only a few events per day. The NuMI beam spill trigger receives a timestamp from the Fermilab accelerator, with a time correction applied to account for the neutrinos' time of flight.

When the detector detects a NuMI beam spill, the buffer farm selects 1000 microblocks or 500 µs slices of data from the entire detector and writes them to the data disk. The beam data is collected within a 10 µs beam spill window, typically ranging from 218 µs to 228 µs. Each trigger has a start time, an end time, and a trigger ID. The detector also records data from other triggers for exotic searches, but those triggers are not the focus of this thesis.

The synchronization of the DAQ system in the NOvA detector is achieved through the timing system, and further details can be found in [59]. Timing Distribution Units (TDUs) function similarly to DCMs, as they send timing commands to all DCMs. Upon receiving a timing command, a DCM distributes it to all Front End Boards (FEBs). The FEBs are connected to the DCM via cables of equal length. The Master Timing Distribution Unit (MTDU) extracts timing information from the universal time based on its link to the Global Positioning System (GPS) and distributes the timing signal to the first Slave Timing Distribution Units (STDUs) in the chain. This synchronization process ensures that each channel in the NOvA detector is aligned and that the corresponding timestamps are recorded for each hit. Additionally, at Fermilab, the MTDU system is used to convert timestamps into NOvA time for the beam spill information received from the NuMI accelerator, with the corrected spill time then transmitted to the near and far detectors.

3.4 Performance of the NOvA Detectors

The monitoring of detector performance is crucial for the success of any particle physics experiment. In the case of the NOvA experiment, several tools have been developed to track and assess the performance of the detectors. Performance metrics, created using automated scripts, enable the monitoring of data quality. An important metric used to evaluate the overall performance of the detectors is the fractional uptime, as depicted in Figure 3.11.

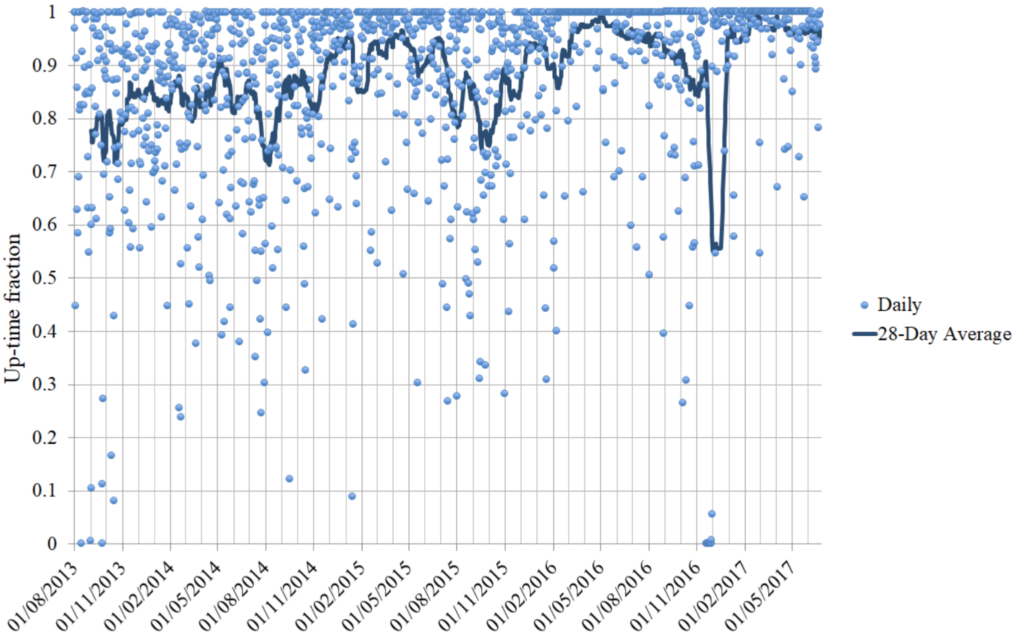

Figure 3.11 fractional uptime as a function of time. Uptime has steadily increased over the time as the experiment moved from commissioning to steady state running.

Ensuring maximum uptime is of utmost importance for the experiment. Despite having advanced tools for reconstructing neutrino kinematics, their usefulness is limited if the data was not recorded in the first place.

3.5 Exposure

Exposure plays a crucial role in scaling the distributions of selected events in the NOvA experiment. Livetime, detector mass, and protons on target (POT) are essential quantities for measuring useful exposure. Livetime is used to scale cosmic rays and electronic noise, while the active mass of the detector is necessary for accurate normalization, especially when certain parts of the detector are blocked. The production of neutrinos is directly related to the number of decayed pions, which in turn depends on the number of protons delivered to the graphite target. The neutrino exposure is meticulously tracked and stored in a database on a spill-by-spill basis. Cumulative neutrino exposure, both for neutrino and antineutrino modes, since the start of the NOvA experiment is depicted over time in Figure 3.12.

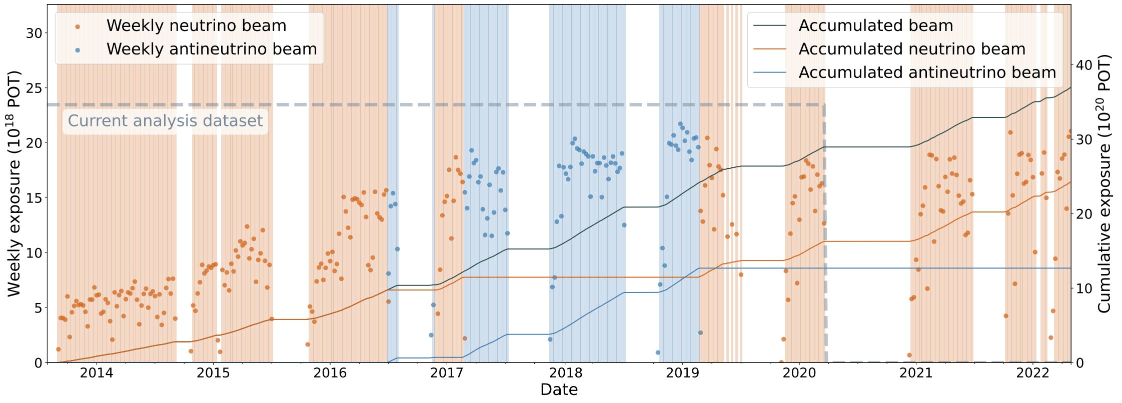

Figure 3.12 Weekly exposure and cumulative exposure vs date from starting of NOvA data taking in neutrino mode as well as anti-neutrino mode.

The accumulated POT for this analysis is the 3.14×10^{21} POT of the neutrino beam collected between August 2014 and February 2022.

Chapter 4

Event Simulation

Simulation is crucial for nearly all of our experiments, and it serves various purposes in data analysis. It provides an independent dataset for particle identification training and analysis optimization, helps estimate selection efficiency, and determines background components associated with signals. Researchers rely on simulation to make measurements and estimate parameters such as neutrino energy.

In the NOvA experiment, the simulation process consists of two main parts: beam simulation and detector simulation. The former simulates the creation of neutrinos, while the latter models how the detector behaves when exposed to those neutrinos. This chapter offers a comprehensive overview of the NOvA simulation chain, covering everything from neutrino production to the final recording of detector data.

4.1 Flux Prediction

The NuMI beam simulation begins by simulating the interaction between 120 GeV protons from the Main Injector and a graphite target. It concludes with the generation of flux files containing information about the simulated neutrinos, including their flavor types, directions, energy, and momentum. The expected flux from the NuMI beam is simulated using G4NuMI, a Monte Carlo simulation based on the GEANT4 framework [60].

G4NuMI simulates the production of hadrons when incoming protons interact with the NuMI target. It then traces the decay of neutrinos or the absorption of muons and hadrons by the downstream hadron monitors. Neutrinos generated from the decay of these particles are saved for future use in the simulation. Tracking all the final products of particles interacting with the target is computationally expensive and time consuming, so not every particle is individually tracked. Instead, the kinematic properties of the neutrino parents are saved in the flux files, along with information such as neutrino flavors, directions, decay points, momentum, and energy. This information can be later utilized to generate neutrinos that interact with the NOvA detectors. Additionally, retaining parent information aids in event re-weighting based on studies of hadronic models.

4.2 Neutrino Interactions

The GENIE (version 3.00) event generator [61] is used in the NOvA experiment to model beam neutrino interactions in the detectors. It takes a flux file as input and creates interactions in the detector volumes based on the neutrinos generated from the beam simulation. The GENIE model incorporates neutrino interaction cross sections to determine the energy of the interacting neutrinos. Various types of neutrino interactions (already explained in Chapter 1), such as quasi-elastic scattering (QE), resonance (RES), deep inelastic scattering (DIS), coherent scattering (COH), and meson exchange current interactions (MEC), are simulated using different cross-section models.

The GENIE model produces a list of final-state particles resulting from the interactions between the neutrinos and the detector material's nuclei. Kinematic information is saved for each particle. Quasi-elastic scattering follows the Llewellyn-Smith formalism described in Section 1.3.7, utilizing a dipole form with a default value of the axial vector mass (MA) of 0.99 GeV/c^2. The electromagnetic form factor is parameterized using the BBBA2005 model [62]. The Rein-Sehgal model [63] is used to simulate resonance neutrino-nucleus interactions, with a default value of the resonance axial vector mass (MA) set to 1.12 GeV/c^2. GENIE incorporates 16 out of 18 baryon resonances from its original paper.

The coherent scattering process is simulated using the Rein-Sehgal model, focusing on events within the low Q2 region, where the PCAC hypothesis predicts a single-dipole form factor. The deep inelastic scattering (DIS) interaction employs the Bodek and Yang model for low Q^2 values. Various cascade-hedronization models based on experimental measurements and theoretical models are available to determine the final-state particles and their kinematics, with the default model being the custom AGKY model in GENIE. For events with low invariant mass, the Koba-Nielsen-Olesen (KNO) scaling [64] is used, while the PYTHIA/JETSET model [61] is used for higher invariant masses. In GENIE an empirical MEC model is used to account for the discrepancies observed with data around 1 GeV in the Q^2 region between quasielastic and resonant events.

Final-state interaction (FSI) rates are derived from free hadron cross sections and the density of nucleons. GENIE employs the Introduce program to simulate final-state interactions. These models have large uncertainties, which directly affect the observed energy of neutrinos in experiments. GENIE also provides systematic uncertainty estimates for various parameters related to the cross-section models through global fits, enabling error bands to be placed on the predictions of various analyses.

The simulation includes not only the detector volume, but also the surrounding materials in the detector hall. Neutrino interactions in the near detector occur in the upstream rock, outside the detector hall, resulting in particle interactions in the detector alongside neutrinos that interact within the detector. To account for this, rock interactions are simulated separately and independently of in-detector events due to their computational complexity and cost. The number of simulated rock events is smaller and are randomly overlaid with the detector events to ensure that the total number of neutrino interactions in the detector is consistent with expectations. During the analysis cut stage, rock interactions are rejected, thus having a negligible impact on the analysis results.

4.3 Propagation of Particles

The output generated by GENIE [61] is entered into GEANT4 [60] to simulate the propagation of particles through the detector geometry. The geometry consists of the NOvA detectors, detector halls, and the surrounding rocks, which are described in CERN's Geometry Description Markup Language (GDML) files that are parsed by ROOT's geometry classes. GEANT4 simulates particle propagation and records energy depositions until the particles have less than 100 eV of kinetic energy remaining.

GEANT4 does not rely on a single modeling algorithm, especially for hadrons, to cover the entire energy range from zero to TeV and all known processes and particles. Instead, physical processes are simulated using different physics lists. Our standard physics list is QGSP BERT HP, which applies electromagnetic processes, utilizes the Bertini-style cascade (BERT) for modeling up to 9.5 GeV, and employs the Quark Gluon String (QGSP) model for high-energy (approximately 20 GeV and above) interactions involving protons, neutrons, pions, kaons, and nuclei. When high-energy interactions create an excited nucleus, it is passed to the precompound model for nuclear deexcitation. Additionally, a data-driven high precision (HP) neutron model is used to transport neutrons below 20 MeV down to thermal scattering energy. The output obtained from GEANT4 consists of the energy depositions of individual particles, which are particularly important for subsequent simulation steps.

4.4 Transport of Photon in Detector

GEANT4 calculates the amount of energy deposited by the particles in the NOvA detector cells. This energy deposition involves the conversion of scintillation light into electrons, which are then read out from each channel or cell. When more charge is produced in the Avalanche Photodiode (APD), it results in higher scintillation light production and therefore a greater amount of energy deposited in the cell. The scintillation light scatters, gets absorbed, and is transported through wavelength-shifting fibers, ultimately reaching the APD where the signal is detected. The captured signal is simulated using custom NOvA software developed internally by NOvA analyzers.

In order to determine the collection of scintillation photons by the fiber, a ray tracing algorithm has been developed (Figure 4.1). Several assumptions are made regarding the detector parameters, such as a scintillator emission time of 9 ns, and a uniform cell wall reflectivity of 87. 7% (Figure. 4.1), an index of reflectivity of 1.47 in oil, and an exponential photon capture probability with a capture length of 30.66 cm. As mentioned above in Chapter 3, all NOvA readout cells are treated identically, since they are composed of many identical cells. A template function is generated on the basis of a ray-tracing simulation to parameterize the transport of photons.

The transportation of photons through the fiber determines the expected number of photons arriving at the APD as a function of time, assuming that the photons are collected in the fiber. The captured photons are divided equally, with half traveling in each direction along the fiber, and they are attenuated based on measurements obtained from fiber quality control tests. Finally, the number of photoelectrons absorbed by the APD is determined, taking into account the quantum efficiency and Poisson statistics. Additionally, APDs exhibit excess noise, which introduces variance to the detected signal in addition to the Poisson variation caused by the number of photoelectrons captured by the APD. This excess noise is modeled using a theoretical distribution, specifically, a log-normal distribution.

4.5 Readout Simulation

The subsequent step in simulating the detector response involves the front-end board (FEB) electronics. The FEB consists of three chips: an application-specific integrated circuit (ASIC), an analog-to-digital converter (ADC) and a field-programmable gate array (FPGA). The ASIC's role is to preamplify and shape the signal produced by the photoelectrons. The pre-amplifier integrates the charge generated by the Avalanche Photodiode (APD), and a pulse is generated using a capacitor-resistor differentiator and a resistor-capacitor integrator (CR-RC) circuit. The pulse has a fast rise time controlled by an integrator unit and a slow fall time controlled by a differentiator unit. Pulse shaping was modeled using the analytical solution of the response of the CR-RC circuit to a unit charge impulse as

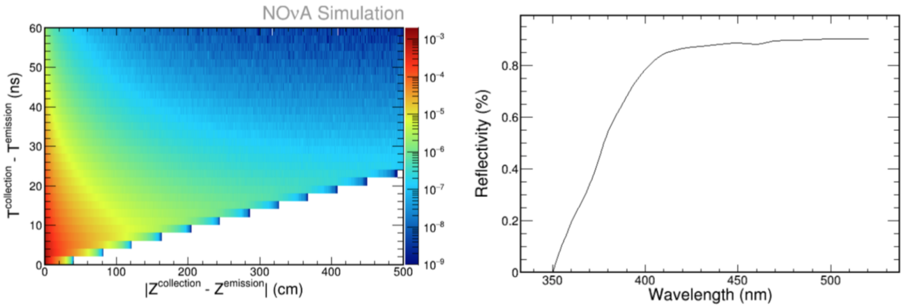

Figure 4.1 Template function of collection rate of scintillation photons (left).Cell wall reflectivity as a function of wavelength (right).

$$f(t) = \frac{F}{F-R}\left(e^{-\frac{(t-t_0)}{F}} - e^{-\frac{(t-t_0)}{R}}\right) \tag{4.1}$$

where t_0 is the time that the photoelectron pulse was collected by the APD, F and R is the fall and rise time of the CR-RC circuit, respectively. The pulse shaping process generates a signal that is fed into the analog-to-digital converter (ADC). When photoelectrons are produced by a cell, individual analog traces (equation 4.1) are created for each photoelectron and then combined to form the final trace. For the Far Detector (FD), four analog traces are digitized every 62.5 ns, while for the Near Detector (ND), eight analog traces are digitized. The digitization involves truncating the trace to integer values and constraining the values within the range of 0 to 4095 ADC counts. After digitization, a constant baseline offset is applied. The baseline value determines the dynamic range of the output signal before saturation.

In Monte Carlo simulations, the saturation peak has a sharp spike due to a constant baseline across all channels. However, in real data, the peak is broader and occurs at lower energies. The Gaussian distribution of the baseline is studied on a per-channel basis using Digital Scanning Oscilloscope (DSO) scans. At the beginning of each run, a baseline in ADC units is randomly drawn for each channel from a Gaussian distribution with specific mean and RMS values.

The trace is then converted from photoelectron units (PE) to ADC units using a conversion factor determined through charge injection studies. The baseline value is obtained from the distribution of modes observed in the pedestal scan.

Finally, the FPGA identifies peaks above a threshold in the dual-correlated sampling trace, which is defined as the difference between the current digitization sample (ADC_i) and the sample three time slices earlier (ADC_{i-3}).

Noise is also modeled for cells that do not contain actual physics hits. This is done using a data-driven method that generates noise hits from a template. The template is constructed by creating a 3D histogram based on the differences between adc1 - adc0, adc2 - adc0, and adc3 - adc0 for noise hits in the noise slice. This histogram is normalized by the product of livetime and the number of active channels for all sub-runs, reflecting the probability of recording a noise hit per channel and per unit time.

4.6 The APD Sag Simulation

In an avalanche photodiode (APD), the pixels are connected to a common voltage source that drives the multiplication of the avalanche. When a high-energy deposit occurs on one pixel, it causes a temporary decrease in voltage for all other pixels on the APD. This voltage decrease, known as “sag”, is influenced by ASIC and digital signal processing, which measure the differences between samples taken at different times. The sag recovers over time, representing a genuine energy deposit, and a digital value is created at the triggered time. The magnitude of the sag was found to be 0.0186 times the amplitude of the pulse on the channel with an actual energy deposit.

In order to simulate the sag effect, a sagged trace is generated by summing the light captured by all pixels of an APD that exceeds 5000 ADC within a 15 ns window. This is done even for pixels that do not contain actual physics hits. This modeling accounts for the flashing behavior observed in the data when high-energy cosmic rays pass through the detector.

4.7 CHERENKOV LIGHT SIMULATION

When a particle propagates through a medium and if the speed of light is faster than the speed of light through a medium, radiation is emitted called Cherenkov radiation [65]. The energy spectrum per unit length of the track is described by the Frank-Tamm formula [66]:

$$\frac{d^2N_\gamma}{dxd\lambda} = \frac{2\pi\alpha z^2}{\lambda^2}\left(1 - \frac{1}{\beta^2 n^2(\lambda)}\right) \tag{4.2}$$

where β is the speed of the particle, n(λ) is the refraction index, λ is the wavelength. The energy spectrum changes $\sim 1/\lambda^2$ if the refraction index changes slowly. At the wavelength between 400-500 nm, the scintillation light is absorbed by the wavelength-shifting fiber and the Cherenkov radiations are indistinguishable from scintillation light which amplifies our light production for fast particles. The Cherenkov light production as a function of wavelength for the different velocity of particles is shown in Figure 4.2. The refraction index of mineral oil used by NOvA is 1.47 and Cherenkov light represents roughly 4% of the light collected by fast particles, as shown in Figure 4.2.

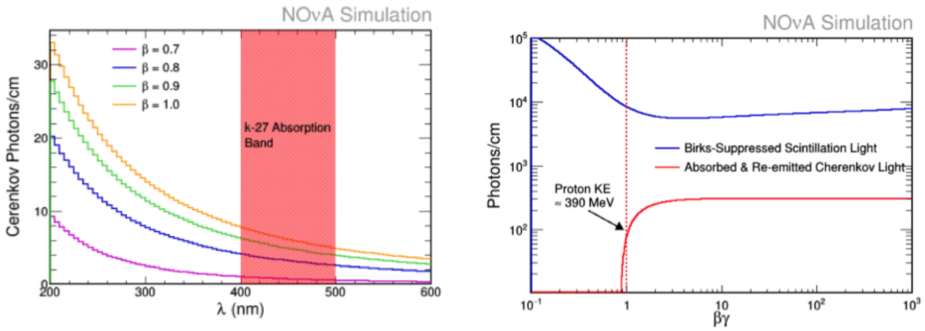

Figure 4.2 The Cherenkov light production as a function of wavelength for different velocity of particles (β) and the red shaded region is absorption spectrum of the k-27 dye in the optical fiber(left). The photon production comparison as a function of $\beta\gamma$ for scintillation is in blue and Cherenkov radiation is in red (right).

4.8 BIRKS-CHOU PARAMETERS

The relationship between energy deposition and light yield is determined using GEANT4. The light yield is directly proportional to the energy lost along the particle's path for lower energies. However, at higher energy-loss rates, organic scintillators experience recombination and quenching effects, leading to a reduction in the final light yield. Birks Law is an empirical model that attempts to capture this behavior by introducing a second-order correction term [67], [68]. Birks law is represented by the following equation:

$$\frac{dL}{dx} = \frac{L_0 \frac{dE}{dx}}{1 + k_B \frac{dE}{dx} + k_C \left(\frac{dE}{dx}\right)^2} \tag{4.3}$$

Here, k_B and k_C are the Birks' and Chou constants, respectively. These constants are determined by analyzing ND events with single muon and single proton tracks. A comparison is made between the $\frac{dE}{dx}$ distributions, as a function of the number of planes from the end of the track, in both data and Monte Carlo (MC). The values of $k_B = 0.040, \mathrm{gMeV}^{-1}, \mathrm{cm}^{-2}$ and $k_C = -0.0005, \mathrm{MeV}^{-2}, \mathrm{cm}^{-2}$ were found to produce the best match between the data and MC, taking into account the oversuppression in the last plane caused by the large Birks suppression. The negative contribution from the Chou constant helps mitigate this over-quenching effect.

There is a tunable parameter in the conversion factor that relates the energy deposited in the detector to the creation of scintillation photons. For the NOvA scintillator, the expectation of 3360 photons/MeV is set. During the tuning process, only 3/4 of the cell is used to avoid roll-off regions, and the scaling of the MC attenuation curves is adjusted to match the dimmer regions of the cell. The scaling factors for the X and Y views in the ND are determined to be 0.610058 and 0.598244, respectively. The data/MC comparison of the detector response to cosmic ray muons without offline calibrations for the ND is shown in Figure 4.3.

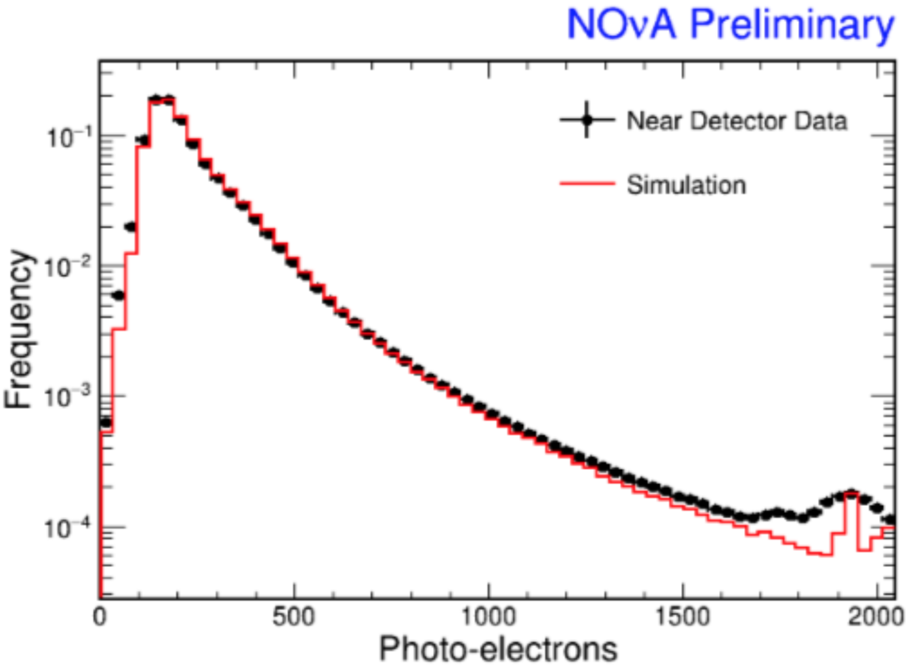

Figure 4.3 Comparing the photo-electron spectrum in cosmic rays between the ND data and simulation reveals a discrepancy. The difference observed at high photo-electron counts can be attributed to the fact that the gain in each cell of the detector is individually set in the data, whereas the simulation assumes a uniform gain value across all cells.

CHAPTER 5

EVENT RECONSTRUCTION AND CALIBRATION

5.1 RECONSTRUCTION

The NOvA experiment aims to reconstruct neutrino interactions in detail for analysis purposes. Different types of interaction have different event signatures. Charged current interactions involving electron neutrinos (ν_e) result in electromagnetic electron showers, while charged current interactions involving muon neutrinos (ν_μ) produce narrow muon tracks along their trajectories (Fig. 5.1). Neutral current interactions involving a single π^0 present challenges in reconstruction. The electromagnetic showers produced by the decay of π^0 into two photons can be difficult to distinguish from electron showers. Scintillating light is produced when photons convert into e^-/e^+ pairs, but before that conversion, the photons travel a certain distance (the photon conversion distance is $38cm$ or 6 planes). Hence, various reconstruction tools have been developed in the NOvA experiment to address different purposes. The reconstruction process is described in the following sections.

Raw data from the NOvA detectors, known as cell hits, are collected from the readout. These hits contain information about the plane, cell, time, and charge. The spatial and temporal correlations between the hits are then grouped into "slices" that form the basis for later-stage reconstruction (explained in Section 5.1.1). Straight-line features within the slices, serving as seeds, are identified using a modified Hough transformation (Section 5.1.2). The Hough lines are utilized to reconstruct a global 3D neutrino interaction vertex through an Elastic Arms algorithm (Section 5.1.3).

Prongs, defined as collections of cell hits with a start point and direction, are generated using the "fuzzy-k-means" algorithm and provide information about the particles' activity in the event, with the vertex as a seed (Section 5.1.4). Another tracking algorithm based on a Kalman filter produces reconstructed tracks from individual slices. The tracking algorithm aims to trace the trajectory of particles that deposit energy in the detector, which is particularly useful for identifying particles that do not produce large electromagnetic or hadronic showers, such as muons (Section 5.1.5).

5.1.1 Isolating Neutrino Interaction

NOvA's data collection involves capturing hits in $550\mu s$ read-out windows for the entire detector, although physics interactions occur within shorter timeframes. In the FD, which is located on the surface, the main challenge is to separate 50-70 cosmic rays within the $550\mu s$ read-out windows.

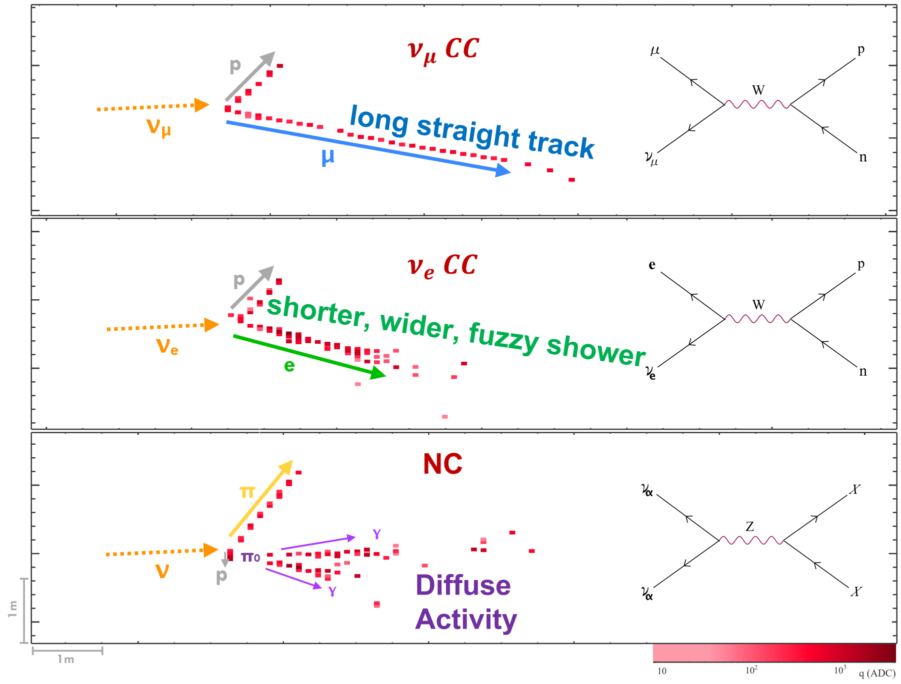

Figure 5.1 (ν_μ) CC neutrino interaction with long muon (top). (ν_e) CC neutrino interaction with electron shower (middle), Neutral current (bottom).

The ND, on the other hand, is designed to separate approximately 5 neutrino interactions within each 10-microsecond neutrino beam window. The beam spill, which represents the time period during which neutrino interactions from the beam are expected to occur, lasts only 10 microseconds. The time outside the beam spill is used to determine the background.

$$\epsilon = \left(\frac{|\Delta T| - |\Delta\vec{r}|/c}{T_{\text{res}}}\right)^2 + \left(\frac{\Delta Z}{D_{\text{pen}}}\right)^2 + \left(\frac{\Delta X \text{ or } Y}{D_{\text{pen}}}\right)^2 \tag{5.1}$$

where T_{res} is the timing resolution for the quadratic sum of two hits (time resolution for FD is $\sim$ 10 ns and for ND is $\sim$ 5 ns), D_{pen} is a distance penalty, ΔT is the time between two hits (order of nanoseconds), ΔZ and ΔX or Y are the distance between hits in each view (in cm). The hits which occurred in the same view of the distance can be written as $|\Delta\vec{r}| = \sqrt{\Delta Z^2 + \Delta X \text{ or } Y^2}$, however, for hits in opposite views $|\Delta\vec{r}| = \Delta Z$.

The slicing algorithm called the "Slicer," ensures that each slice contains a single interaction. The performance of the slicer is evaluated using two metrics: efficiency and purity. Efficiency measures the ratio of the energy deposited in a slice of a specific interaction to the total energy deposited in that slice from all interactions. Purity, on the other hand, measures the ratio of the energy deposited in a slice from a specific interaction to the total energy in that slice.

$$Efficiency = \frac{Energy\ deposited\ in\ slice\ from\ interaction}{Total\ energy\ deposited\ in\ slice\ from\ interaction} \tag{5.2}$$

$$Purity = \frac{Deposited\ energy\ in\ slice\ from\ interaction}{Total\ energy\ in\ slice} \tag{5.3}$$

In simulations of cosmic events in the FD, the slicing algorithm achieved efficiency and purity of 99.3%. In the ND neutrino simulations, the slicing algorithm demonstrated an efficiency of 94.4% and a purity of 98.5% [69].

5.1.2 Identifying Lines with Multi-Hough Transform

The next step after slicing is to identify lines in each slice using a modified Hough transform algorithm [70]. This algorithm takes as input pairs of points characterized by a straight line passing through them and parameterized in the polar coordinate system, where ρ gives the perpendicular distance from the line to the origin and θ gives the angle between ρ and the x axis. The algorithm makes lines and fits in each detector view separately. The line passing through each pair of hit points in the slice creates a Gaussian smear vote

After the slicing process, the next step involves identifying the lines within each slice using a modified Hough transform algorithm [70]. This algorithm takes pairs of points as input, which define a straight line passing through them and are parameterized in a polar coordinate system. In this system, ρ represents the perpendicular distance from the line to the origin, and θ represents the angle between ρ and the x-axis. The algorithm performs line fitting separately for each detector view.

For each pair of hit points in the slice, the line passing through them generates a Gaussian smear vote:

$$\text{vote } = e^{\frac{-(\rho-\rho_0)^2}{2\sigma_\rho^2}} e^{\frac{-(\theta-\theta_0)^2}{2\sigma_\theta^2}} \tag{5.4}$$

where $\sigma_\rho = \frac{3}{\sqrt{12}}, \sigma_\theta = \frac{3}{d\sqrt{6}}$ and d represents the distance between the two hits. The Hough transform creates a map by accumulating these votes in the phase space, and the peak in the map is identified as the line of interest. The algorithm iteratively creates new lines in the Hough map. It removes the last peak result from the Hough space and searches for new peaks among the remaining entries. This process continues until no more peaks above a defined threshold can be found in the Hough space. The algorithm aims to deliver the dominant Hough lines that pass through and intersect near the primary vertex of the slice.

The algorithm's performance in the Far Detector (FD) is measured in terms of the mean distance to the vertex for different types of interaction. For neutral current interactions, the mean distance is approximately 6.9 cm, while for muon neutrino charged current interactions it is around 4.1 cm, and for electron neutrino charged current interactions it is approximately 2.7 cm. The mean distance for the secondary Hough line is approximately 9.9 cm for the neutral current, 8.2 cm for the muon neutrino charged current, and 8.8 cm for the electron neutrino charged current [69].

5.1.3 IDENTIFICATION OF VERTEX USING ELASTIC ARMS

After the slicing and the Hough algorithm, the next step in the reconstruction process is to apply an elastic arm algorithm to each slice to locate the primary neutrino interaction point. This algorithm utilizes the lines generated by the Hough algorithm to seed a global 3D vertex point. The vertex is determined as the single point where the prong arms intersect within a slice. An elastic arm is a straight line defined by the polar angle θ_a and azimuth angle ϕ_a. It is described in Cartesian coordinates by the following equations:

$$x(s) = x_0 + sSin\theta_a Cos\phi_a \tag{5.5}$$

$$y(s) = y_0 + sSin\theta_a Sin\phi_a \tag{5.6}$$

$$z(s) = z_0 + sCos\theta_a \tag{5.7}$$

To determine the event topology accurately, the Elastic Arm algorithm [71] finds the parameters (x_0, y_0, z_0, $\vec{\theta}$, $\vec{\phi}$) by minimizing an energy function. The energy function is formulated as follows:

$$E = \sum_{i=1}^{N}\sum_{a=1}^{M} V_{ia}M_{ia} + \lambda \sum_{i=1}^{N}\left(\sum_{a=1}^{M} V_{ia} - 1\right)^2 + \frac{2}{\lambda_\nu}\sum_{a=1}^{M} D_a \tag{5.8}$$

Here, M and N represent the total number of arms and hits in the slice, respectively. M_{ia} is the distance from cell hit i to arm a, which is computed as the perpendicular distance from hit i to the projection of the arm in the two 2D detector views. The term M_{ia} is calculated as:

$$M_{ia} = \left(\frac{d_{ia}^{prep}}{\sigma_i}\right)^2 \tag{5.9}$$

where σ_i is a normalized factor (half of the cell depth $/\sqrt{12} = 0.9$ cm). V_{ia} represents the likelihood that hit i associated with arm a is assumed proportional to $e^{-\beta M_{ia}}$, and the noise is assumed to be a constant factor $e^{-\beta\lambda}$:

$$V_{ia} = \frac{e^{(-\beta M_{ia})}}{e^{(-\beta\lambda)} + \sum_{b=1}^{M} e^{(-\beta M_{ia})}}. \tag{5.10}$$

The distance D_a is the distance from the vertex to the first hit on arm a. β represents the range of influence, and the penalty terms are controlled by λ and λ_ν. The first 44 terms in equation 5.8 evaluate the goodness of fit between the arms and the hits, which minimizes when arm passes through the hits. The energy function evaluates the fit between the arms and the hits, penalizes arms that do not contain any hits, and considers the penalty for the vertex position being far from the first hit. The likelihood for a photon that propagates with a distance d before converting is proportional to e where $\lambda_\nu = 7/9x_0$ (30 cm), leads to a penalty term:

$$\chi^2 = 2lnL = \frac{2d}{\lambda_\nu} \tag{5.11}$$

The elastic arms are seeded for all the vertices, and the directions are scanned to minimize the energy cost function using ROOT's MINUIT class. The fit procedure starts with low values of β to avoid local minima and gradually adjusts β until the final vertex point is obtained within the slice.

The vertex resolutions indicate the performance of both the Multi-Hough and Elastic Arms algorithms. The resolutions are approximately 11.6 cm (about 2 NOvA cells), 10.9 and 28.8cm for ν_μ CC, ν_e CC, and NC events, respectively.

5.1.4 Prong Formation with Fuzzy k-Means

The subsequent step in the reconstruction process involves identifying prongs, which are clusters of hits with a start point and direction. To achieve this, we employ a possibilistic fuzzy-k means algorithm [72], [73]. This algorithm assigns a prong membership to each cell hit within the slice. The term "possibilistic" signifies that the sum of membership values across all prongs for a hit does not need to be unity, allowing for outlier hits to be treated as noise. This algorithm effectively separates noise hits. The "fuzziness" property allows a hit to belong to multiple prongs.

The fuzzy-k means algorithm generates prongs separately in the XZ and YZ views by utilizing the cell hits within the slice. It begins with a 2D view and subsequently matches the prongs between the two views to produce a 3D prong. The algorithm considers the vertex obtained from the Elastic Arms algorithm as the event's origin in both detector views. The cell hits within the slice manifest as peaks of deposited energy in a 1-D angular space around the vertex. Uncertainty is assigned on the basis of the distance from the vertex. The line connecting a cell hit to the vertex forms an angle with respect to the z-direction of the detector, ranging from $+pi$ to -π.

To determine the uncertainty associated with the angle, we model it after the multiple scattering of 1-2 GeV electrons and muons associated with each cell hit, considering its distance from the vertex position. In order to identify the prongs in angular space, we seed a prong and search for minima in dense cell hits using the density matrix w:

$$w_k = \sum_{i=1}^{n} e^{\left(-\frac{\theta_k - \theta_i}{\sigma_i}\right)^2} \tag{5.12}$$

here:

$$\theta_k = \pi + \frac{k * \pi}{180}, 0 \leqslant k < 360 \tag{5.13}$$

The process of associating each cell hit with a prong begins by assuming that there is a single prong centered on the region with the highest density of cell hits in angular space. The prong centers are then added and updated using an iterative method. The distance from each cell hit j to the prong center i is calculated as:

$$d_{ij} = \left(\frac{\theta_i - \theta_j}{\sigma_i}\right)^2 \tag{5.14}$$

and the prong membership is assigned with

$$U_{ij} = e^{-\frac{m\sqrt{a}d_{ij}}{\beta}} \tag{5.15}$$

In this case, the variable a represents the number of prong centers in the slice. The variable m is a measure of the fuzziness of the prongs and is set to 2, allowing membership to be shared between prongs. The variable σ is a normalization factor that represents the expected spread of hits around the prong center. Additionally, the prong centers are updated using:

$$\theta_i' = \theta_i + \frac{\sum_{i=1}^{n} \frac{U_{ij}^m}{\sigma_j} \left(\theta_j - \theta_i\right)}{\sum_{i=1}^{n} \frac{U_{ij}^m}{\sigma_j}} \tag{5.16}$$

The prong formation stage involves updating prong angles and adding additional prongs until all cell hits have at least a 1% membership in a prong or the maximum number of prong seeds has been reached. Prongs with significant membership overlaps are merged, while prongs with large spatial gaps indicating two co-linear particles are split.

After the prong formation stage, there are separate sets of 2D prongs for each view of the NOvA detector. The next step is to match the prongs between views to form 3D prongs. This matching process compares the energy profile of a prong in each view using a Kuiper metric. The Kuiper metric (i.e $K = D^{+} + D^{-}$) is calculated as the sum of the largest positive (D+) and negative (D-) distances between the energy profiles and used to find the best match for prong. In this case, $D^{+} = \max\Big(E^{XZ}(s) - E^{YZ}(s)\Big)$ and $D^{-} = \max\Big(E^{YZ}(s) - E^{XZ}(s)\Big)$, respectively (Figure 5.2, 5.3)

The performance of this algorithm is evaluated on the basis of the completeness of hits produced by the primary lepton in charged current (CC) interactions. For electron neutrino (ν_e) CC events, the average completeness is 88%, with 95% for quasi-elastic events and 86% and for non-quasi-elastic events. For muon neutrino (ν_e) CC events, the corresponding numbers are 93%, 98%, and 92% respectively.

5.1.5 Kalman Track

The Kalman algorithm [74] is a widely used track reconstruction algorithm in NOvA's muon neutrino disappearance analysis. It operates on individual slices and forms tracks separately in the XZ and YZ views of the detector. Initially, 2D tracks are created by seeding, where a seed segment consists of a pair of hits that are close together (less than 4 cells apart). The seed is then extended and additional hits are added using a Kalman filter, which utilizes the current track position and slope to propagate the track and incorporate compatible hits from the next cell. This process continues until no more hits can be added to the track.

Track propagation starts from the downstream end of the detector, moving towards the upstream direction, as particles emerging from the interaction are expected to be most separated in the downstream end. The propagation continues as long as there are consistent hits, and the probability of a gap between hits is below a threshold of 0.0001. Once the track reaches the upstream end, the propagation direction is reversed to pick up any missing hits from the initial propagation.

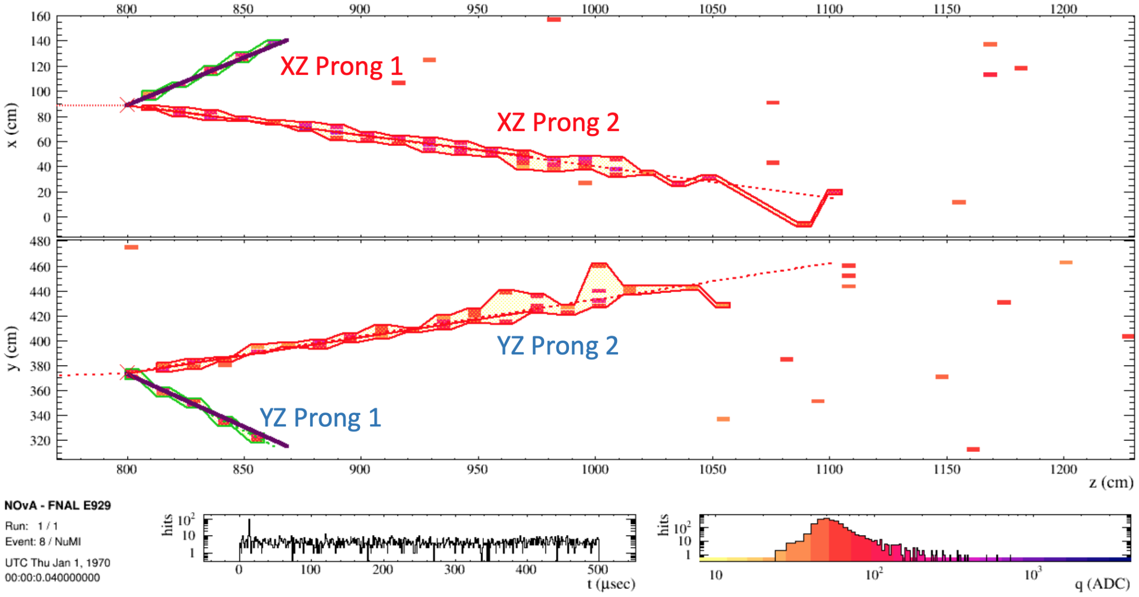

Figure 5.2 Illustration of the 3D prong reconstruction using the fuzzy-k means algorithm for a simulated ν_e CC QE process in the FD. The reconstructed prongs are visualized in the xz and yz views, with the electron prong displayed in red and the proton prong in green. The corresponding cumulative energy profile histograms, which are utilized to determine appropriate matches for the 3D prongs, are also depicted in the Figure 5.3 [75]

To ensure the quality of tracks, there is an optimization process that aims to maximize the efficiency of reconstructing long tracks, particularly for muons, while rejecting poorly reconstructed tracks.

After creating all the 2D tracks in each view independently, the next step is to match the 2D tracks from the two views. This matching is based on a score metric that quantifies the overlap of the 2D tracks in the z-direction of both views. The definition of the scoring metric is as follows:

$$S = \frac{Start_{diff} \ + \ Stop_{diff}}{Length\ of\ Overlap\ in\ z - direction} \tag{5.17}$$

$$Start_{diff} = |z_{low}\ of\ xz\ track\ \ - \ \ z_{low}\ of\ yz\ track| \tag{5.18}$$

$$Stop_{diff} = |z_{high}\ of\ xz\ track\ -\ z_{high}\ of\ yz\ track| \tag{5.19}$$

Matching begins with the lowest value of the scoring metric S and proceeds to higher values. The process of merging tracks is performed iteratively, combining 2D tracks to form a 3D track, until no further matches can be made.

5.2 CALIBRATION

The purpose of calibration is to convert the recorded signal into physically meaningful units of energy, ensuring a consistent detector response throughout the entire NOvA detector. Cosmic ray muons are employed for calibration as they provide a reliable source of energy deposition across the detector. The initial step in the calibration process involves selecting the hits associated with the reconstructed 3D cosmic muon tracks using the CosmicTrack algorithm. This algorithm fits a straight line to all the hits in a given slice and eliminates any hits that are inconsistent with the fit.

Additionally, a tri-cell criterion is applied to determine the track's path length through the cell. A tri-cell is defined as a cell that contains hits on a track and also has hits in the adjacent upper and lower cells in the same plane, as depicted in Figure 5.4. The calibration procedure is summarized in the calibration tech note [76].

If there are not enough statistics to meet the tri-cell criterion (let's say having a bad channel next to a good channel), one can require that the hit in the adjacent cell was also hit in the planes. For corner cells, there is no requirement on the tri-cell criterion (no adjacent cell) but rather an average path length over all the directions that the track can have is used. A 2D plot of the mean response (PE/cm) from tri-cell vs W is drawn for each cell; where W is the distance from the readout, W = 0 is the center of the cell along the fiber, and a positive value of W is closer to the readout end. The profile of 2D plot is taken and a cell-by-cell attenuation is performed after applying a threshold and shielding corrections. The threshold corrections refer

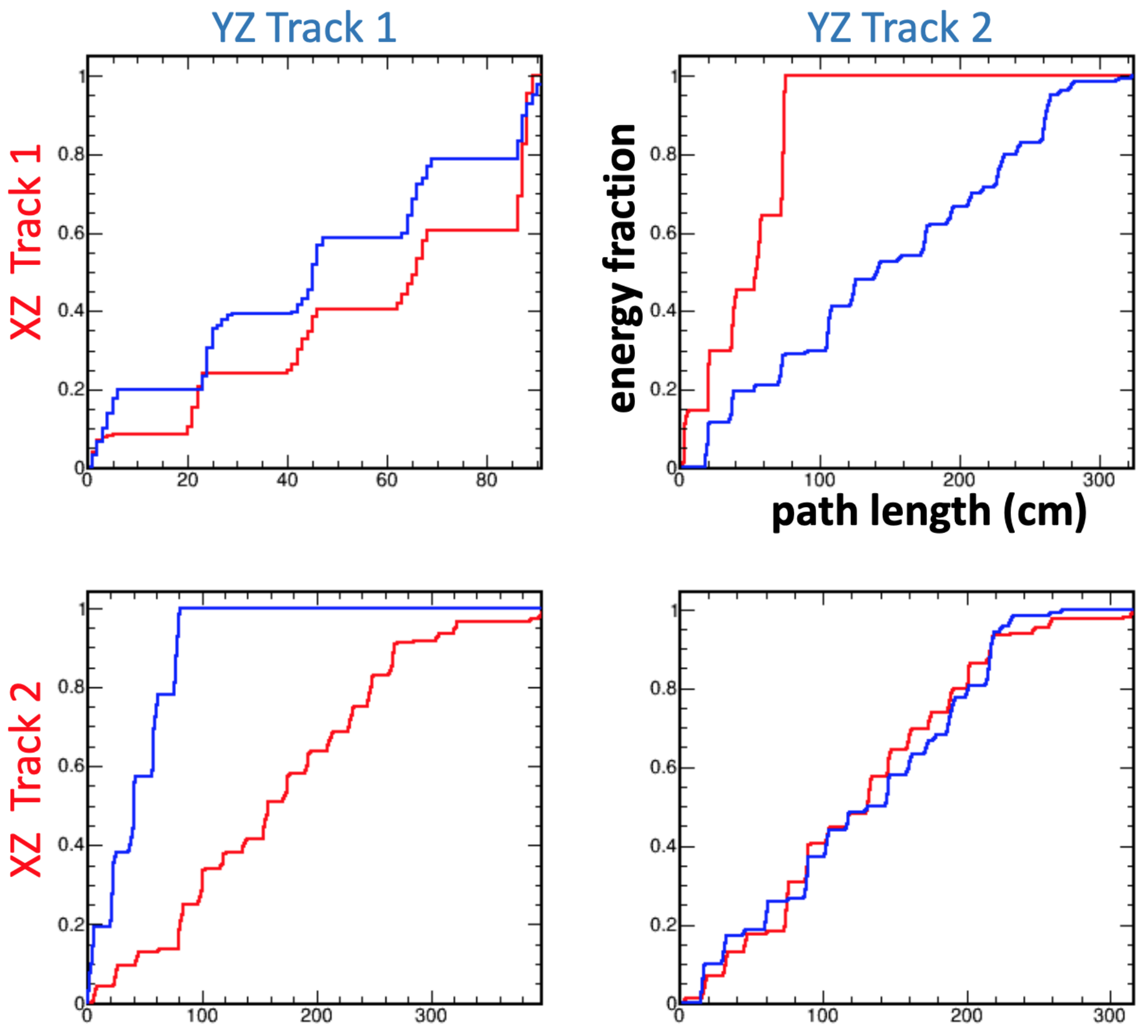

Figure 5.3 Representation of potential 3D match candidates as shown in Figure 5.2 displays the cumulative energy profile of prongs as a function of path length along the prong. The red and blue curves correspond to prongs in the XZ view (vertical planes) and the YZ view (horizontal planes), respectively. In the upper-left and lower-right figures, the preferred matches are shown, indicated by the green and red tracks, respectively. These matches exhibit similar energy profiles. The off-diagonal elements demonstrate the dissimilarity in energy profile shape for incorrect combinations [75].

to a minimum number of hit requirements for reaching APD as it slightly upwards fluctuation in the number of photons produced by the energy deposition. Shielding is defined as the average visible energy depositions from minimum ionizing particles (MIPs) that are not truly spatially uniform in the detector due to their own mass of the detector. To account for these two effects a correction factor is applied in each

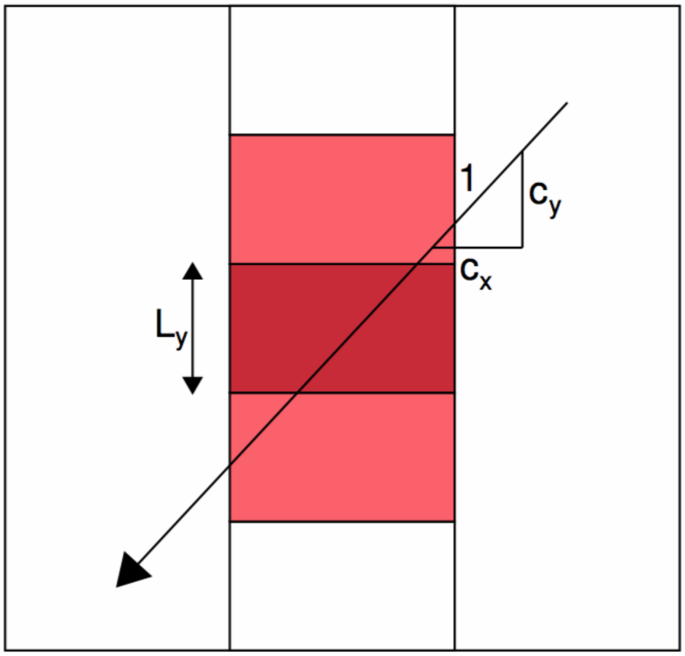

Figure 5.4 The process of selecting tri-cells related to a cosmic ray muon involves identifying specific cells based on their neighboring cells being triggered by the same cosmic ray. In the illustration, the dark red cell represents a tri-cell since its adjacent cells are also triggered by the same cosmic ray. The path length within this cell is determined by the variable L_y/c_y.

cell defined as :

In cases where the tri-cell criterion cannot be met due to insufficient statistics, an alternative requirement can be imposed. This involves ensuring that the hit in the adjacent cell was also registered in the corresponding planes. For corner cells where there is no adjacent cell, the tri-cell criterion does not apply. Instead, an average path length across all possible track directions is used.

To assess the response of each cell, a 2D plot is created, depicting the mean response (PE/cm) (in photoelectrons per centimeter) as a function of distance from the readout, denoted as W. In this plot, W = 0 represents the center of the cell along the fiber, and positive values of W indicate proximity to the readout end. The profile of the 2D plot is analyzed, and cell-by-cell attenuation is performed after applying threshold and shielding corrections.

Threshold corrections account for the minimum number of hits required to trigger the avalanche photodiode (APD), compensating for slight fluctuations in the number of photons generated during energy deposition. Shielding corrections, on the other hand, address the non-uniform distribution of visible energy depositions from minimum ionizing particles (MIPs) within the detector, which arises due to the detector's own mass. To correct for these effects, a correction factor is applied to each cell, as defined by the given equation:

$$\mathrm{T} = \frac{\mathrm{PE}}{\lambda} \cdot \frac{\mathrm{E}_{\mathrm{True}}}{\mathrm{E}_{MIP}} \tag{5.20}$$

where T is the combined threshold and shielding correction factor, PE is the number of simulated photoelectrons registered by the electronic readout, λ is the number of simulated photons seen at the readout without fluctuations, $\mathrm{E}_{\mathrm{True}}$ is the true energy deposited in the cell and E_{MIP} is the energy expect to be deposited and it depends on the path length through the cell.

5.2.1 Attenuation Correction

The light within the detectors undergoes attenuation as it travels through the wavelength-shifting (WLS) fiber. This fiber serves the purpose of transporting the light generated by a charged particle passing through the scintillator to the avalanche photodiode (APD). The process of attenuation calibration aims to correct the amount of energy deposited in the detector and registered by the APD. This calibration is denoted as PECorr, representing the corrected number of photoelectrons, regardless of the position where the energy was deposited.

The ADC/cm (analog-to-digital converter per centimeter) is recorded for a specific cell by creating a 2D histogram with W (distance from the readout) as the variable.

Prior to constructing the histogram, a correction factor is applied, taking into account the threshold and shielding effects. The 2D histogram profile is formed by calculating the median value within each W bin, and then fitted to a double exponential function that considers both the travel of light along short and long paths. The functional form of this fit is as follows:

$$\mathrm{y} = C + A\left(e^{\frac{\mathrm{w}}{\mathrm{X}}} + e^{-\frac{\mathrm{L+W}}{\mathrm{x}}}\right) \tag{5.21}$$

Where L represents the total length of the cell, and C, A, and X are parameters that can be adjusted freely. Parameter X provides the attenuation length of the cell. The fitting process encompasses the central portion of the cell, which corresponds to the range of [-150, 150] cm for Y view ND Muon Catcher cells and active cells, and [-150, 50] cm for X view ND Muon Catcher cells. Hits near the beginning and end of the cell exhibit distinct characteristics compared to the majority of hits within the cell. This discrepancy arises because the light that reaches the white PVC cell walls is reflected back into the scintillator. On the contrary, the top of the cell is constructed from black plastic, which has a lower reflectivity and consequently results in greater light loss. To correct for this effect, a polynomial function is introduced in the exponential form mentioned above at the two ends of the cell. The roll-off behavior is empirically defined as follows:

$$\mathrm{y} = \begin{cases} 1 - \alpha_R \left(W - W_R\right)^4, & \text{if } W > +W_R \\ 1, & \text{otherwise} \\ 1 - \alpha_L \left(W - W_L\right)^4, & \text{if } W > -W_L \end{cases} \tag{5.22}$$

This scenario presents another situation where significant discrepancies are observed in certain cells. These discrepancies arise due to variations in the position of the fiber within the cell. Typically, the fiber is placed along the corners of the cell. However, if the fiber somehow deviates and moves towards the central part of the cell, it captures a greater amount of light than anticipated, leading to these deviations. In such instances, the exponential function fails to accurately characterize the response. A LOWESS(Locally Weighted Scatter plot Smoothing) fit is done using a tricube weight,

$$\mathrm{w}_i = \begin{cases} \left(1 - \left|\frac{W - W_i}{\sigma}\right|^3\right)^3, & \text{if } |W - W_i| < \sigma \\ 0 & \text{if } |W - W_i| \geq \sigma \end{cases} \tag{5.23}$$

In the given expression, W_i represents the neighboring point i^{th} surrounding a local point. w_i represents the weight assigned to W_i, and W represents the local point on the curve. The range of measurements that affect the value of W is indicated by σ, which is set at 30cm. An illustration of complete attenuation fits for NOvA ND is presented in Figure 5.5. Figure 5.6 provides examples of the cell view for the ND before and after calibration, both horizontally and vertically. Attenuation calibration incorporates all of the aforementioned conditions to achieve a smoother cell response.

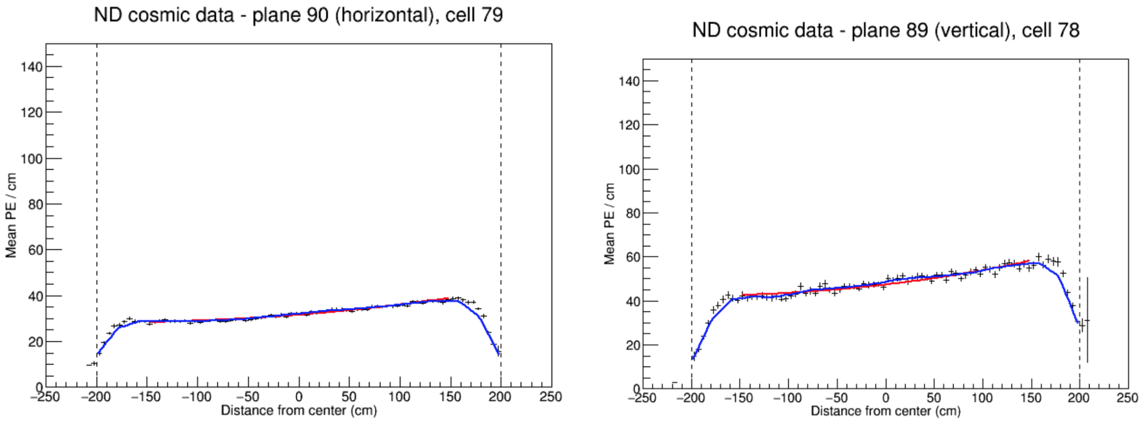

Figure 5.5 Examples of well-fitted attenuation curves with LOWESS corrections for the ND. The blue curve represents the full attenuation fit that incorporates the LOWESS fit, while the red curve represents the double exponential fit. The plot on the left corresponds to the horizontal view cells, while the plot on the right corresponds to the vertical view cells.

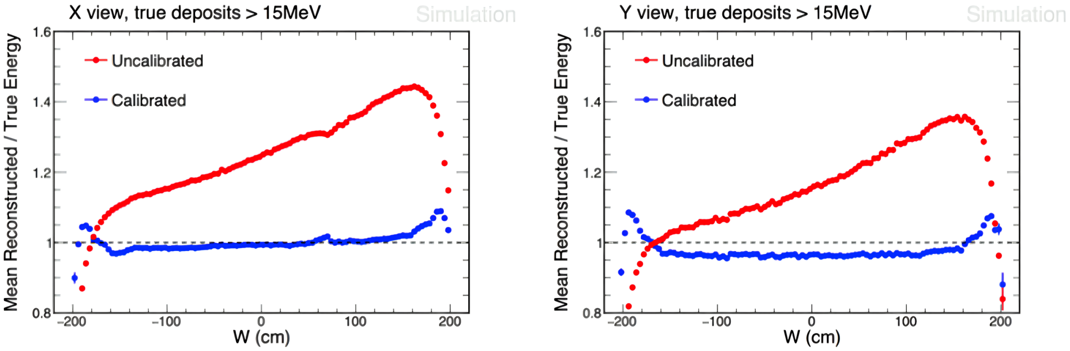

Figure 5.6 Examples of the ratio between the mean reconstructed energy and the true energy as a function of W. The red dots represent the results before the calibration is applied, while the blue dots represent the results after the calibration is applied. The plot on the left corresponds to the horizontal view cells, while the plot on the right corresponds to the vertical view cells.

5.2.2 Absolute Energy Scale

The primary objective of absolute energy calibration is to convert the relative corrected scale, represented in arbitrary units known as PEcorr/cm, into a physical energy scale measured in GeV/cm. In order to achieve this, the absolute calibration process utilizes stopping cosmic ray muons instead of muons that pass through the entire detector, in addition to the tri-cell criterion. Stopping muons are identified by the presence of a Michel electron at the end of the muon track, resulting from the muon decay ($\mu \rightarrow e^- + \nu_e + \nu_\mu$), which can be accurately described using the Bethe-Bloch formula. The Bethe-Bloch equation is applied to estimate the amount of energy lost through ionization within the scintillator while ignoring the energy deposition through the PVC material. Also, the determination of scale factor for absolute calibration is the ratio between the mean of the muon energy unit $\mathrm{MEU}_{\mathrm{truth}}$ to mean of the $\mathrm{MEU}_{\mathrm{reco.}}$ MEU is the mean of the detector response in units of PECorr (or simulated energy deposition in MeV) to a stopping muon tri-cell hit within the track window ($100 - 200$ cm) divided by the path length. In the NOvA liquid scintillator (consisting of chains of polyethylene), the expected energy loss per unit length due to a minimum ionizing particle is 1.79 MeV/cm.

The energy depositions occurring between 100 and 200 cm from the end of a track are considered to be within the minimum ionizing particle (MIP) region in the detector, which is utilized for determining the absolute energy calibration. Corrected photo-electrons per length (PECorr/cm) distribution between the data and simulation is shown in Figure 5.7. The scale factor is used to convert the PECorr/cm in data to MeV/cm. In this approach, we calibrate NOvA detectors independently and the constant is stored in the database, also they stored for different time periods so that a PE signal in raw digit object is converted to an energy unit.

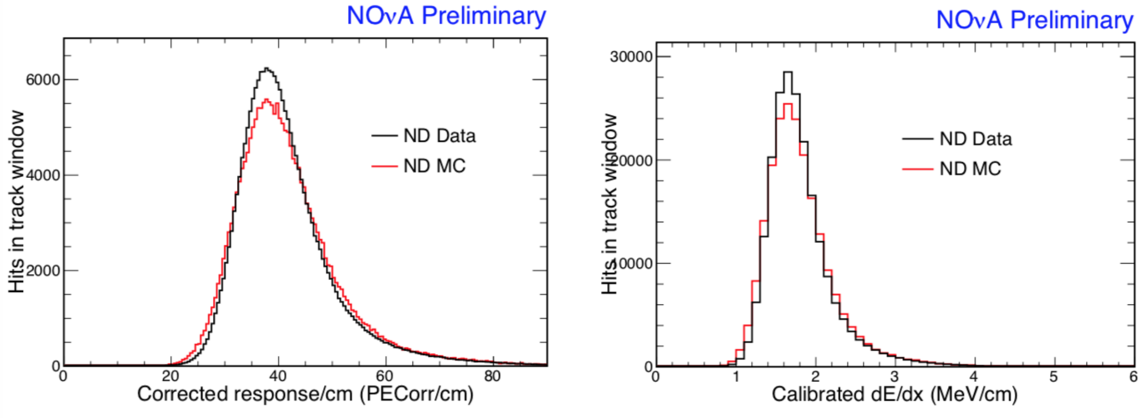

Figure 5.7 The graph on the left shows the corrected response of the detector as a function of the distance from the track end in both the ND data and Monte Carlo (MC) simulations. On the right, the graph illustrates the calibrated energy distribution per unit path length as a function of the distance from the track end in the ND data and MC simulations.

CHAPTER 6

SELECTION OF ν_μ CHARGED CURRENT COHERENT π^+ EVENTS

As discussed in Section 1.3.7 ν_μ induced charged current coherent interactions create two final state particles in the near detector (muon and a pion). The signal definition made for analysis is ν_μ coherent charged current events formed within the fiducial volume. All other events will be treated as background events. An event display view of a clean signal event simulated in NOvA near detector is shown in Figure 6.2. Event selection is capable of separating signal events from the background with an absolute efficiency of 1.42% and 59% purity and will be explained in a later section.

Before diving into the signal estimation for the cross-section analysis is performed, basic selection (preselection) criteria are enforced to ensure good data-taking conditions. Pre-selection is defined to ensure removal of poorly reconstructed events, removal of events that are near the edges of the detector, removal of events with more or less than two 3D reconstructed prongs for the two final-state particles (muon and pion) due to reconstruction inefficiencies, removal of events that are not fully contained in the containment volume (as explained in Section 6.3) to precisely reconstruct 4-momenta of final-state particles and finally remove events that contain particle candidates other than muons in muon candidate Kalman tracks. The data quality criteria and the containment requirement are borrowed from NOvA ν_μ Charged Current inclusive cross analysis [77].

The pre-selection consists of the following selection criteria:

- Data Quality cut
- Fiducial cut
- Two Prong cut
- Containment cut
- Muon ID cut

6.1 Data Quality

Data quality criteria are intended to remove detector noise and poorly reconstructed events for which particle four-momenta cannot be reliably estimated.

- Hits per slice > 20: A lesser number of hits in an individual slice is likely due to neutral current interaction or a partially reconstructed event.
- A vertex is reconstructed: An interaction vertex is required for downstream reconstruction algorithms. If a vertex was not reconstructed, the hits clustered by the slicing algorithm are likely noise.
- At least one track: Since there are two final-state particles expected, this analysis relies on the formation of tracks and prongs for the estimation of final-state particle kinematics.
- Number of continuous planes > 4: This requirement is enforced for both the XZ and YZ views of the detector to ensure there is enough energy deposition in the detector to reliably reconstruct the particle's energy.

6.2 Fiducial Volume

We optimize the fiducial volume for this analysis by applying Data Quality cut for NOvA production version 5.1 forward horn current Monte Carlo events. In this case, the chosen figure of merit function is **Sensitivity** and is defined as follows:

$$Sensitivity = \frac{Number\ of\ selected\ Signal\ Events}{\sqrt{Number\ of\ selected\ (Signal\ +\ Background)\ Events}} \tag{6.1}$$

In this case, Signal events are charged with current coherent events. We calculate the cumulative signal (in red), the cumulative background (in blue), and the sensitivity (in black) for each coordinate separately. The lower and upper thresholds for each (x, y, z) coordinate were determined based on the coordinate values that maximize sensitivity. As shown in Figure 6.1, six different figures of merit graphs (area normalized) (two figures of merit graphs to determine lower and upper thresholds for each coordinate) were made to finalize the boundaries of the fiducial volume.

Therefore, the optimized fiducial volume considered in the ν_μ charged-current coherent analysis is the following:

$$-160.0 < X(\text{cm}) < 170.0 \tag{6.2}$$

$$-150.0 < Y(\text{cm}) < 160.0 \tag{6.3}$$

$$50.0 < Z(\text{cm}) < 1200.0 \tag{6.4}$$

The graphical representation of the fiducial volume (in blue) can be seen in Figure 6.3.

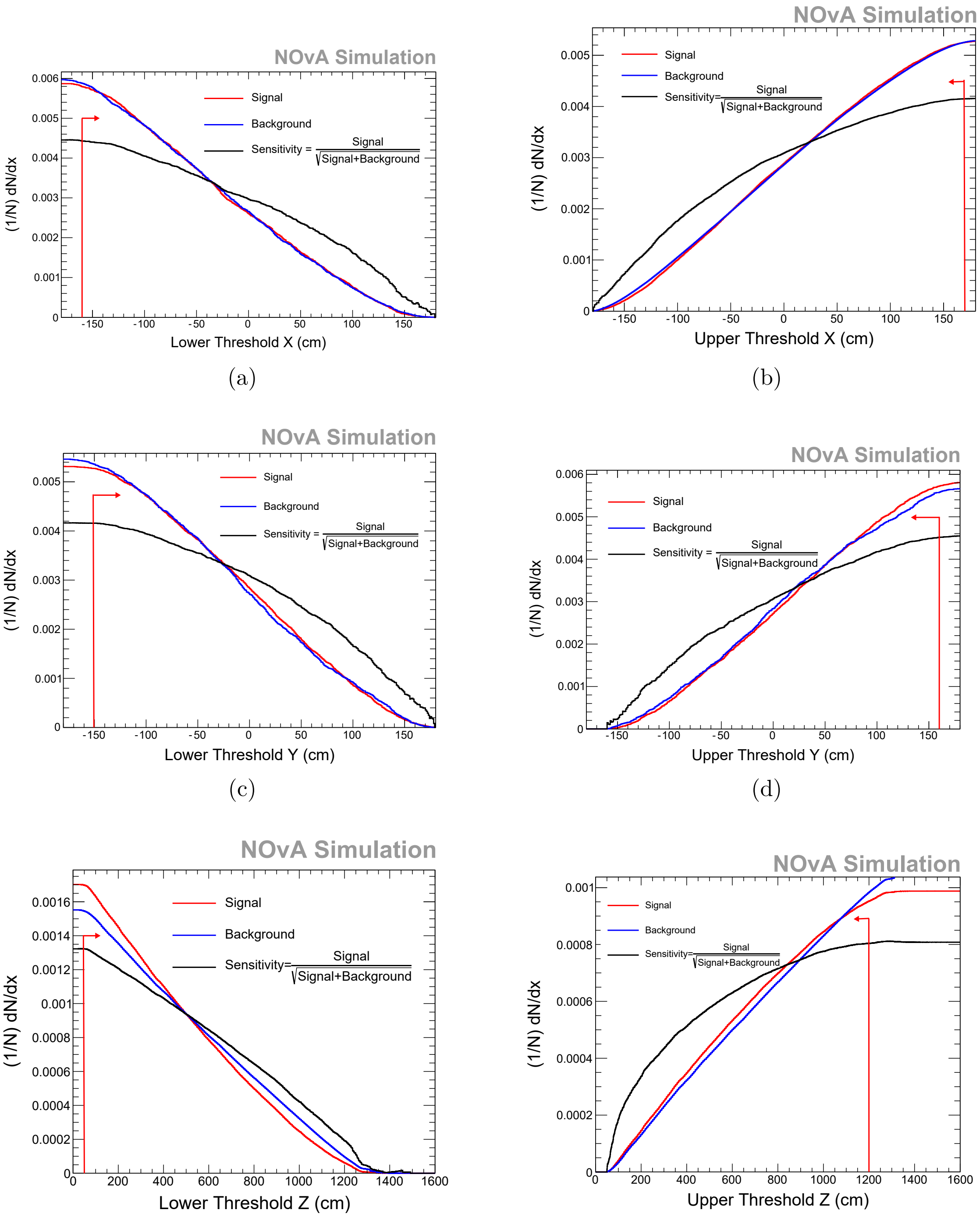

(a) (b)

(c) (d)

(e) (f)

Figure 6.1 Optimizing Fiducial Volume using Figure of merit plot: Sensitivity

6.3 EVENT TOPOLOGY

Under ideal reconstruction, the expected number of 3D prongs is two with zero 2D prongs. Due to reconstruction inefficiencies (such as the failure to identify pion interaction at the end of the trajectory), there will be other topologies, as shown in Figure 6.2 (b) (Histogram of the number of 2D vs. 3D Prongs normalized to data POT). To accurately calculate the kinematics of the two final-state particles (i.e. μ^- and π^+) it is required to select events that only contain two 3D-reconstructed prongs with zero 2D prongs. The selected topology and the event display are shown in Figure 6.2 (a), also known as the golden event sample!

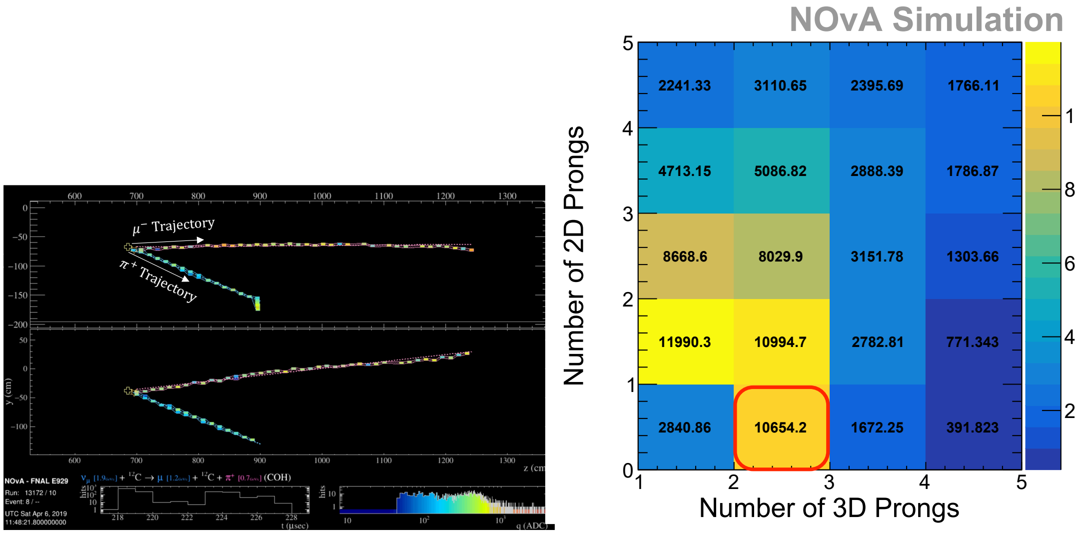

(a) Event display view of clean Charged-Current Coherent event

(b) Histogram of 3D Vs 2D prongs

Figure 6.2 Selected Topology used for analysis (i.e. events that only contain two 3D prongs and zero 2D prongs)

6.4 CONTAINMENT

In this case, the same containment cut defined in the inclusive analysis of CC was used (as described in **docdb-32688-v3**). After selecting muon candidate Kalman track (as explained in section 6.5

- The forward projection of the muon candidate track is greater than 5 cells from the edge of the detector. This aims at removing events with uncontained muons.
- The backward projection of the muon candidate track is greater than 10 cells from the edge of the detector. This is to remove contamination from neutrino interactions outside the detector.
- Remove all events with muon candidate tracks that could have exited the active region of the detector before reentering the muon catcher ("air gap events"): the end z-position of the track is less than 1275 cm or $(trk.kalman.tracks[ibesttrk].stop.Z() < 1275 \ ||$ $trk.kalman.tracks[ibesttrk].trkyposattrans < 55)$.

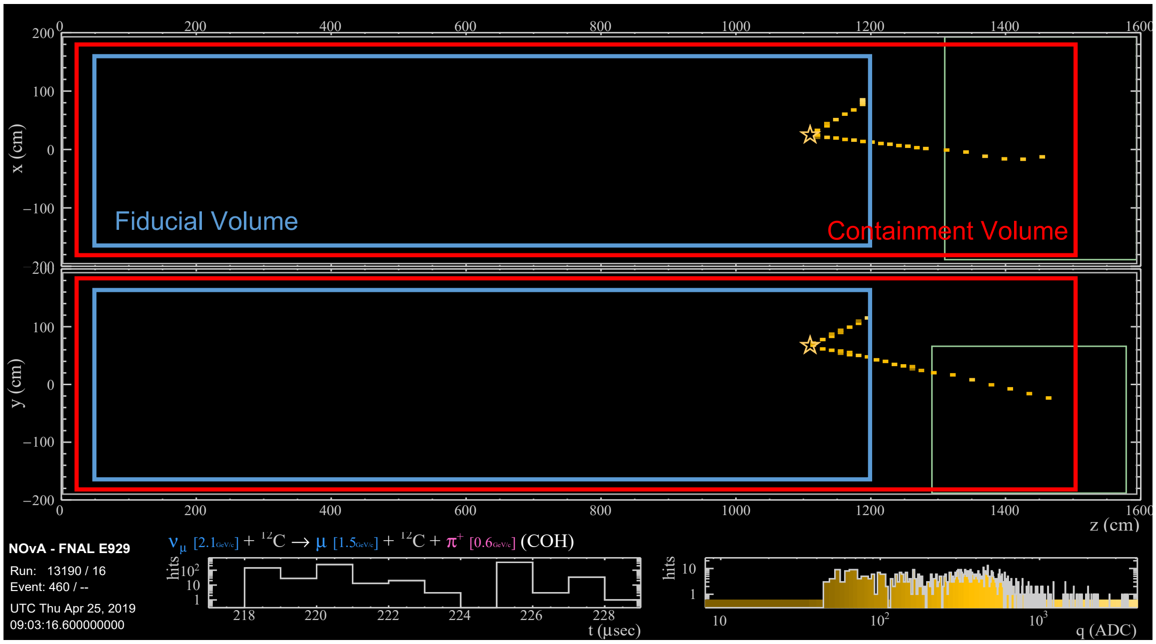

Figure 6.3 Graphical representation of the fiducial and containment volumes defined to study charged current coherent events

6.5 Muon Identification

Signal events are selected using an optimized cut on a BDT-based muon identifier developed for the ν_μ CC inclusive analysis (as described in **docdb-32688-v3**) MuonID. MuonID is trained to identify muons by considering properties of reconstructed tracks: muon likelihood of track dE/dx, muon likelihood of a scattering metric based on the angle and length of the scattering between the scattering events, dE/dx in the last 10 cm of the track, and dE/dx in the last 40 cm of the track. The plots of the inputs used to train the BDT are shown in Figure 6.4. The correlation matrices made for the signal and background tracks are shown in Figure 6.5.

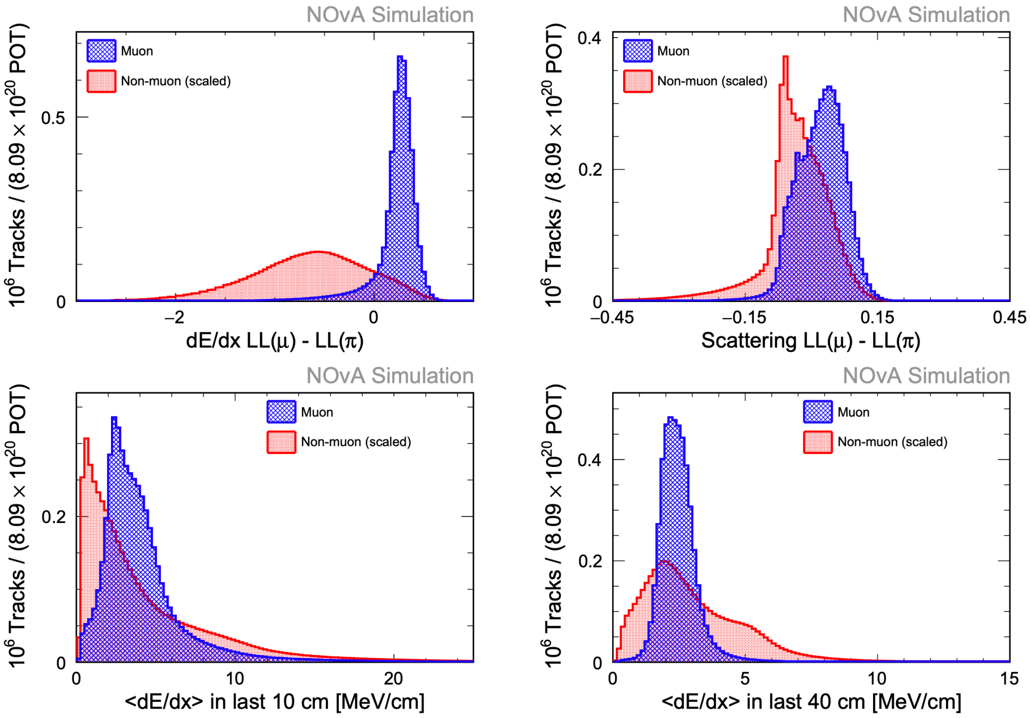

Figure 6.4 Simulated muon (hashed blue) and non-muon (dashed red) track distributions in: dE/dx log-likelihood differences between that of a muon and a pion (top left), multiple scattering log-likelihood differences (top right), average dE/dx in last 10 cm (bottom left) and average dE/dx in last 40 cm (bottom right) used in the MuonID selector [77].

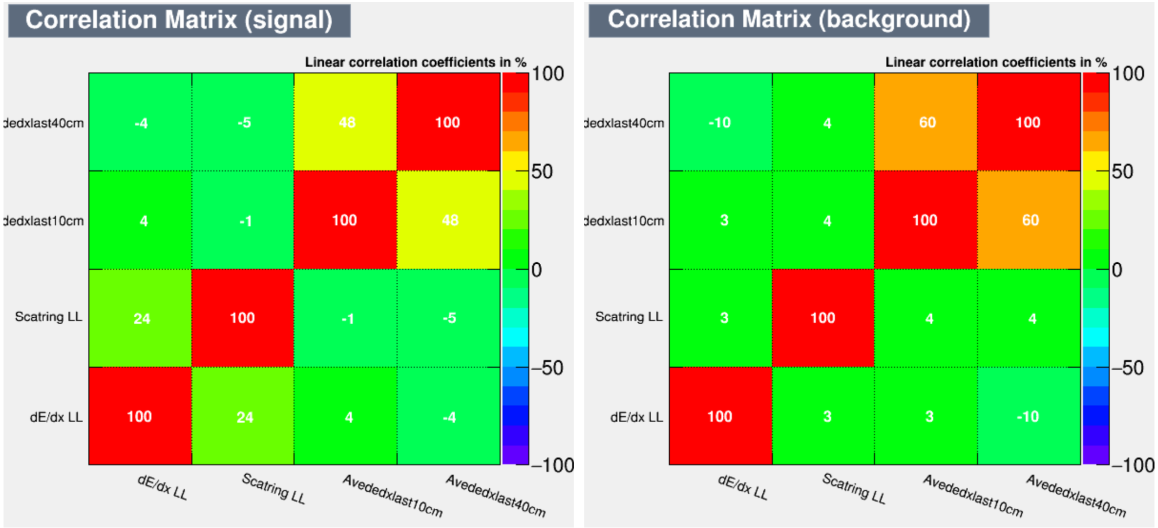

Figure 6.5 Correlation matrix of MuonID input variables for signal tracks (left) and correlation matrix of input variables for background tracks (right) [77].

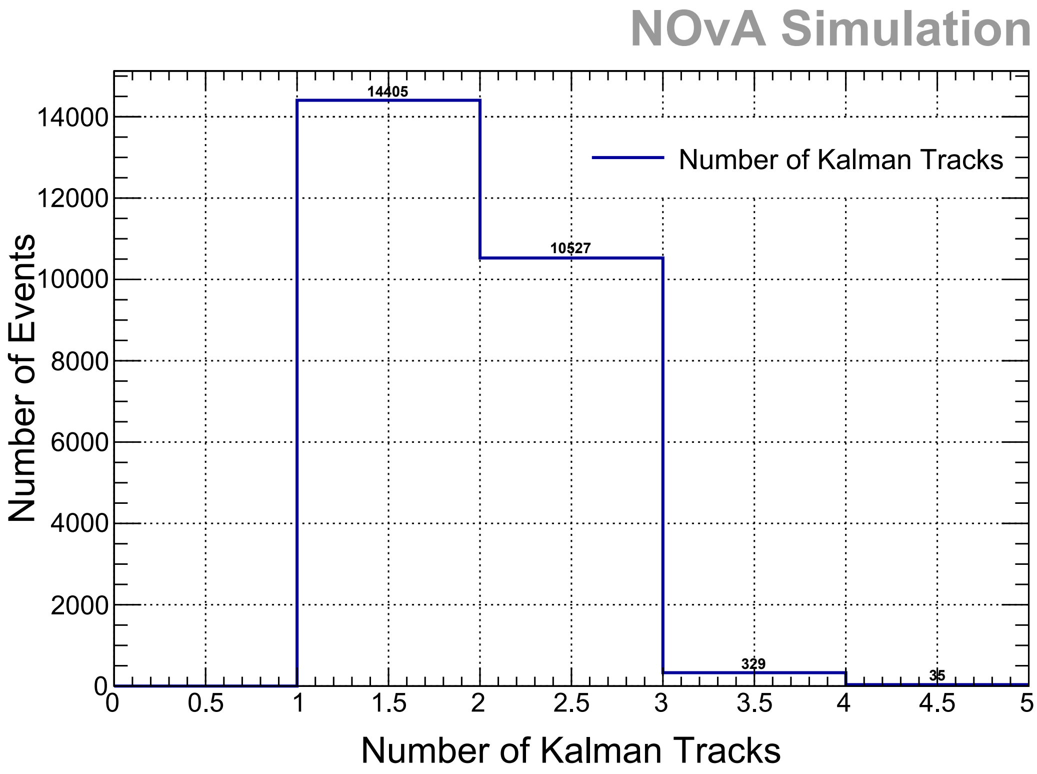

Figure 6.6 Number of Kalman tracks after Two 3D Prong cut

6.5.1 Selecting Muon Candidate Track

If the neutrino event contains only one reconstructed Kalman track; then that Kalman track will be selected as the muon candidate (as shown in Figure 6.6) and the muon candidate prong will be the reconstructed prong that most overlaps (the opening angle between the track and the prong minimized) with the muon candidate Kalman track. In all the other cases, the muon-candidate Kalman track will be selected on the basis of the most overlapped Kalman track with the muon-candidate prong. In this case, the muon candidate prong was selected based on length ($>$ 500cm) with the highest muonID score (CVN single particle trained prong). This method increases the number of correct choices from 88.1% to 96.8% (as described in table 6.7)

Figure 6.7 Muon Candidate table after prongs to track mapping

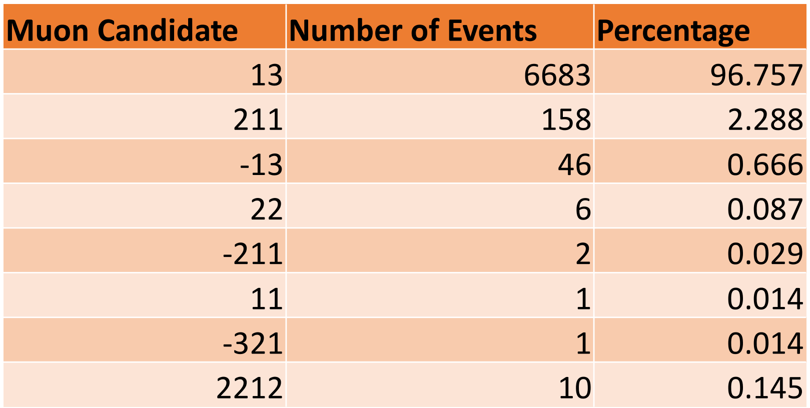

Muon Candidate	Number of Events	Percentage
13	6683	96.757
211	158	2.288
-13	46	0.666
22	6	0.087
-211	2	0.029
11	1	0.014
-321	1	0.014
2212	10	0.145

6.5.2 MuonID Cut

An optimization is performed by calculating the figure of merit: sensitivity as a function of the MuonID cut value of the Muon candidate Kalman track, where events with MuonID evaluations less than the value found on the x axis are removed. In this case, the signal is the sample that contains true muons in Muon candidate Kalman track, and the background sample contains muon candidates that are not true muons (see Figure 6.8). There is a maximum at MuonID = 0.4 and therefore we require selected events to have MuonID greater than 0.4 (as shown in Figure 6.9).

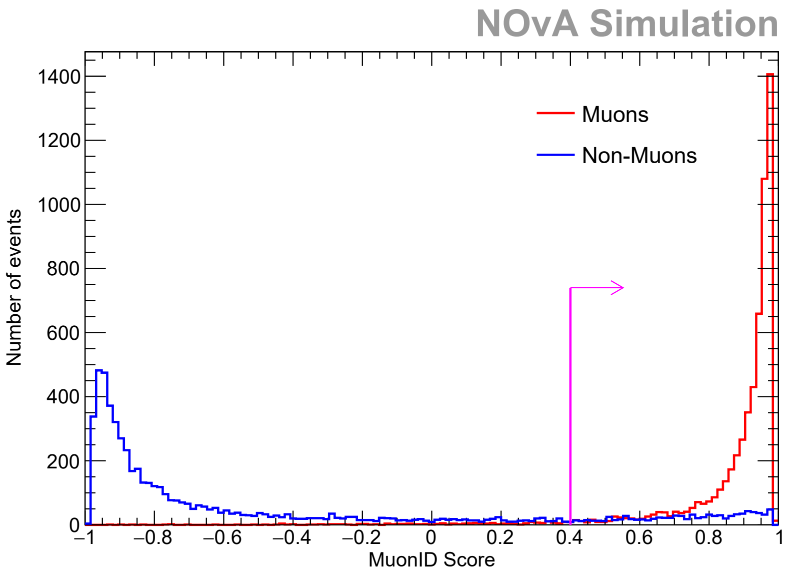

Figure 6.8 Plots of MuonID made for signal and background muon candidate Kalman tracks

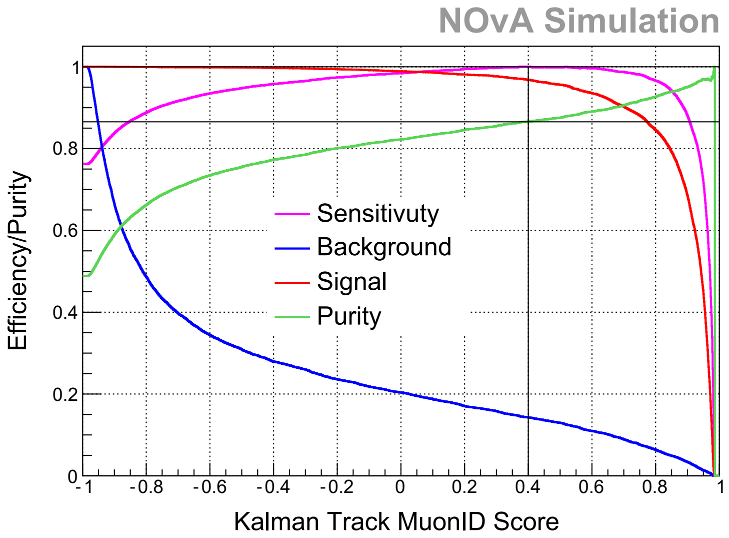

Figure 6.9 The MuonID cut value optimized by FOM as a function of MuonID Score

6.5.3 MUON ENERGY

The same muon energy estimator that was used for the ν_μ charged current inclusive analysis [77] is employed without any lower limit on the kinetic energy of the true muon. The reconstruction efficiency of the muons as a function of the true kinetic energy of the muons is shown in Figure 6.10 in the background true muon kinetic energy spectrum.

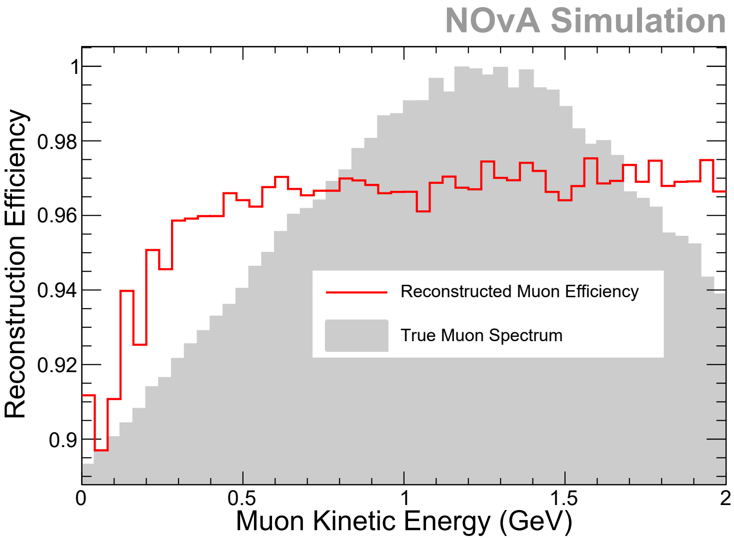

Figure 6.10 Muon Reconstruction Efficiency as a function of Muon Kinetic Energy

$$Fractional\ Resolution = \frac{(E_{Reco.} - E_{True})}{E_{True}} \tag{6.5}$$

According to the Gaussian fit created to the fractional resolution (as explained in equation 6.5), the mean value is -3×10^{-6} and the standard deviation is 3.5×10^{-2} (the fractional resolution plot is shown in Figure 6.11). To compensate for the offset of the fractional energy resolution, a constant correction factor: 1.0008 was calculated.

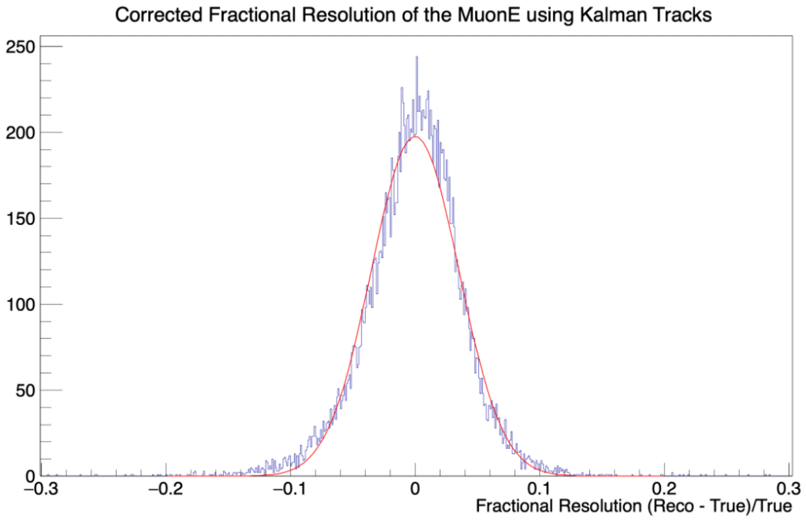

Figure 6.11 Fractional Resolution of the Muon Energy estimator

6.5.4 PION ENERGY

A multi-variate regression was trained to estimate the pion energy by using the calorimetric energy of the pion prong and the angle between the direction of the average beam and the pion prong.

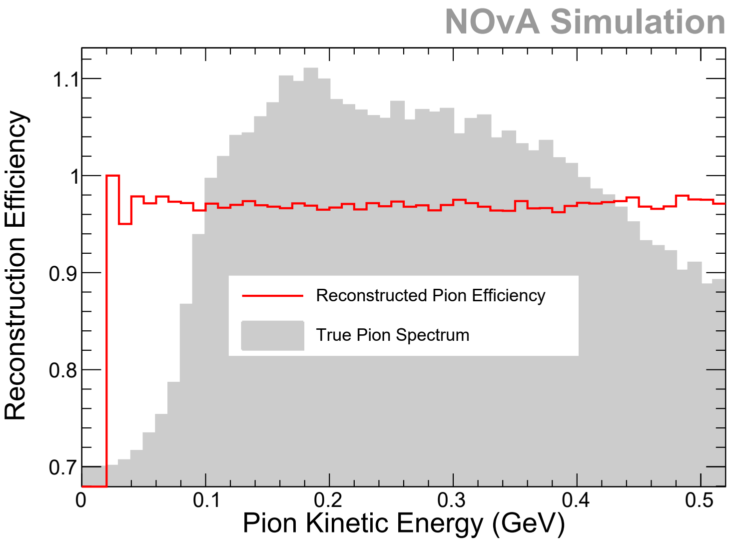

Figure 6.12 Pion Reconstruction Efficiency as a function of Pion Kinetic Energy

Previously, different types of inputs were used to train pion energy estimators. On the basis of the studies, the best pion energy resolution was obtained by using the pion calorimetric energy and the angle between the pion prong and the average beam direction. Currently, there is no lower threshold applied to the true pion Kinetic Energy. The efficiency of re-construction of the pions as a function of the true kinetic energy of the pion is shown in Figure 6.12. The mean value is 1×10^{-5} and the standard deviation is 1.53×10^{-1} (the fractional resolution plot is shown in Figure 6.13). To offset the fractional energy resolution to zero, a constant correction factor: 0.963 was calculated.

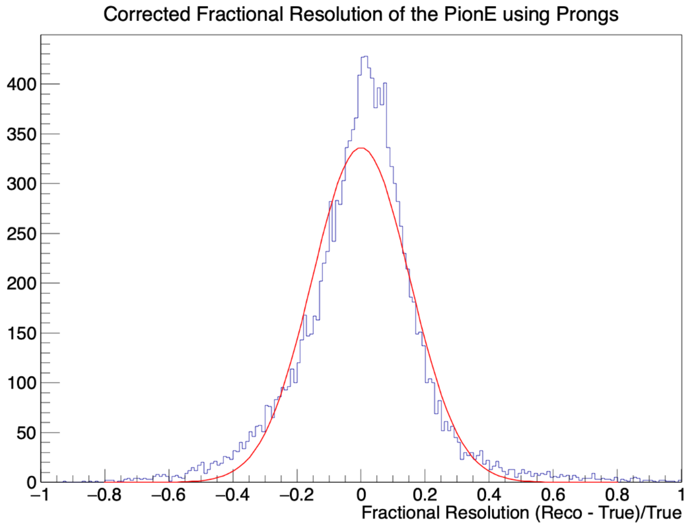

Figure 6.13 Fractional Resolution of the Pion Energy estimator

6.6 Reconstruction of Momenta

After selecting the correct muon candidate (already explained in section 6.5.1) it is important to reconstruct the kinematic properties of the muon and pion accurately to measure the reconstructed $|t|$. We rely on NOvA's track and prong reconstruction algorithms and apply corrections to further reduce the reconstruction bias on energy resolution. The track selected to represent the muon of a selected event is chosen as described in Section 6.5.1. The resulting fraction of correct choices is 96.8%.

The magnitude of the particle momentum $|P_i|$ (here $i = \mu, \pi$) is calculated using estimated particle energy E_i using following equation:

$$E_i = \sqrt{P_i^2 + m_i^2} \tag{6.6}$$

Here, m_i is the mass of the particle.
The direction of the particle is calculated by taking the unit vector (since the direction of the reconstructed track is known and the length of the reconstructed track is known it is possible to calculate the unit vector) of the particle candidate track ($\hat{u_i}$). Therefore,

$$\overrightarrow{P_i} = |P_i|\hat{u_i} \tag{6.7}$$

6.7 Selection of Signal Events

After applying preselection, the next step is to apply the main selection criteria to further separate charged current coherent events from backgrounds. The event selection consists of mainly three cuts:

- Pion ID cut: optimized to mainly remove protons present in Pion candidate prong.
- Hit ID cut: optimized to remove backgrounds that create higher hadronic activity around the reconstructed vertex.
- Kinematic ID cut: optimized to further remove coherent-like background events by investigating kinematics.

6.7.1 Pion Identification

After selecting the muon candidate prong, the next challenge is to remove events containing particles other than pions in the pion candidate prong. Studies reveal that the dominant background present in the candidate prong for the pion is protons. These protons come from backgrounds such as CCQE (Figure 6.14) and CCDIS. A deep neural network is trained using the following calculations of the pion candidate prong as input:

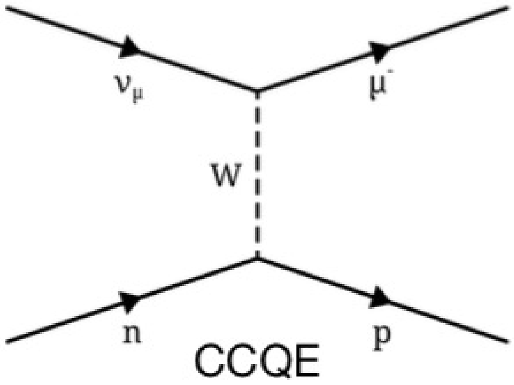

Figure 6.14 Feynman diagram of charged current quasi-elastic scattering that produces muon and proton in final state

- Minimum Hit Energy
- Maximum Hit Energy
- Average Hit Energy
- PionID-old (single particle trained prong CVN)
- MuonID (single particle trained prong CVN)

This training was done by applying Data Quality, Fiducial, Two Prong, Containment, and MuonID cuts (only pre-selection). Figure 6.15 demonstrates the correlation matrices made by taking input variables for both the signal (true pions) and the background (true protons) samples.

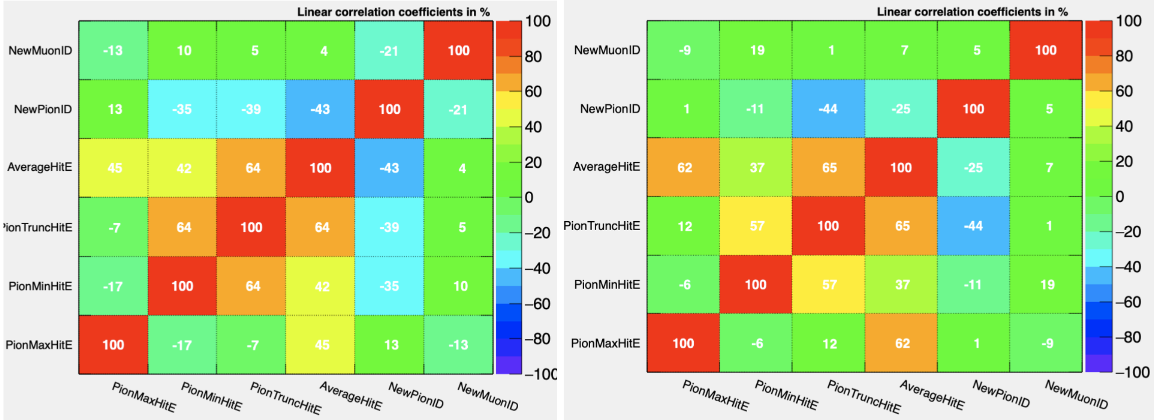

	PionMaxHitE	PionMinHitE	PionTruncHitE	AverageHitE	NewPionID	NewMuonID
NewMuonID	-13	10	5	4	-21	100
NewPionID	13	-35	-39	-43	100	-21
AverageHitE	45	42	64	100	-43	4
ionTruncHitE	-7	64	100	64	-39	5
PionMinHitE	-17	100	64	42	-35	10
PionMaxHitE	100	-17	-7	45	13	-13

	PionMaxHitE	PionMinHitE	PionTruncHitE	AverageHitE	NewPionID	NewMuonID
NewMuonID	-9	19	1	7	5	100
NewPionID	1	-11	-44	-25	100	5
AverageHitE	62	37	65	100	-25	7
PionTruncHitE	12	57	100	65	-44	1
PionMinHitE	-6	100	57	37	-11	19
PionMaxHitE	100	-6	12	62	1	-9

Figure 6.15 Mixing matrices made by analyzing input variables for True Pions (on left) and the dominating background: true protons (on right)

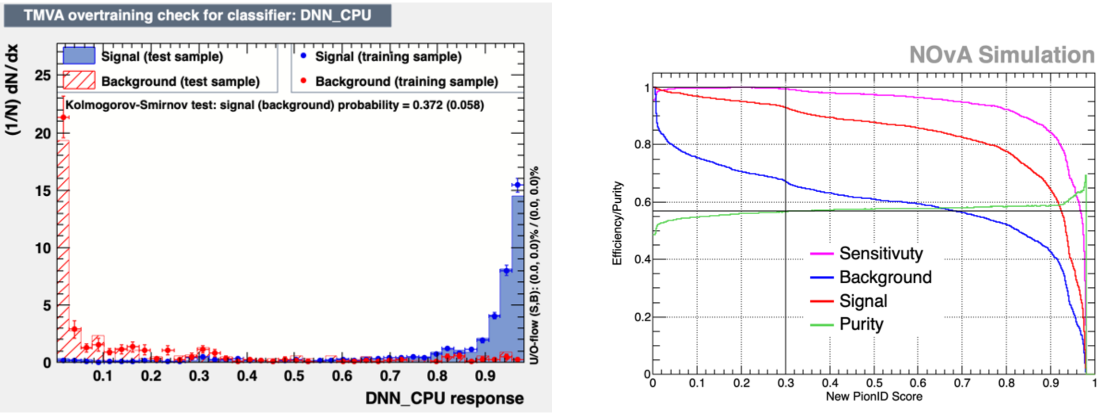

(a) PionID Score Testing Vs Training

(b) PionID Figure of Merit Plot

Figure 6.16 Creating a cut based on PionID

PionID is trained to separate pions from nonpion particles of candidate pions, such as protons. Signal events are selected using an optimized cut on PionID using the sensitivity FOM as a function of the PionID score. The FOM is maximized iteratively considering the PionID cut as the final cut and the finalized optimum cut value is PionID = 0.3 and therefore we require that the selected events have PionID greater than 0.3 (as shown in Figure 6.16).

6.7.2 Hit Energy Distributions

Hit Score is trained to separate Coherent events from Coherent-like events. Figure 6.17 (a) is the Feynman diagram that represents the CCRES event. Figure 6.17 (b) is the same event simulated in the NOvA near detector.

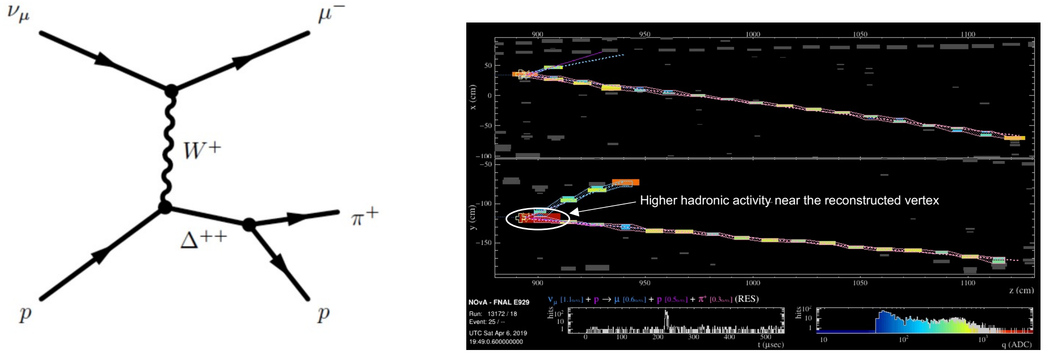

(a) Feynman diagram of CCRES event (b) CCRES event simulated in Near Detector

Figure 6.17 CC Resonant interaction simulated in NOvA Near Detector

A neural network (Multi-Layer Perceptron) is trained by using the following calculations of the Muon and Pion candidate prongs as inputs:

- First hit's energy of the muon candidate prong
- Second hit's energy of the muon candidate prong
- Third hit's energy of the muon candidate prong
- First hit's energy of the pion candidate prong
- Second hit's energy of the pion candidate prong
- Third hit's energy of the pion candidate prong
- Vertex Energy calculated by 3D-prong hits enclosed in 10cm side cube
- Vertex Energy calculated by 3D-prong hits enclosed in 20cm side cube

- Hit Ratio (Ratio between total hits in muon and pion candidate prongs to slice hits)

The mixing matrices made for input variables as shown in Figure 6.18.

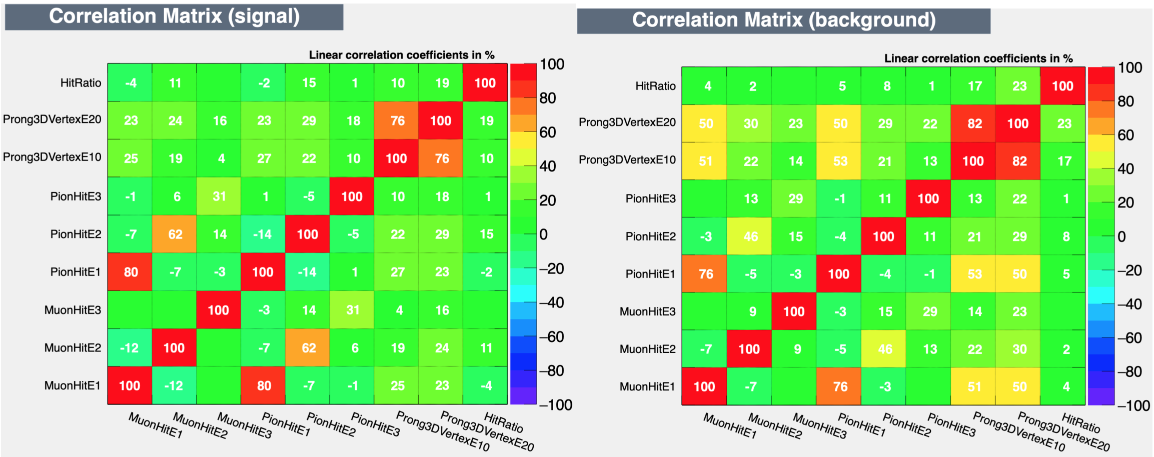

(a) Signal Matrix (b) Background Matrix

Figure 6.18 Mixing matrices made for input variables used to train HitID

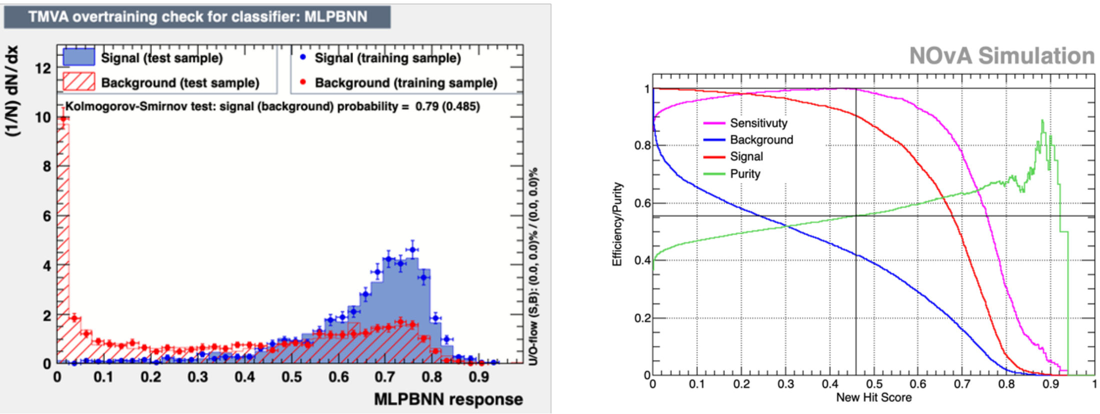

(a) Hit Score Testing Vs Training (b) Hit Score Figure of Merit Plot

Figure 6.19 Creating a cut based on Hit Score

Signal events are selected using an optimized cut on the Hit Score using the sensitivity FOM as a function of the Hit Score. The FOM is maximized in an iterative way by considering the Hit Score cut as the final cut, and the finalized optimum cut value is Hit Score = 0.46. Therefore, the selected events must have a Hit Score greater than 0.46. (as shown in Figure 6.19)

6.7.3 Event Kinematics

Even after applying the PionID cut and the HitID cut to remove background events such as CCQE and CCRES, signal events are still dominated by coherent-like background events. In order to remove such events, particle kinematics was studied. In Figure 6.20 the kinematics were calculated for both the final-state muon and pion by calculating momenta in the transverse and longitudinal directions.

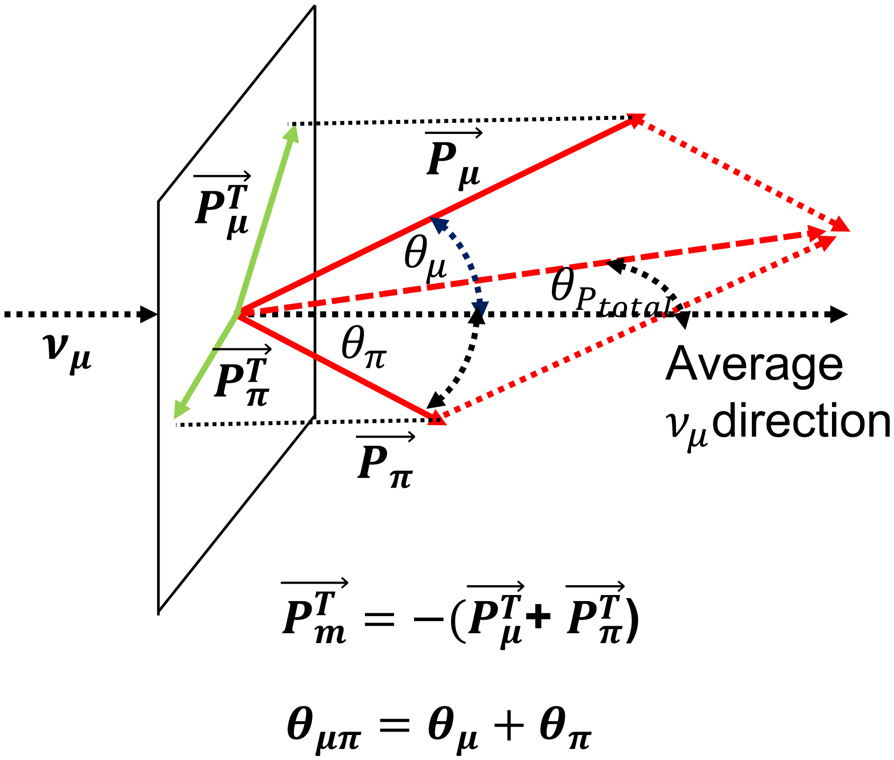

Figure 6.20 Reconstruction of the event kinematics for individual events

After estimating the energies of the muon and pion candidates, the kinematics of the muon and pion candidates can be calculated (as explained in Section 6.5.3). The kinematic score is trained to separate coherent events from background events.

A neural network (Multi-Layer Perceptron) is trained by using the following calculations of the Muon and Pion candidate prongs as inputs:

- Missing Transverse momentum $\boldsymbol{\vec{P}_m^T}$
- Muon's Transverse momentum $\boldsymbol{\vec{P}_\mu^T}$
- Pion's Transverse momentum $\boldsymbol{\vec{P}_\pi^T}$
- Opening Angle (The angle between Muon and Pion prongs $\boldsymbol{\theta_{\mu\pi}}$)
- Visible Angle (The angle between the sum of Muon and Pion momenta to the average beam direction $\boldsymbol{\theta_{P_{total}}}$)

Correlation matrices were made for the input variables by taking sample signal and background events as shown in Figure 6.21.

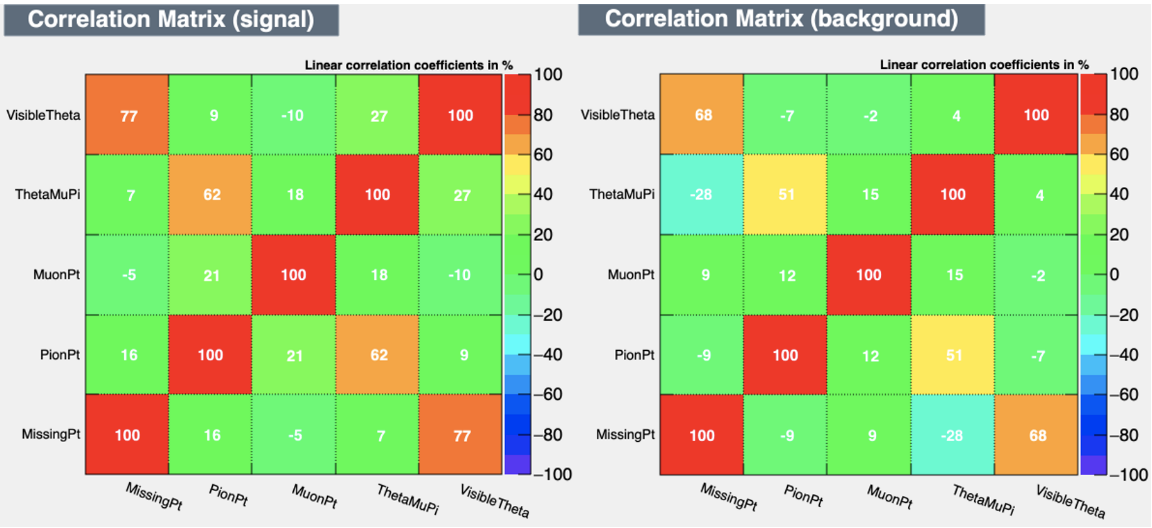
Correlation Matrix (signal)

Linear correlation coefficients in %

	MissingPt	PionPt	MuonPt	ThetaMuPi	VisibleTheta
VisibleTheta	77	9	-10	27	100
ThetaMuPi	7	62	18	100	27
MuonPt	-5	21	100	18	-10
PionPt	16	100	21	62	9
MissingPt	100	16	-5	7	77

Correlation Matrix (background)

Linear correlation coefficients in %

	MissingPt	PionPt	MuonPt	ThetaMuPi	VisibleTheta
VisibleTheta	68	-7	-2	4	100
ThetaMuPi	-28	51	15	100	4
MuonPt	9	12	100	15	-2
PionPt	-9	100	12	51	-7
MissingPt	100	-9	9	-28	68

(a) Signal Matrix

(b) Background Matrix

Figure 6.21 Mixing matrices made for input variables used to train Kinematic ID

Signal events are selected using an optimized cut on the kinetic score using the sensitivity FOM as a function of the kinetic score. The FOM is maximized in an iterative way by considering the kinematic score cut as the final cut and the finalized optimum Kinematic Score = 0.84.

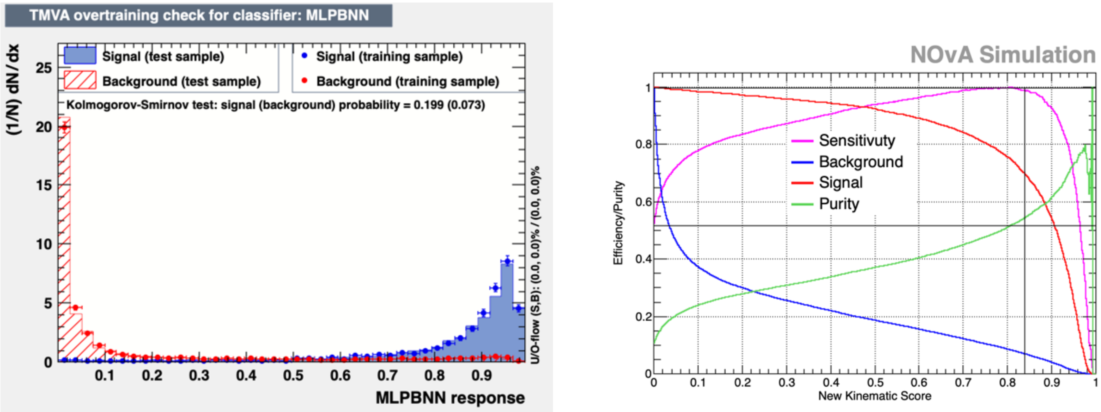

(a) Kinematic Score Testing Vs Training

(b) Kinematic Score Figure of Merit Plot

Figure 6.22 Creating a cut based on Kinematic Score

Therefore, it is necessary to select events with a Kinematic Score greater than 0.84 (as shown in Figure 6.22).

6.8 SIGNAL REGION FROM $|t|$ DISTRIBUTION

The 4-momentum transferred to the nucleus is calculated by using the following equation:

$$|t| \approx \left(\sum_{i=\mu,\pi} E_i - p_{i,L}\right)^2 + \left|\sum_{i=\mu,\pi} p_{i,T}\right|^2 \tag{6.8}$$

Here,

- E_μ is the energy of the muon
- E_π is the energy of the pion
- $p_{\mu,T}$ is the transverse momentum of the muon w.r.t. average beam direction
- $p_{\pi,T}$ is the transverse momentum of the pion w.r.t. average beam direction
- $p_{\mu,L}$ is the longitudinal momentum of the muon w.r.t. average beam direction

In Figure 6.23 represents the reconstructed $|t|$ after muonID cut (right after pre-selection). Coherent events are denoted by red color histogram, background events are in blue color, and the signal events are dominated by backgrounds.

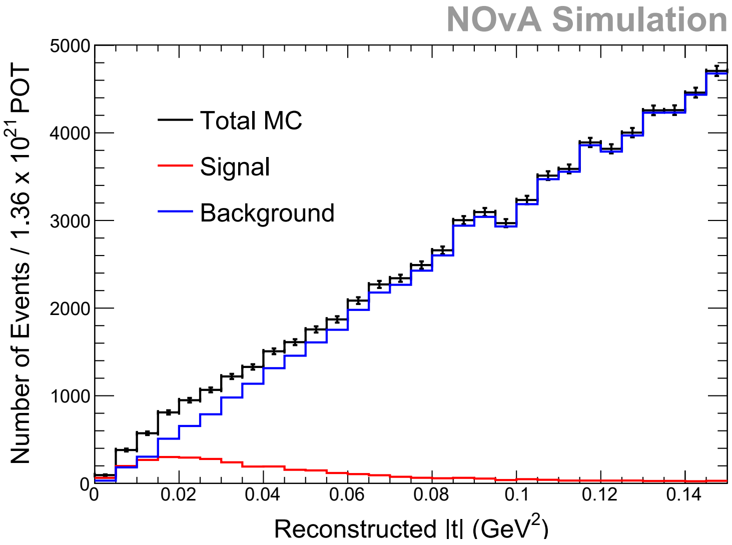

Figure 6.23 Reconstructed $|t|$ after MuonID Cut

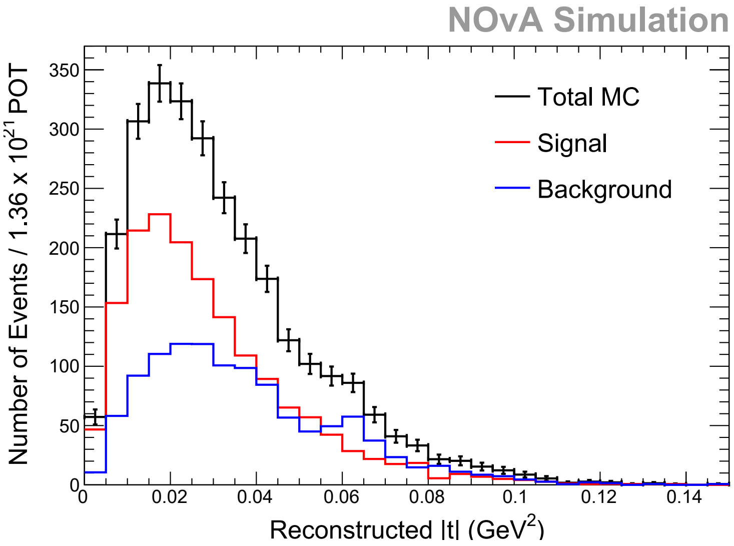

Figure 6.24 Reconstructed $|t|$ after complete event selection

In Figure 6.24 the reconstructed $|t|$ histograms are made after applying the entire event selection (Data Quality, Fiducial, Two-prong, Containment, MuonID, PionID, Hit ID, Kinematic ID cuts), and these two figures clearly demonstrate the power of our event selection.

6.9 SELECTED EVENTS

After finalizing the selection of events as mentioned above, the summarized cut table is produced as shown in Table 6.1. Absolute efficiency (that is, selected signal events / total number of true signal events) is 1.42% with purity 59%.

6.9.1 CUT TABLE WITH MC ONLY

Cut Name	CC COH	CC QE	CC RES	CC DIS	CC MEC	NC	Other	Total Bkgd	Total MC	Efficiency (%)
No Cut	112522.6	9212641.2	18716893.2	34217464.3	4782497.0	14710277.2	263914.6	81903687.4	82016209.9	97.05
Data Quality	112171.3	6474801.0	13394817.1	25566361.7	3164765.0	8224225.1	205291.6	57030261.6	57142432.8	96.74
Fiducial	110039.5	4144679.7	8407700.5	12521810.2	2149302.1	5418945.6	85330.7	32727768.6	32837808.2	94.9
Two Prong	10654.2	847830.8	300559.6	116956.3	275948.6	62522.3	8797.4	1612614.9	1623241.3	9.16
Containment	4417.7	156090.7	81372.9	18100.0	83664.5	31756.7	2864.1	373848.9	378266.6	3.81
Muon ID	3725.9	126642.8	64669.6	11222.4	70733.7	4678.6	2274.4	280221.5	283947.4	3.21
Pion ID	2792.9	24436.0	16307.8	3988.3	26934.1	1303.9	1143.5	74113.5	76906.4	2.41
Hit ID	2473.5	22726.9	5901.7	2433.8	25633.9	809.2	491.2	57996.7	60470.2	2.13
Kinematic ID	1651.2	43.5	699.5	106.8	21.7	38.3	228.9	1138.6	2789.7	1.42

Table 6.1 Cut Table made for the event selection

The composition of the "Other" backgrounds is shown in Figure 6.25. The dominant background variant in the "Other" category is due to diffractive scattering.

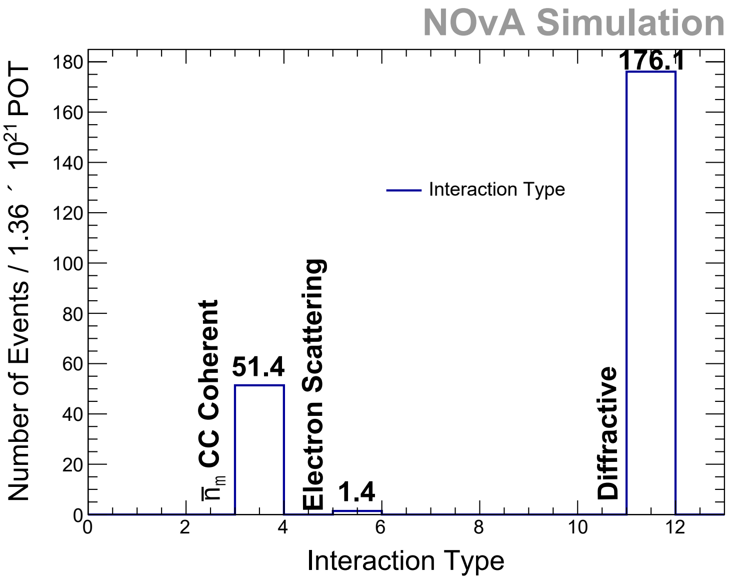

Figure 6.25 Composition of Other Backgrounds survived after event selection

Cut Name	CC COH	CC QE	CC RES	CC DIS	CC MEC	NC	Other	Total Bkgd	Total MC	Data	Data/MC
Data Quality	114839.2	6474801.0	13394817.1	25566361.7	3164765.0	8224225.1	202623.7	57027593.7	57142432.8	55469310	0.97
Fiducial	110718.8	4144679.7	8407700.5	12521810.2	2149302.1	5418945.6	84651.4	32727089.3	32837808.2	31680510	0.96
Two Prong	5664.1	846090.6	296850.4	114800.9	275315.1	61895.8	7839.5	1602792.3	1608456.4	1782981	1.11
Containment	2432.4	156027.6	80526.5	17963.4	83638.2	31443.4	2587.7	372186.8	374619.2	414796	1.11
Muon ID	2077.2	126599.3	63967.8	11121.6	70708.8	4636.6	2042.0	279076.2	281153.4	308715	1.10
Pion ID	1143.9	24392.5	15606.0	3887.4	26909.3	1261.9	911.4	72968.6	74112.4	80051	1.08
Hit ID	820.8	22220.5	5141.3	2202.1	25033.4	742.0	259.6	55598.9	56419.7	59982	1.06

Table 6.2 Cut Table by removing signal box (Data Quality and Fiducial cuts contain signal box)

6.9.2 Cut Table with Data and MC without Signal Box

After granting permission to analyze neutrino events of the data sample essential steps are taken to investigate DataMC variations. Since permission to examine neutrino events of the data sample has not yet been granted, to investigate Data/MC variations in main event selection cuts, the signal box was removed by applying a check: $!(PionID > 0.3 \;\&\&\; HitID > 0.46 \;\&\&\; KinematicID > 0.84)$. After removing the events that qualify in the signal box, the cut table was made to check the DataMC ratio as shown in Table 6.2.

6.9.3 Distribution of reconstructed topologies

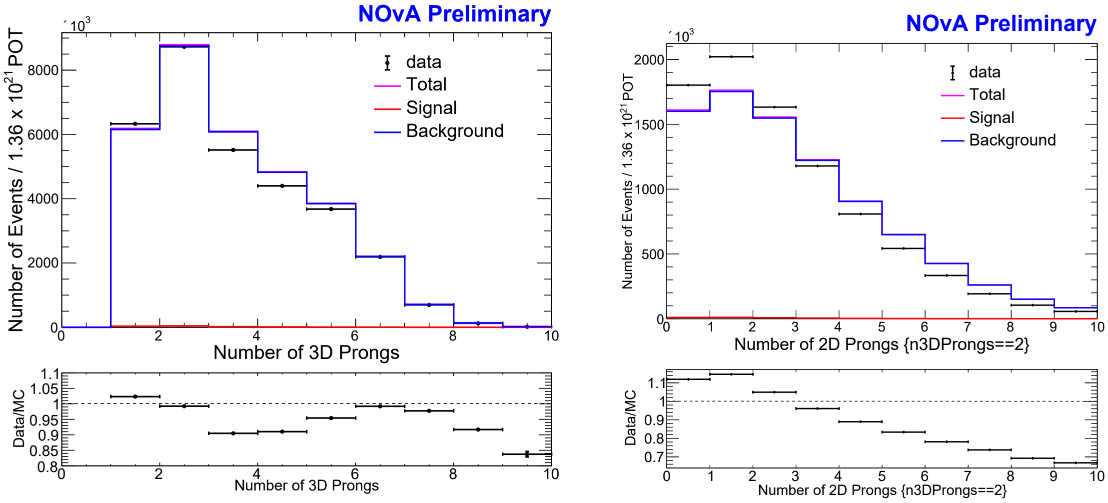

(a) Number of 3D Prongs

(b) Number of 2D Prongs with 2-3D Prongs

Figure 6.26 Number of reconstructed prongs Data Vs Total MC

Studying the Data/Total MC ratio calculated in Table 6.2 revealed that there is a discrepancy of 11% in Data/MC at Two 3D prong cut. In order to understand where the discrepancy comes from, the number of 3D prongs and the number of 2D prongs were studied. In Figure 6.26 (a) the number of 3D prongs was compared between the data and Monte Carlo. Our cut value for 3D prongs is 2 and there is no significant discrepancy between data and Monte Carlo at 2. Further investigations were done with the number of 2D prongs with the selection of 2-3D prongs. A significant data/total Monte Carlo discrepancy was observed in our choice at 0-2D prongs, as shown in Figure 6.26.

Cut Name	**Data Efficiency (%)**	**Total MC Efficiency (%)**	**Efficiency Ratio (Data/Total MC)**
2-3D Prong Cut	27.54695	26.77438	1.02885
2-3D & 0-2D Png Cut	20.6569	18.46245	1.11886
Combined	5.6903	4.9432	1.15114

Table 6.3 Two 3D Prong Cut Efficiency Ratio

To apply a data-driven correction at 2-3D prong cut, we first calculated efficiencies for neutrino events from both data and Monte Carlo, then the efficiency data/total MC ratio was calculated as shown in Table 6.3. The correction factor 1.15114 will be applied in Section 7.1.1.

Chapter 7

Background Determination and Cross-Section Measurements

So far, the numbers mentioned in the cut table 6.1 are determined by MC statistics. In reality, the numbers might be different for both the signal and the background events. Therefore, it is necessary to define control samples to check whether the numbers are accurate.

7.1 Background Control Samples

The analysis is mainly based on three cuts:

1. PionID Cut
2. HitScore Cut
3. Kinematic Cut

Therefore, 3 discriminants can be made using PionID Score, Hit Score, and Kinematic Score and the idea is to control the shape specifically around the cut region for each of the 3 discriminants by using the events which fail any of the other 2 cuts. Looking at the same samples in the data, we can compare the shapes in which the signal distributions are negligible.

After inverting the Hit ID cut (i.e. HitID < 0.46) and Kinematic ID cut (i.e. Kinematic ID < 0.84) Pion ID score was graphed for Data, Total MC, Signal and Background events.

The efficiencies were calculated for the events from data and total MC samples at the cut value: 0.3.

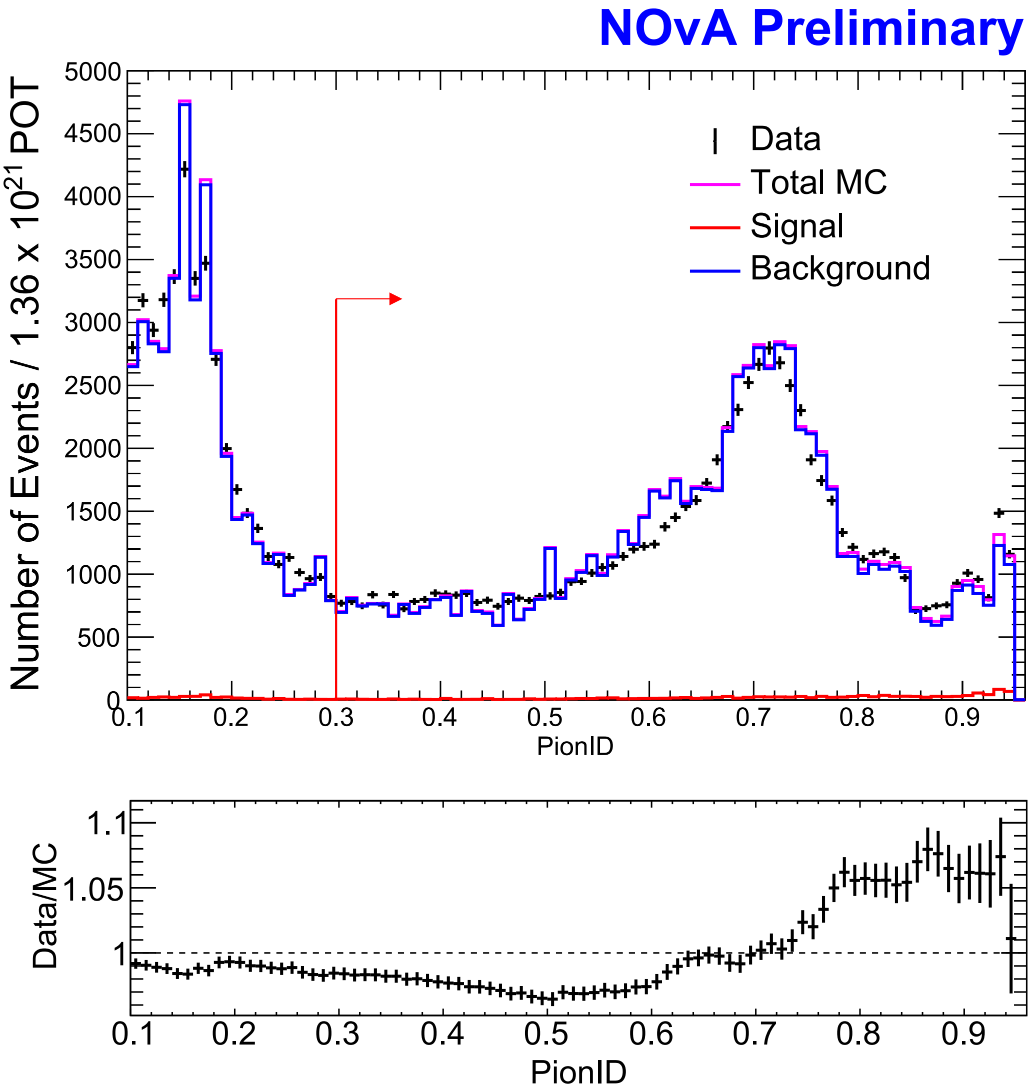

Figure 7.1 Plot of PionID Score made with events that failed either Kinematic Score or Hit Score cuts (Kinematic Score < 0.84 or Hit Score < 0.46)

The cumulative ratio of the data to the total MC is plotted in Figure 7.1. Similarly, the HitID score was graphed for data, total MC, signal and background events by inverting the PionID cut (i.e. Pion ID < 0.3) and Kinematic ID cut (i.e. Kinematic ID < 0.84).

The cumulative ratio of the data to the total MC was then plotted in Figure 7.2.

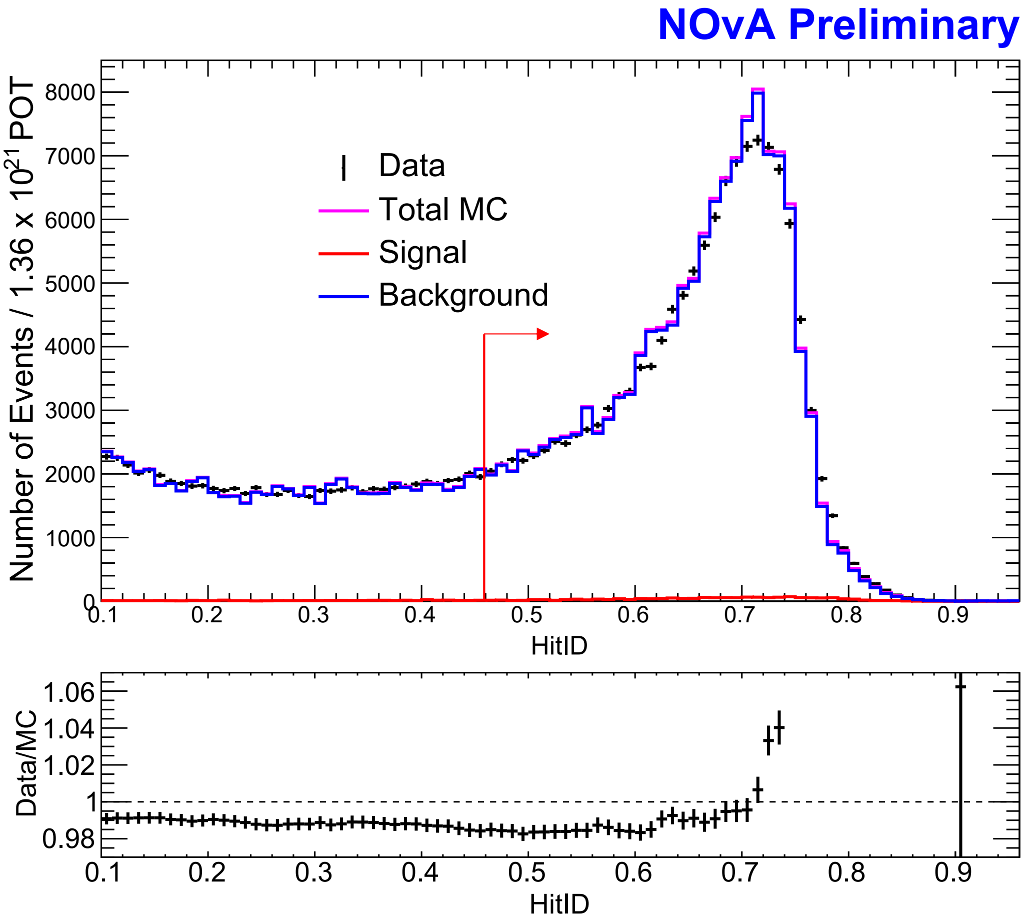

Figure 7.2 Plot of Hit Score made with events that failed either Kinematic Score or PionID Score cuts (Kinematic Score < 0.84 or PionID Score < 0.3)

The efficiencies were calculated for the events from data and total MC samples at the cut value: 0.46. Finally, the Kinematic ID score was plotted for the data, total MC, signal and background events by setting the Pion ID < 0.05 and Hit ID < 0.05. The cumulative ratio of the data to the total MC was then plotted in Figure 7.3. The efficiencies were calculated for the events from the data and total MC samples at the cut value: 0.84.

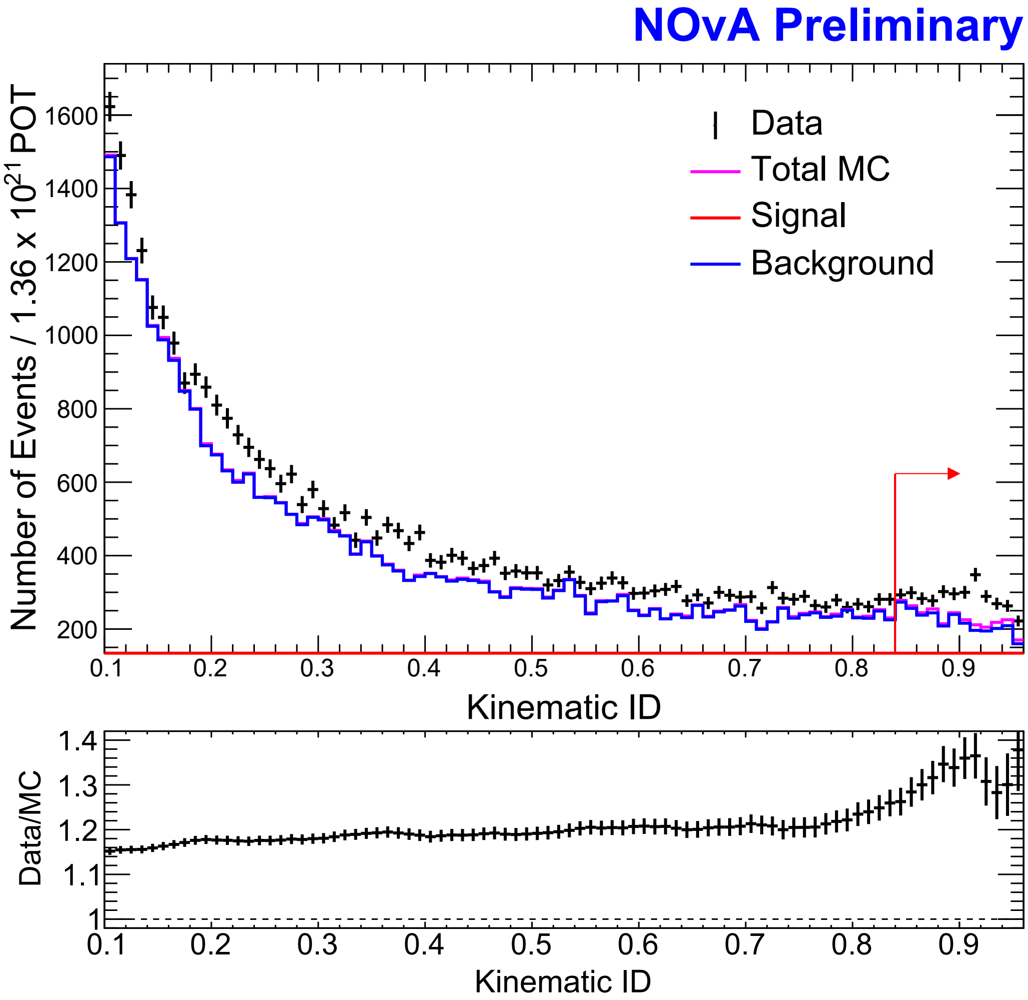

Figure 7.3 Plot of Kinematic Score made with events that failed either PionID Score or Hit Score cuts (PionID Score < 0.05 or Hit Score < 0.05)

Table 7.1 Efficiency ratios calculated to correct main cuts

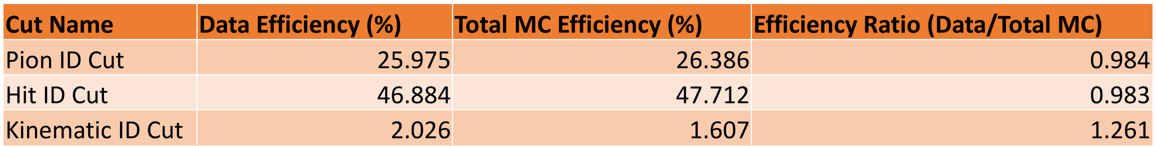

Cut Name	Data Efficiency (%)	Total MC Efficiency (%)	Efficiency Ratio (Data/Total MC)
Pion ID Cut	25.975	26.386	0.984
Hit ID Cut	46.884	47.712	0.983
Kinematic ID Cut	2.026	1.607	1.261

The calculated efficiency ratios (Data/Total MC) at each cut level can be found in Table 7.1.

7.1.1 Cut Table with Data Normalized to Two Prong Cut

The data-driven correction factors calculated in Table 7.1 were applied to the cut table 6.2 and normalized all background columns with respect to the two-prong cut. The final cut table was made by removing the signal box and is shown in Table 7.2.

Table 7.2 Cut Table made for the event selection normalized to Two Prong cut and data-driven corrections applied (Data Quality and Fiducial cuts contain signal box)

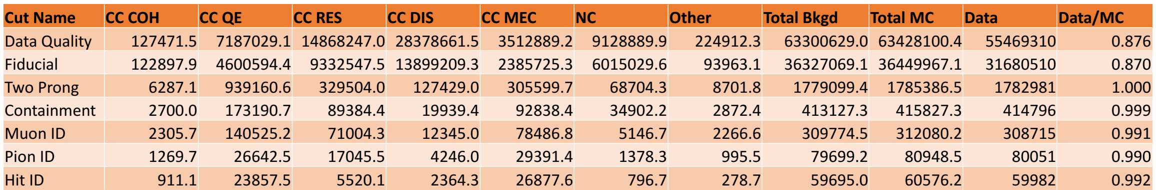

Cut Name	**CC COH**	**CC QE**	**CC RES**	**CC DIS**	**CC MEC**	**NC**	**Other**	**Total Bkgd**	**Total MC**	**Data**	**Data/MC**
Data Quality	127471.5	7187029.1	14868247.0	28378661.5	3512889.2	9128889.9	224912.3	63300629.0	63428100.4	55469310	0.876
Fiducial	122897.9	4600594.4	9332547.5	13899209.3	2385725.3	6015029.6	93963.1	36327069.1	36449967.1	31680510	0.870
Two Prong	6287.1	939160.6	329504.0	127429.0	305599.7	68704.3	8701.8	1779099.4	1785386.5	1782981	1.000
Containment	2700.0	173190.7	89384.4	19939.4	92838.4	34902.2	2872.4	413127.3	415827.3	414796	0.999
Muon ID	2305.7	140525.2	71004.3	12345.0	78486.8	5146.7	2266.6	309774.5	312080.2	308715	0.991
Pion ID	1269.7	26642.5	17045.5	4246.0	29391.4	1378.3	995.5	79699.2	80948.5	80051	0.990
Hit ID	911.1	23857.5	5520.1	2364.3	26877.6	796.7	278.7	59695.0	60576.2	59982	0.992

7.1.2 Background Determination from Data

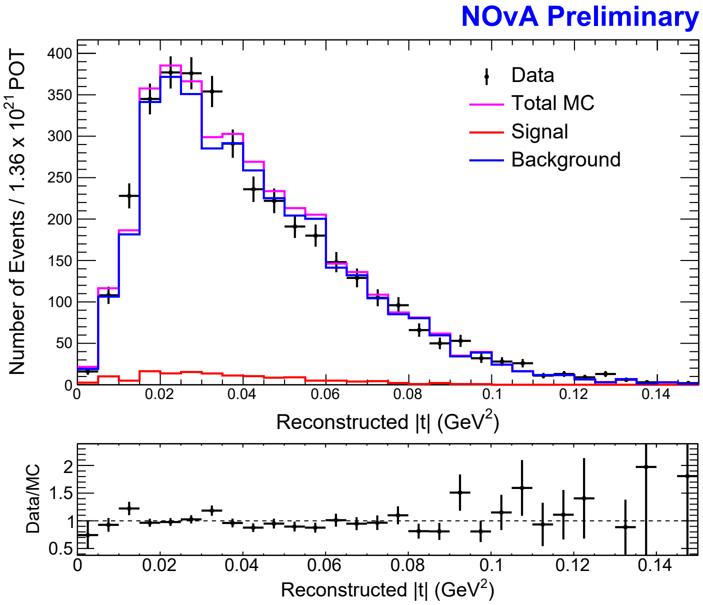

Figure 7.4 Plot of $|t|$ distributions made with failed events (PionID Score < 0.05 or Hit Score < 0.05) and (Kinematic Score > 0.84). An absolute normalization to the expected pot is used for the MC, corrected by the factors from table 7.1

We have already defined a region where the signal is not visible. The signature of the charged current-coherent events is to have a small $|t|$ distribution. We will look at the $|t|$ distribution of the data in the background region. Here, all Monte Carlo histograms are normalized to the nominal POT. The Total Background histogram was scaled using the product of 1.261 (efficiency ratio calculated for the Kinematic ID cut in table 7.1) and 1.11 (data / MC ratio calculated at the two-prong cut in table 6.2). The total Monte Carlo histogram was created by adding signal and background histograms. The integral of the Data histogram is 3736.0 and the integral of the Total MC histogram is 3758.95. Therefore, the Data/MC ratio is 0.994. After applying data-driven corrections we can control the Data/Total MC ratio as a function of cuts to about 1%!

The next step is to create a data-based background prediction in the signal region. In order to create prediction in the signal region, the following $|t|$ ratio was calculated bin by bin with propagation errors defined as follows:

$$\frac{Background\ |t|\ in\ control\ region}{Background\ |t|\ in\ signal\ region} \tag{7.1}$$

In this case, "background $|t|$ in the background control region" was taken from Figure 7.4 and the "background $|t|$ in the signal region" was taken from Figure 6.24. The motivation to calculate the $|t|$ ratio in this way is due to the fact that there are higher statistics in the background control region compared to the signal region, so the prediction calculation will be relatively accurate. Another reason is that the $|t|$ ratio as shown in Figure 7.5 will be very robust with the presence of extreme variations applied to our simulation model. In order to check the robustness of the reconstructed $|t|$ ratio, extreme variations were applied to the GENIE knobs available for the dominant background (i.e. CCRES).

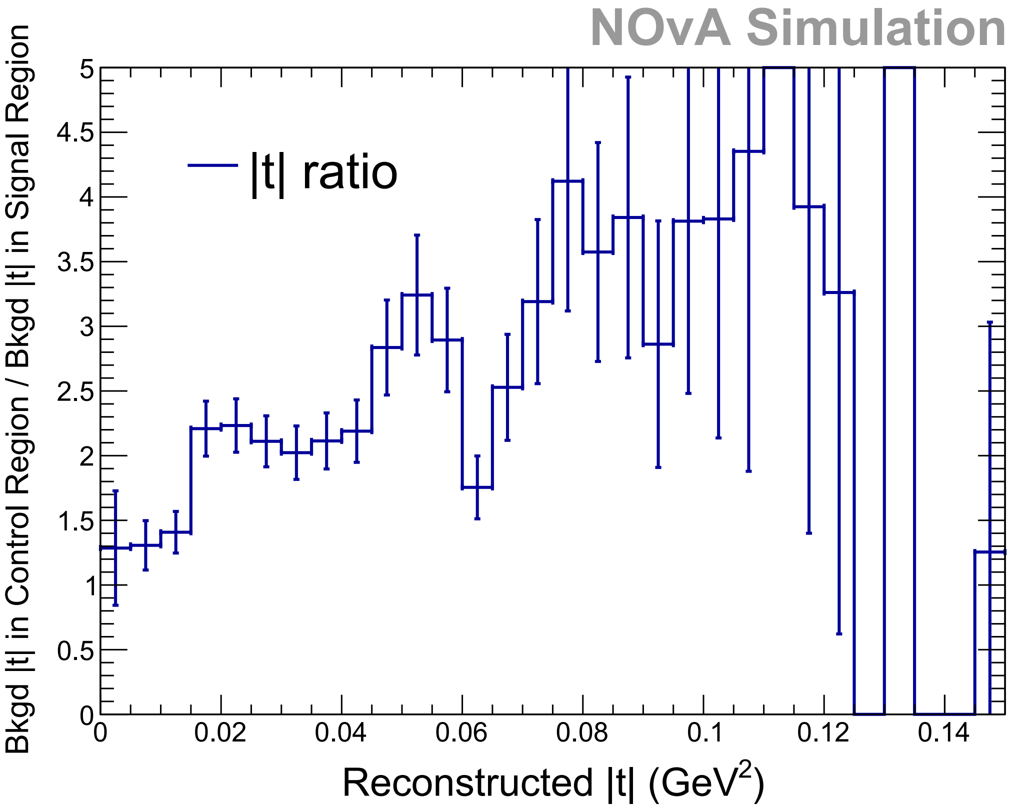

Figure 7.5 Plot of $|t|$ ratio made with failed events (PionID Score < 0.05 or Hit Score < 0.05) and (Kinematic Score > 0.84).

7.1.3 TESTS APPLIED FOR $|t|$ RATIO

In order to demonstrate that the $|t|$ ratio is immune to extreme simulation changes, the following GENIE shifts were introduced:

- CCRESMa $\sigma = -3, -2, -1, +1, +2, +3$ (as shown in Figure 7.6)
- CCRESMv $\sigma = -3, -2, -1, +1, +2, +3$ (as shown in Figure 7.7)

Here, CCRESMa is the axial mass of the CCRES interactions and CCRESMv is the vector mass.

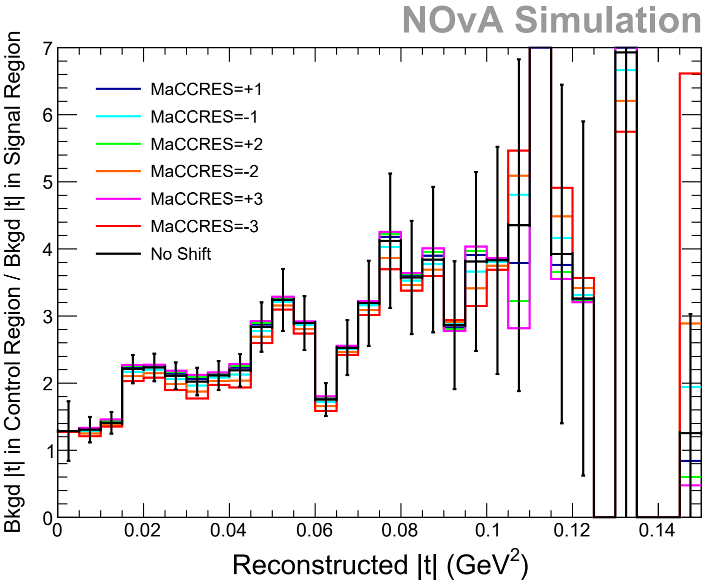

Figure 7.6 Plot of $|t|$ ratio by applying shifts for GENIE Knob: CCRESMa

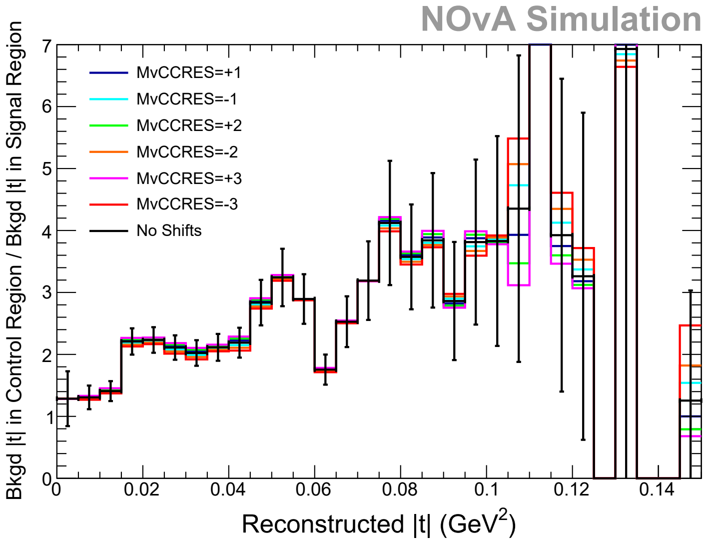

Figure 7.7 Plot of $|t|$ ratio by applying shifts for GENIE Knob: CCRESMv

In conclusion, the $|t|$ ratio is very stable with the presence of extreme changes applied to the simulation model (the shifts are within the error bars).

The reconstructed $|t|$ histograms were made for the background control region (Figure 7.8) and signal region (Figure 7.9) using background events. The dominating background in both regions is Charged-Current Resonant.

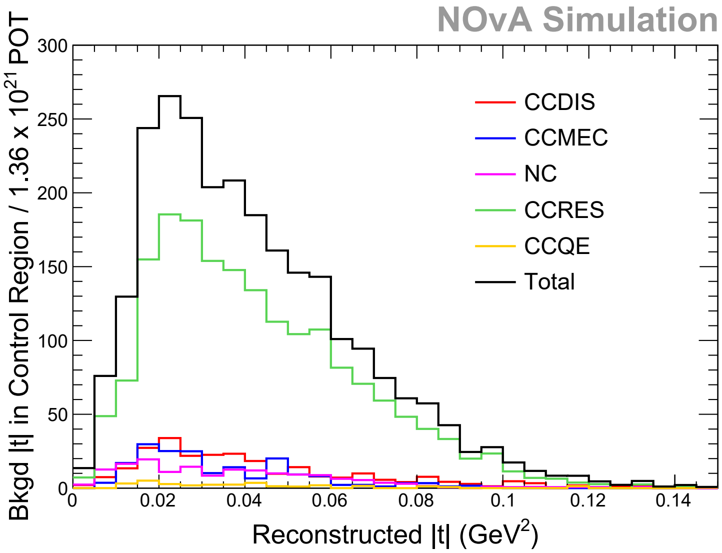

Figure 7.8 Plot of Background $|t|$ split into different interaction types in background control region

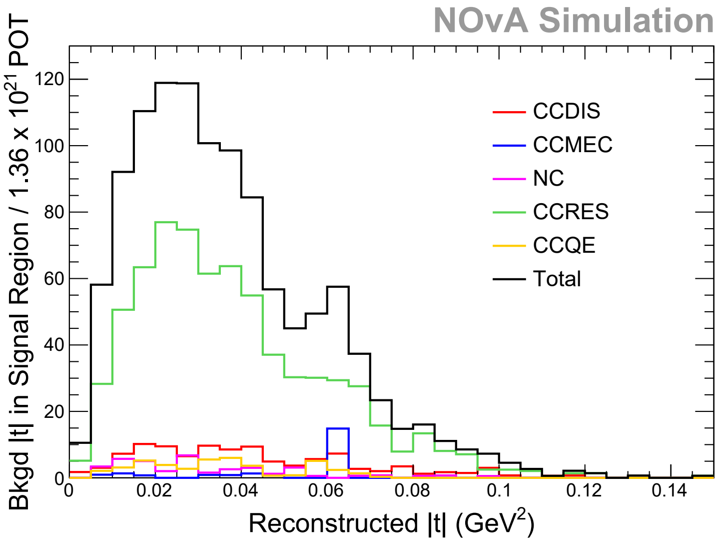

Figure 7.9 Plot of Background $|t|$ split into different interaction types in signal region

7.1.4 Background Predictions for Signal Region

In order to calculate a data-based prediction for the background $|t|$ for the bin by bin of the signal region, the $|t|$ ratio and the reconstructed $|t|$ made using data in the background region were used. The i^{th} bin of the prediction is calculated by using equation 7.2:

$$i^{th}\, bin\, of\, Data{-}based\, prediction = \frac{i^{th}\ bin\ of\ Data\ background\ |t|\ in\ control\ region}{SF_i} \tag{7.2}$$

In this case, scaling factor of i^{th} bin (SF_i) is given by the ratio histogram denoted in Figure 7.5

$$SF_i = \frac{i^{th}\ bin\ of\ Background\ |t|\ in\ control\ region}{i^{th}\ bin\ of\ Background\ |t|\ in\ signal\ region} \tag{7.3}$$

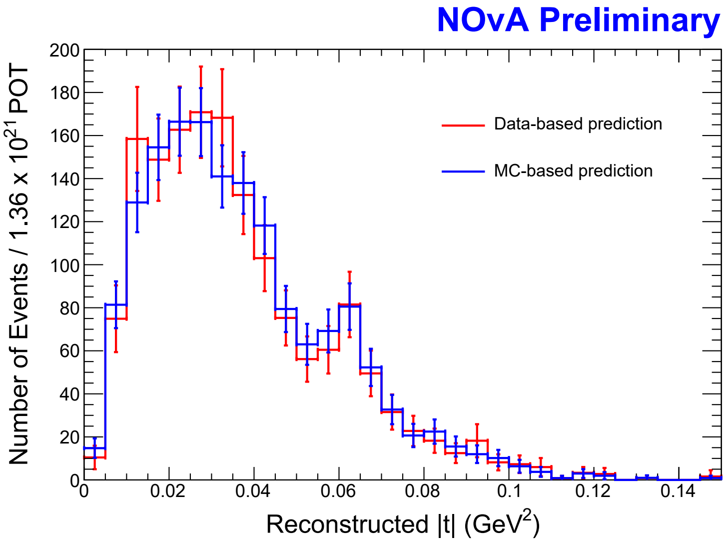

Figure 7.10 Plot of $|t|$ predictions made for signal region using data

The data-based background prediction was compared with the MC background in Figure 7.10.

After selecting data-based prediction, the predicted total reconstructed $|t|$ was calculated. Here:

$$Predicted\ Total\ |t|\ (FakeData) = Monte\ Carlo\ Signal\ +\ Data - based\ prediction \tag{7.4}$$

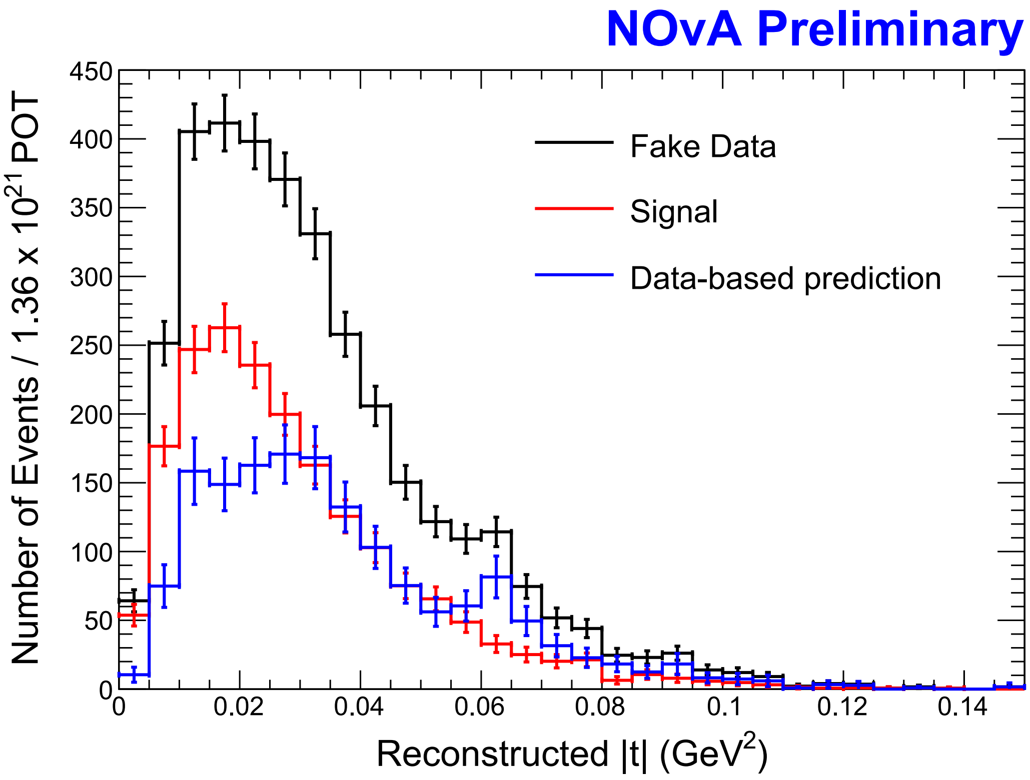

Figure 7.11 Plot of total $|t|$ Data-based prediction using Signal MC

The error of each bin of the predicted total $|t|$ is calculated by accounting for the statistical error of each bin. All histograms are normalized to data POT.
The predicted signal is calculated as follows:

$$Signal\ |t|\ Prediction = Predicted\ |t|\ from\ Fake\ Data -\ Data - based\ Background \tag{7.5}$$

Table 7.3 Integrals of the histograms with errors (signal extractions done using Figure 7.12)

	Signal	**Background**	**Total**
Data-Based Prediction	1900.9±87.7	1590.0±64.8	3490.9.3±59.1
MC-Based Prediction	1900.9±76.4	1593.8±48.4	3494.7±59.1

The integral of the data-based background prediction is 1590.0 ± 64.8 and the Monte Carlo prediction is 1593.8 ± 48.4.

In this figure, the shaded region in each bin denotes statistical uncertainty. The error bars in each bin were calculated by accounting for the propagation error. The integral of the signal prediction is 1900.9 ± 87.7 compared to the Monte Carlo-based signal prediction, 1900.9 ± 76.4.

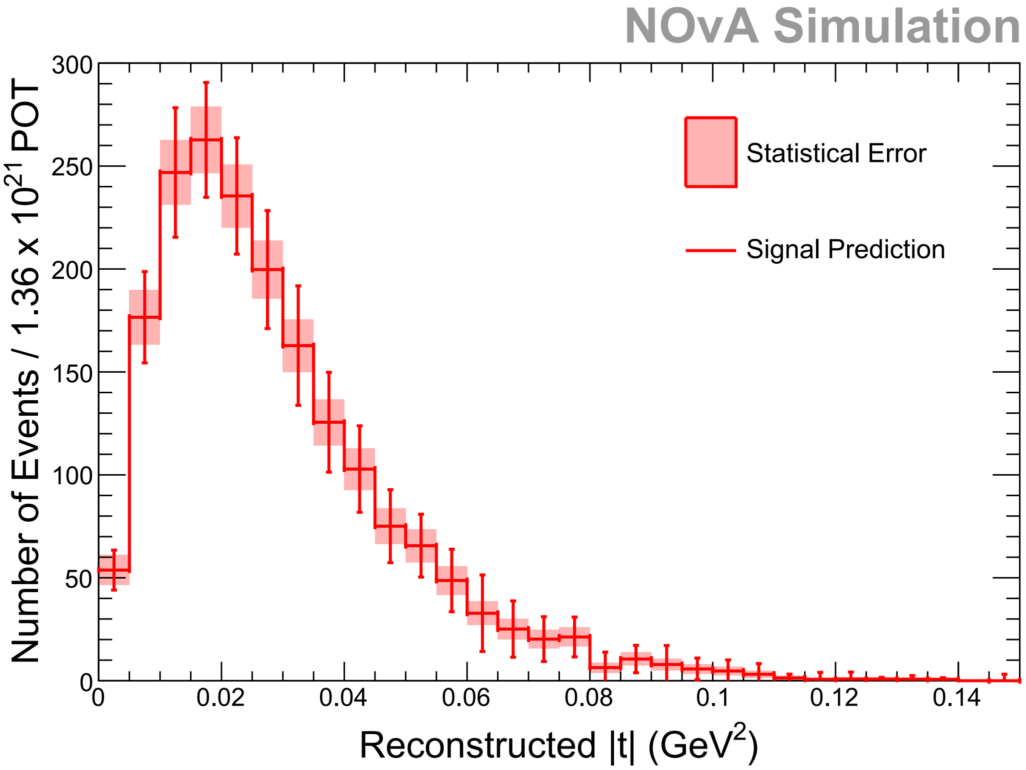

Figure 7.12 Plot of subtracted Signal $|t|$ from total $|t|$ prediction with errors

7.3 DETERMINATION OF THE FLUX AVERAGED CROSS-SECTION

The remaining unknowns to finalize the flux-averaged cross section are the diffractive corrected number of nuclei and the neutrino flux.

7.3.1 NUMBER OF TARGETS IN FIDUCIAL VOLUME

We use standard NOvA tools to calculate the number of nuclei. The only input is the fiducial volume.

Table 7.4 Target Composition

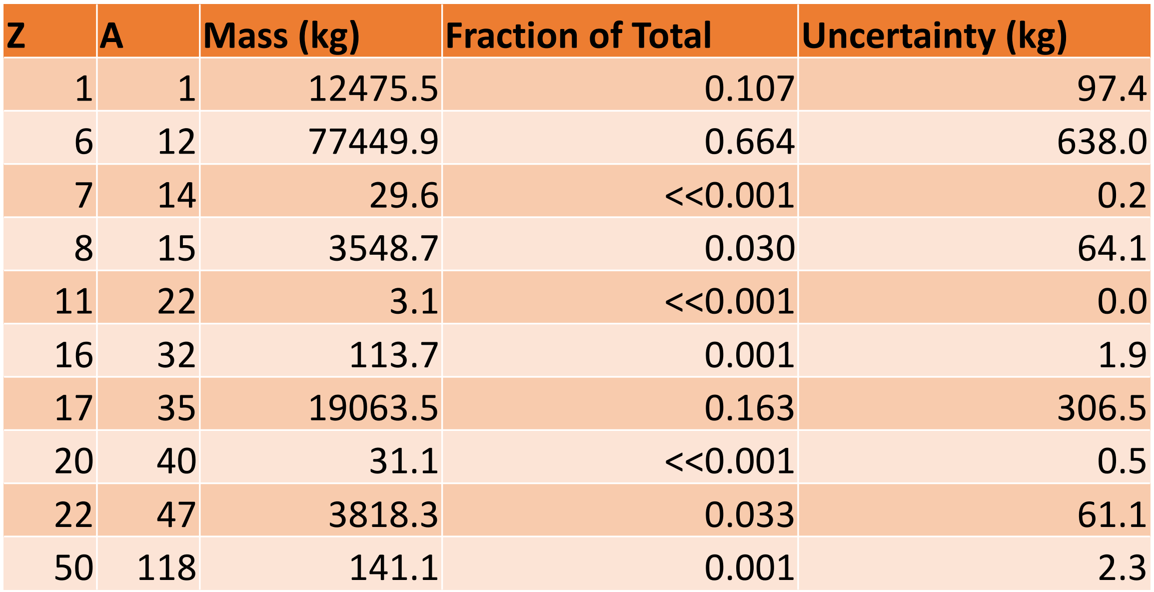

Z	A	Mass (kg)	Fraction of Total	Uncertainty (kg)
1	1	12475.5	0.107	97.4
6	12	77449.9	0.664	638.0
7	14	29.6	<<0.001	0.2
8	15	3548.7	0.030	64.1
11	22	3.1	<<0.001	0.0
16	32	113.7	0.001	1.9
17	35	19063.5	0.163	306.5
20	40	31.1	<<0.001	0.5
22	47	3818.3	0.033	61.1
50	118	141.1	0.001	2.3

$$Total\ Number\ of\ Target\ nucleons = 7.03 \times 10^{31} \tag{7.6}$$

$$Total\ Number\ of\ Target\ nuclei = 1.19 \times 10^{31} \tag{7.7}$$

$$Total\ Number\ of\ H\ nuclei = 7.51 \times 10^{30} \tag{7.8}$$

$$\therefore Diffraction\ Corrected\ Total\ Number\ of\ nuclei = 4.40 \times 10^{30} \tag{7.9}$$

$$Total\ mass\ (kg) = 116669 \pm 719.96\ (0.62\%) \tag{7.10}$$

7.3.2 Neutrino flux

We used the standard NOvA tool "DeriveFlux" function to determine the flux histogram. The input for this function is the fiducial volume.

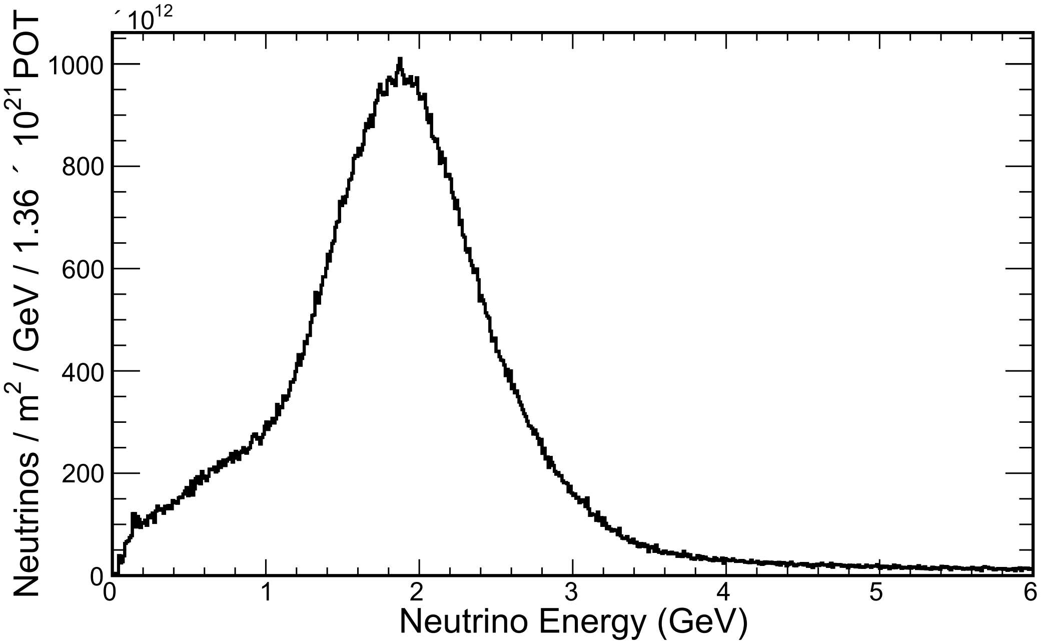

Figure 7.13 Plot of NOvA flux seen by Near Detector (Normalized to Data POT)

$$Total\ Neutrino\ Flux = 1.58 \times 10^{17} Neutrinos/m^2/GeV/1.36 \times 10^{21}\ POT \quad (7.11)$$

$$Relative\ Error\ of\ Flux = 8.3\% \quad (7.12)$$

This 8.3% flux uncertainity is [78]

7.3.3 Cross-section from observed signal events

After substituting all calculations into Equation 7.13 the flux-averaged total cross section averaged by flux was calculated.

$$\sigma = \frac{N_{Data} - N_{Bkgd}}{\varepsilon_{Coh}\ \Phi\ N_A} \quad (7.13)$$

$$\therefore \sigma = \frac{1900.9 \pm 87.7(Stat.)}{1.42 \times 10^{-2} \times 1.15114 \times 1.58 \times 10^{13} \times 4.4 \times 10^{30}} \tag{7.14}$$

$$\therefore \sigma = 1.64 \pm 0.08(stat.) \times 10^{-39} cm^2/nucleus \tag{7.15}$$

The effective mass <A> was calculated by using Table 7.4:

$$\langle A \rangle = 15.9 \tag{7.16}$$

$$\sigma_{scaled} = (15.9/12)^{2/3} \times (1.64 \times 10^{-39}) \tag{7.17}$$

$$\therefore \sigma_{scaled} = 1.98 \times 10^{-39} cm^2/C12 \tag{7.18}$$

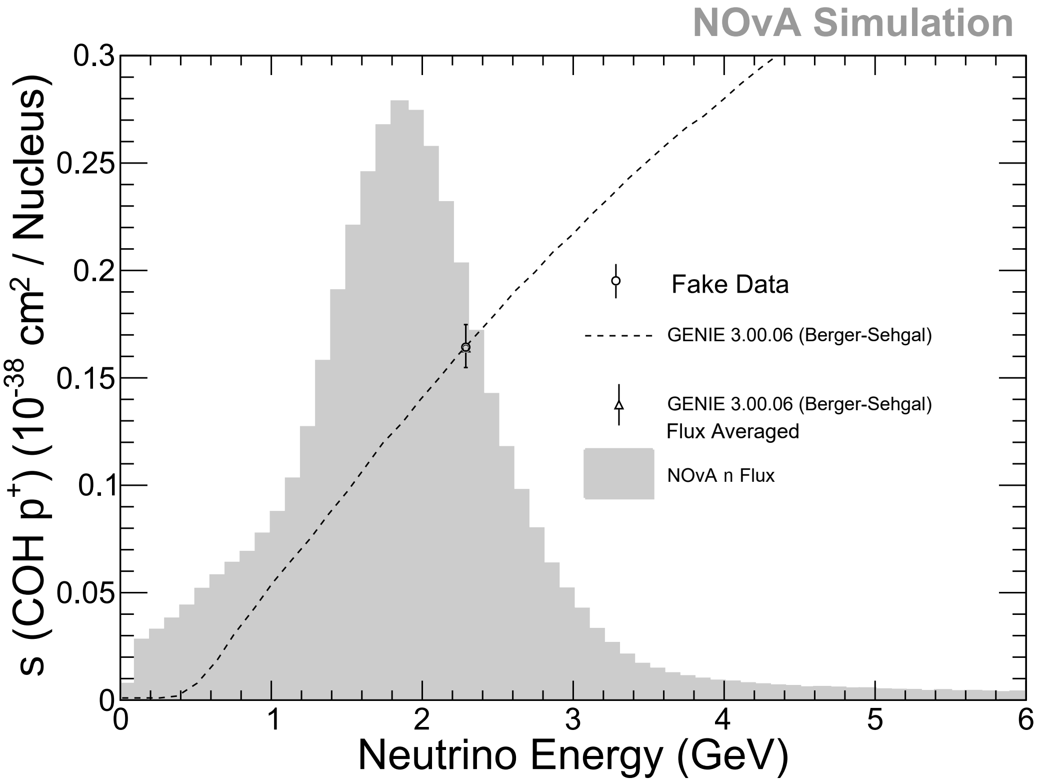

Figure 7.14 Plot of total cross-section as a function of Neutrino Energy

Chapter 8

Systematic Uncertainties

8.1 Systematic uncertainties on the measured cross-section

The analysis evaluates systematic uncertainties by utilizing simulation samples that have been systematically altered, when possible, and by re-weighting events in other situations. For each systematic effect, the cross-section is recalculated entirely, which includes reestimating the background, unfolding, correcting for efficiency, and normalizing the flux. The analysis addresses various sources of systematic uncertainties, which will be explained in the following discussion. We assessed systematics for both the signal event samples (pure sample of charged current coherent events) and the background-dominated sample. In order to calculate Calibration, Light Level, and Coherent modeling systematics, we had to create a pure sample of charged-current Coherent signal events to conduct systematic studies due to technical constraints such as pre-staging PID (Particle Identification Files).

8.2 Target normalization

In order to calculate the systematic due to target normalization, the fiducial volume was changed by 30%, and the percentage uncertainty of the Data/MC ratio was calculated (i.e. 1.04%). Then the quadrature sum was calculated considering POT uncertainty: 0.5% (from [78]) and the percentage error of the target mass: 0.62% (from Section 7.3.1)

8.3 Neutrino flux

The PPFX multi-universe approach [94] is utilized to evaluate the uncertainty in flux caused by the mis-modeling of hadron production in the beamline. Each data point, whether it is the total cross section for an interaction or the production of a particle with varying characteristics, is considered a parameter. In each universe, these parameters are assigned values by sampling from a multidimensional Gaussian distribution centered around the default parameter values, incorporating covariances that account for uncertainties and correlations from the data. PPFX calculates the correction for the default Monte Carlo (MC) model in each universe and provides the corresponding values (weights) per neutrino, which are then stored and associated with the corresponding neutrino interaction. These resulting weights are used to calculate the variance of any kinematic variable, thereby correcting for the expected neutrino yield.

The total uncertainty is computed using the CAFAna tools. Contributions from different categories are also presented but are calculated directly using PPFX on the G4NuMI ntuples without being propagated through CAFAna. The overall uncertainty around the focusing peak is approximately 8%, arising predominantly from pions generated during interactions between the primary proton beam and the target, nucleon interactions occurring outside the target, and interactions involving incident mesons. A detailed description of each category can be found in [94].

The uncertainty in flux resulting from the mismodeling of the beamline geometry is obtained from the work described in [95]. While oscillation analyses take this uncertainty into account as a function of neutrino energy, this analysis is calculated based on the neutrino's 3-momentum to capture the resultant uncertainty in the beam's angular distribution.

Since we are using the same neutrino flux used in ν_μ Charged-Current Inclusive π^0 analysis, the percentage uncertainty of neutrino flux is taken from [78].

8.4 Background Estimate

In Section 7.1.2 we have already demonstrated that the dominant background is Charged Current Resonant. Therefore, it makes sense to apply $\pm 1\sigma$ to the CCRESMa and CCRESMv knobs and assess the implications for the background prediction made for the signal region. The background prediction (in subsection 7.1.4) was varied by applying the $\pm 1\sigma$ change to **CCRESMa** when calculating the $|t|$ ratio (in subsection 7.1.3. After the integral was calculated for each prediction, the fractional error was calculated.

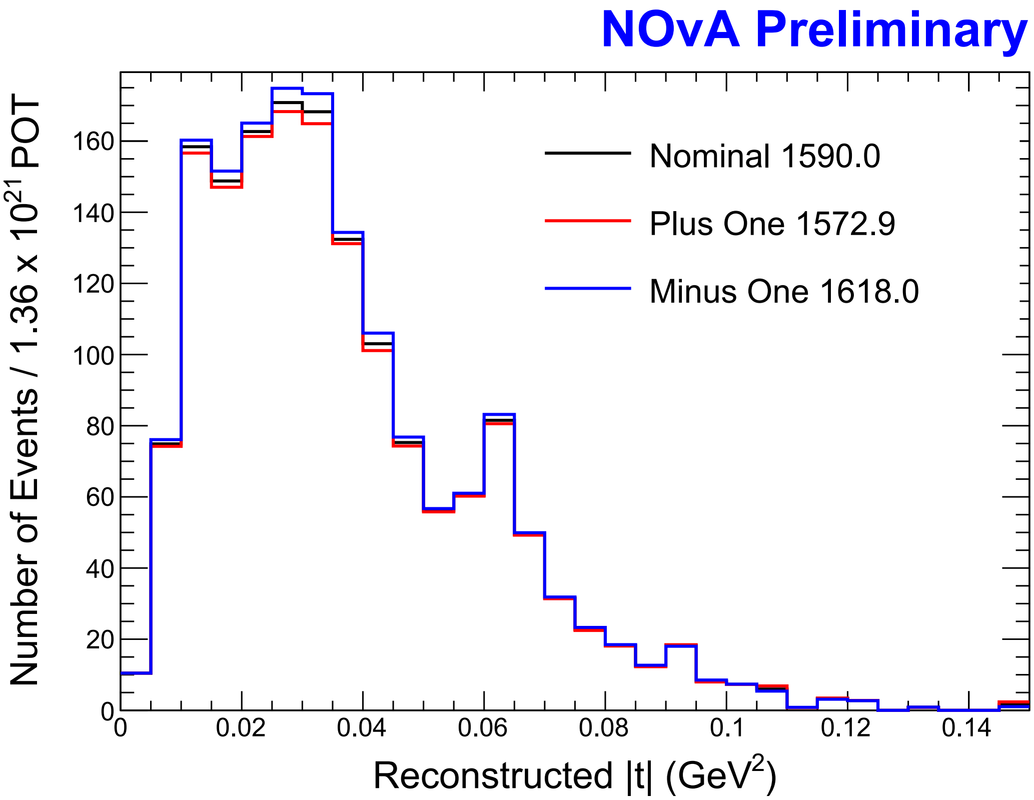

Figure 8.1 Plot of Background Prediction for different MaCCRES shifts $\{Nominal, +1\sigma, -1\sigma\}$

$$Fractional\ Error \;=\; 0.014 \tag{8.1}$$

The background prediction (in subsection 7.1.4) was varied by applying the $\pm 1\sigma$ shift to **CCRESMv** when calculating the $|t|$ ratio (in subsection 7.1.3). After calculating the integral for each prediction, the fractional error was calculated.

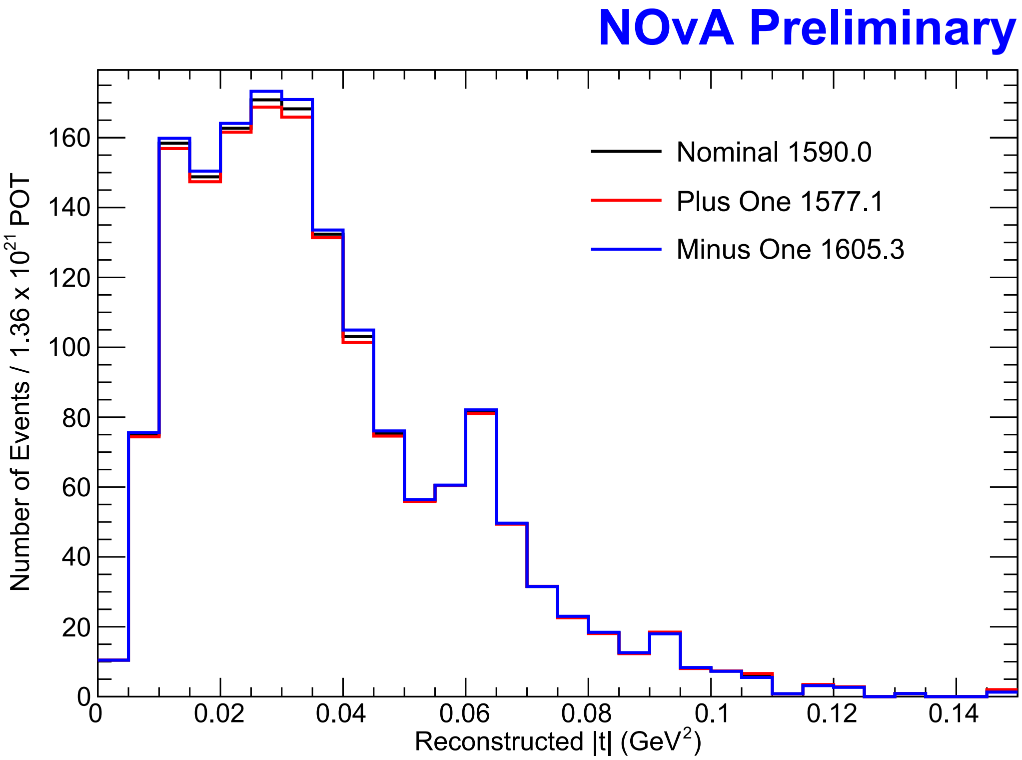

Figure 8.2 Plot of Background Prediction for different MvCCRES shifts $\{Nominal, +1\sigma, -1\sigma\}$

$$Fractional\ Error \;=\; 0.009 \tag{8.2}$$

Finally, the quadrature sum was calculated using the results 8.1 and 8.2. The systematic due to background estimation is 1.7%.

8.5 COHERENT MODELING

Unfortunately, the official GENIE re-weight knob made to change the axial mass of the coherent interactions was broken, we were advised to use the re-weight **kCOHCCScaleSyst2018** to apply the change 20%.

Since this change only applies a 20% change to normalization (not to the shape), we have decided to create the GENIE spline for ν_μ charged current coherent interactions as a function of neutrino energy only by applying the 20% shift to the axial mass defined in the Berger-Sehgal model. Then the cross-section ratio (i.e. shifted spline to the nominal spline) as a function of neutrino energy was calculated (as shown in Figure 8.3). Our strategy was to use the cross-section ratio as a reweight to calculate the efficiency shifted and then to calculate the percentage error of efficiency due to the shift 20% in the axial mass. The calculated percentage error in efficiency is 0.08%. Therefore, we have decided to use the result published in [79] and the change 50% scaled for 20% to match **kCOHCCScaleSyst2018**. The systematic due to coherent modeling is 1.5%.

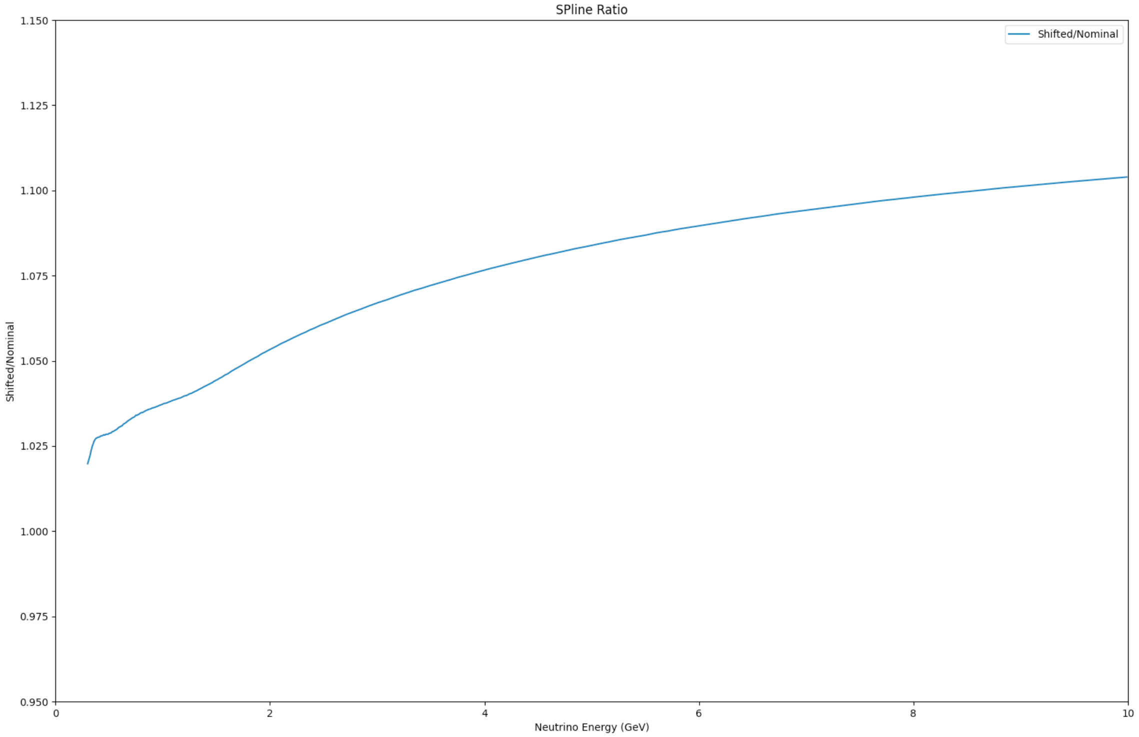

Figure 8.3 Plot of ν_μ CC Coherent cross-section ratio after applying 20% shift to $CCCOH\_Ma$ knob as a function of neutrino energy

8.6 MUON ENERGY SCALE

The Muon energy errors at the Near Detector are computed, and the Muon Catcher is analyzed independently, with the primary influence arising from Geant4's handling of the Bethe density effect. In this context, the most substantial uncertainty at the Near Detector is caused by stray hits resulting from neutron capture pile-up. Other contributing factors have a comparatively minor impact, with the most notable sources, listed in descending order, being external measurements of the mean excitation energies of elements, accounting for detector mass, and adjustments to energy loss due to chemical binding. The systematic uncertainty due to the muon energy scale was calculated using Monte Carlo studies. We evaluated the muon energy scale considering the maximum error, from the density effect and Geant4 validation, of 0.8% for the main detector and 1.2% for the muon catcher. Therefore, a constant shift (ΔE) for the muon energy scale is shown in Equation 8.3.

$$E_{\mu}^{shifted} = E_{\mu}(1 + \Delta E) \tag{8.3}$$

The choice for $\Delta E = 1.2\%$ was selected by using the highest energy loss of muons in the detector. A detailed analysis of muon energy loss can be found in [80]. The systematic result of the muon energy scale was calculated, that is, 0.7%.

8.7 PION ENERGY SCALE

The systematic uncertainty due to the pion energy scale was calculated using Monte Carlo studies. The systematic pion energy scale was evaluated by introducing a constant shift that is similar to the typical hadron energy scale in the NOvA analysis, and we selected the offset of the fractional resolution of the pion energy in Figure 6.13. (ΔE) for the pion energy scale was introduced as shown in Equation 8.4.

$$E_{\pi}^{shifted} = E_{\pi}(1 + \Delta E) \tag{8.4}$$

The choice for $\Delta E = 4\%$ was selected by rounding off the offset in the mean of Figure 6.13. The systematic calculated due to the Pion Energy scale is 1.1%.

8.8 Light level

In the 2017 simulation, the scintillator response model incorporates the generation of Cherenkov light. The variability in the light model is a result of uncertainties in both the scintillator's overall light yield and its efficiency in absorbing Cherenkov photons and re-emitting them at detectable wavelengths. To address these uncertainties, systematically altered Monte Carlo (MC) samples are created by adding hit variables to evaluate the effects of these factors. We have created a pure sample of CC coherent events. By running ART producer modules to apply standard NOvA shifts to light levels, systematic effects for PionID, HitID, and Kinematic ID were studied. We made histograms for Nominal, light level shift up and down samples by plotting PionID. Then we calculated the cumulative histogram for each case and finally divided all three histograms by nominal cumulative histograms to compare the variations in Figure

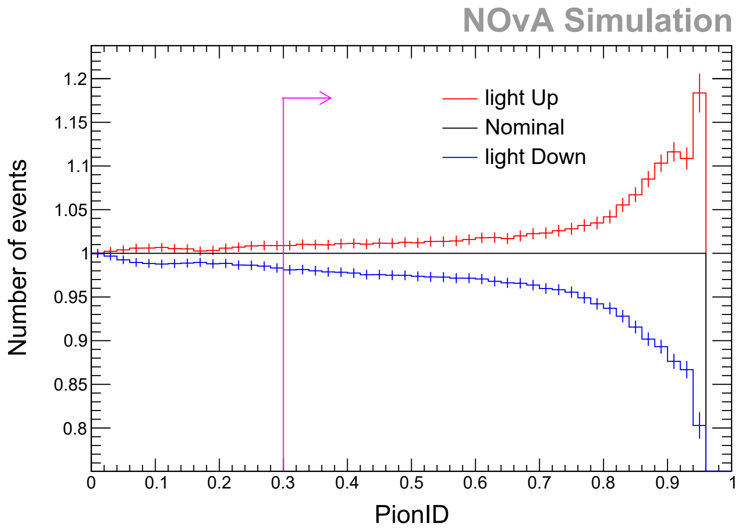

Figure 8.4 Plots of Cumulative Ratios made for PionID by introducing light level shifts

8.4. To calculate the systematic uncertainty due to light-level shifts, the efficiency was calculated at the cut value (i.e. PionID = 0.3). The calculated efficiencies can be found in Table 8.5.

Figure 8.5 Efficiency calculations for each light level shift for PionID cut

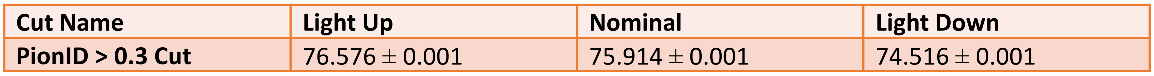

Cut Name	**Light Up**	**Nominal**	**Light Down**
PionID > 0.3 Cut	76.576 ± 0.001	75.914 ± 0.001	74.516 ± 0.001

$$Fractional\ Error = 1.36\% \tag{8.5}$$

We followed the same procedure to calculate light-level systematics for the HitID

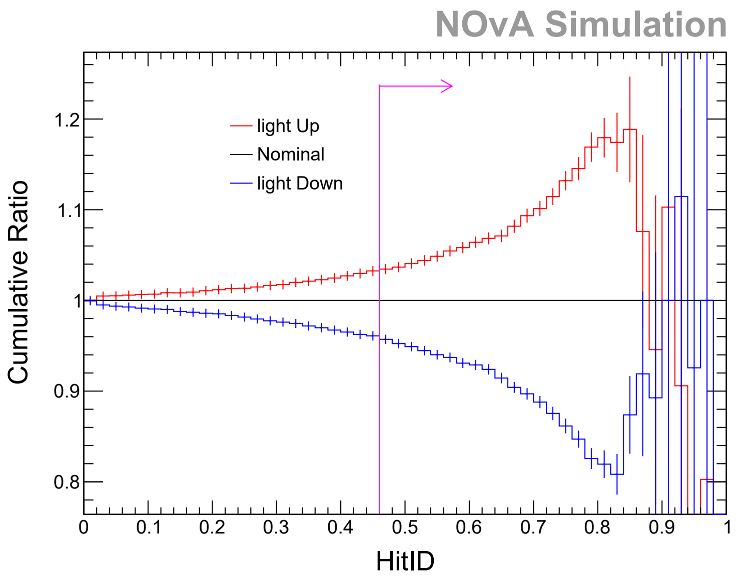

Figure 8.6 Plots of Cumulative Ratios made for HitID by introducing light level shifts

variable. Figure 8.6 includes the cumulative ratios made for the nominal, light-level-up, and light-level-down samples. At the cut value (i.e.HitID = 0.46), efficiencies were calculated for each sample and recorded in Table 8.1

$$Fractional\ Error = 3.83\% \tag{8.6}$$

Table 8.1 Efficiency calculations for each light level shift for HitID cut

Cut Name	Light Up	Nominal	Light Down
HitID > 0.46 Cut	83.489 ± 0.001	80.724 ± 0.001	77.299 ± 0.001

8.9 DETECTOR CALIBRATION

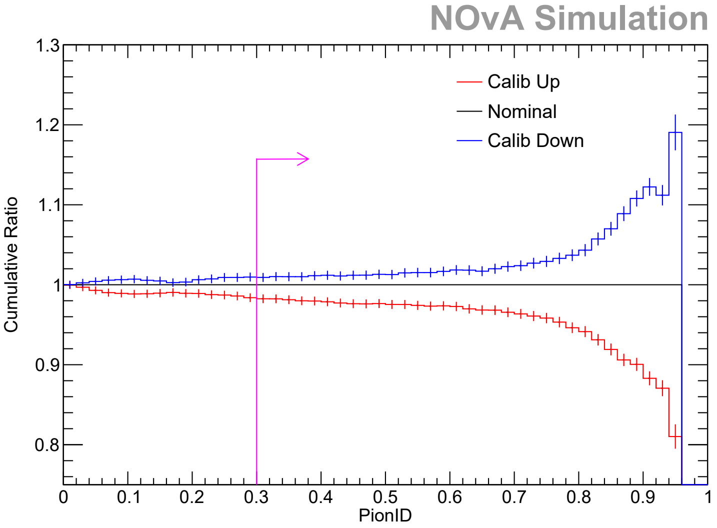

Figure 8.7 Plots of Cumulative Ratios made for PionID by introducing calibration shifts

In order to address uncertainties due to calibration effects, systematically altered Monte Carlo (MC) samples are created by adding hit variables to evaluate the effects of these factors. We have created a pure sample of CC coherent events. ART producer modules were run to apply standard NOvA shifts of calibration systematic effects to study PionID, HitID, and Kinematic ID. We made histograms for nominal, calibration shifts up-and-down samples by plotting PionID. Then we calculate the cumulative histogram for each case and finally divide the three histograms by the nominal cumulative histograms to compare the variations in Figure 8.7. To calculate the systematic uncertainty due to calibration shifts, the efficiency was calculated at the cut value (i.e. PionID = 0.3). The calculated efficiencies can be found in Table

Table 8.2 Efficiency calculations for each calibration shift for PionID cut

Cut Name	Calib Up	Nominal	Calib Down
PionID > 0.3 Cut	74.613 ± 0.001	75.907 ± 0.001	76.581 ± 0.001

8.2.

$$Fractional\ Error = 1.3\% \tag{8.7}$$

We followed the same procedure to calculate calibration systematics for the HitID variable. Figure 8.8 includes the cumulative ratios made for the nominal, calibration up and calibration down samples. At the cut value (i.e.HitID = 0.46), efficiencies

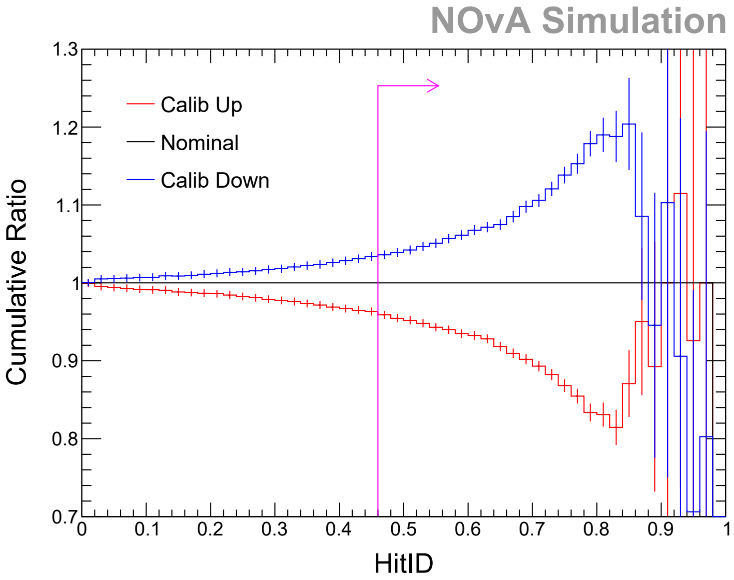

Figure 8.8 Plots of Cumulative Ratios made for HitID by introducing calibration shifts

Table 8.3 Efficiency calculations for each calibration shift for HitID cut

Cut Name	Calib Up	Nominal	Calib Down
HitID > 0.46 Cut	77.462 ± 0.001	80.735 ± 0.001	83.619 ± 0.001

were calculated for each sample and recorded in Table 8.3

$$Fractional\ Error = 3.81\% \tag{8.8}$$

After calculating fractional errors for absolute efficiency in each systematic variation, all results were summarized in Table 8.4 below. Systematic uncertainty at the light level: 4.1% was calculated taking the quadrature sum of the results 8.5 and 8.6. Similarly, systematic uncertainty due to calibration effects: 4.0% was calculated taking the quadrature sum of the results 8.7, 8.8.

Table 8.4 List of systematic and statistical uncertainties.

Source	$\delta(\%)$
Statistical Uncertainty	**4.6**
Target Normalization	1.3
Neutrino Flux	8.3
Background Estimate	1.7
Coherent Modeling	1.5
Muon Energy Scale	0.7
Pion Energy Scale	1.1
Light Level	4.1
Detector Calibration	4.0
Systematic Uncertainty	**10.4**
Total Uncertainty	**11.5**

Therefore, the total uncertainty of our total cross-section measurement is 11.5%.

8.10 BACKGROUND SYSTEMATICS

We are largely insensitive to the details of the background model, since we extract our background prediction directly from the data (see Sect. 7.1.3. It is also important to study systematic uncertainties using background-dominated samples. Due to prestaging limitations, we granted permission only to pre-stage about 2000 PID files in each variation (official light level and calibration samples made by the NOvA production group) to add hit variables and to study systematics. The neutrino interactions are heavily dominated by backgrounds such as CCRES.

8.10.1 VARIATIONS OF DETECTED LIGHT

We created Monte-Samples by adding hit variables to light-level samples, and cumulative ratios were graphed in Figure 8.9. At the cut value (i.e. PionID=0.3) we calculated efficiencies. The calculated efficiencies can be found in Table 8.5.

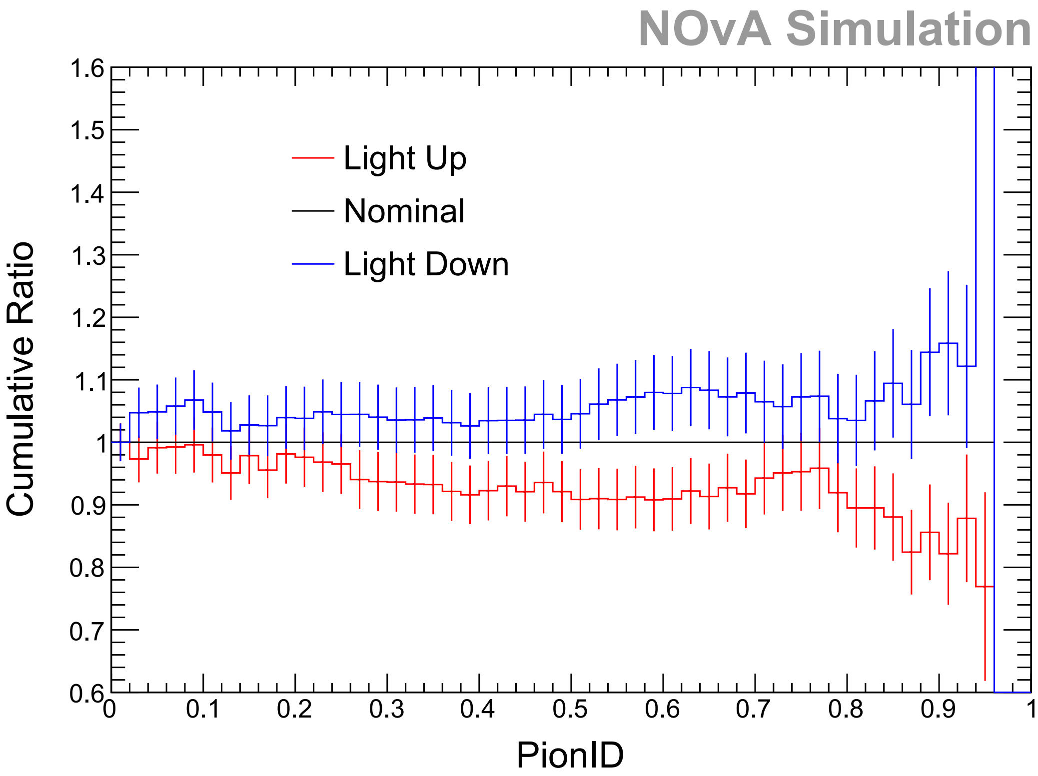

Figure 8.9 Plots of PionID with the presence of Light Level Up, Down and No Shifts

Table 8.5 PionID Cut Efficiency comparison Light Level Up, Down and No Shifts

Cut Name	LightUp	Nominal	LightDown
PionID > 0.3 Cut	33.67 ± 0.04	35.96 ± 0.04	37.24 ± 0.04

Similar to plotting cumulative ratio histograms for the PionID variable, cumulative ratio histograms for hitID graphs were made in Figure 8.10.

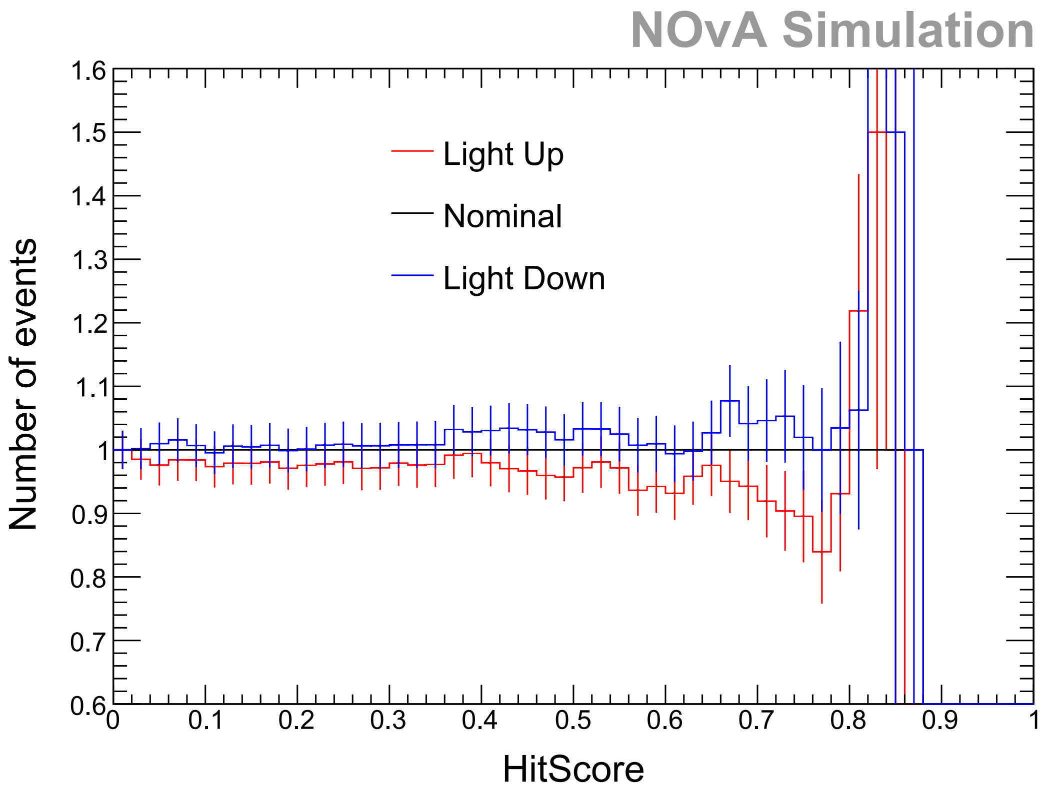

Figure 8.10 Plots of HitID with the presence of Light Level Up, Down, and No Shifts

At the cut value (i.e. HitID > 0.46) the efficiencies for Nominal, light level up and down samples were calculated and recorded in Table 8.6.

Table 8.6 HitID Cut Efficiency comparison Light Level Up, Down and No Shifts

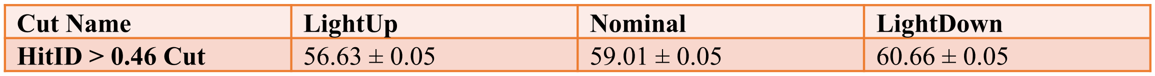

Cut Name	**LightUp**	**Nominal**	**LightDown**
HitID > 0.46 Cut	56.63 ± 0.05	59.01 ± 0.05	60.66 ± 0.05

8.10.2 Variations of detector calibration

Like we investigate light level shifts, Monte-Carlo samples were made to study variations due to calibration shifts by adding Hit variables. The histograms were made for PionID and HitID variables. Then the cumulative histograms were created and

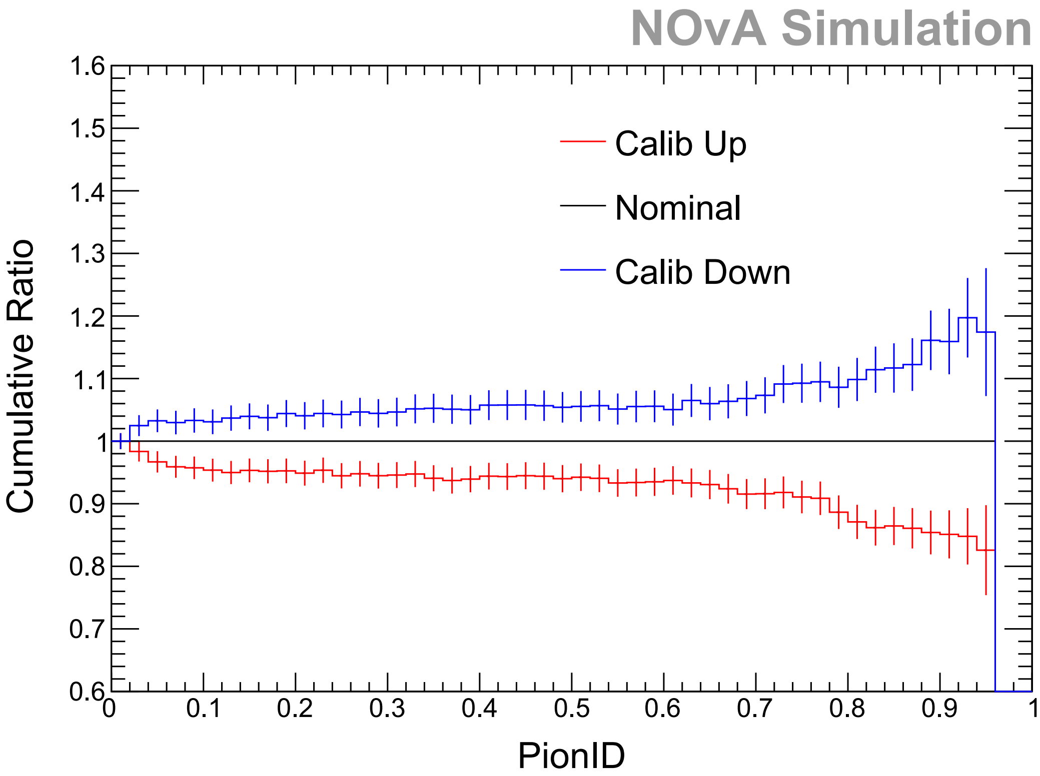

Figure 8.11 Plots of PionID with the presence of Calibration Up, Down, and No Shifts

Table 8.7 Background Predictions made by using Nominal

Cut Name	**CalibUp**	**Nominal**	**CalibDown**	**CalibShape**
PionID > 0.3 Cut	32.21 ± 0.01	34.06 ± 0.01	35.64 ± 0.01	33.78 ± 0.01

finally cumulative ratios were made. In Figure 8.11 cumulative ratios were made for nominal, calibration up and down samples divided by nominal cumulative histogram.

At the cut value (i.e. PionID = 0.3) the efficiencies were calculated and recorded in Table 8.7.

By following the same procedure, cumulative histograms were made for nominal, calibration up and down. After dividing each histogram by nominal histogram, cumulative ratios for nominal, calibration up and down samples were graphed in Figure

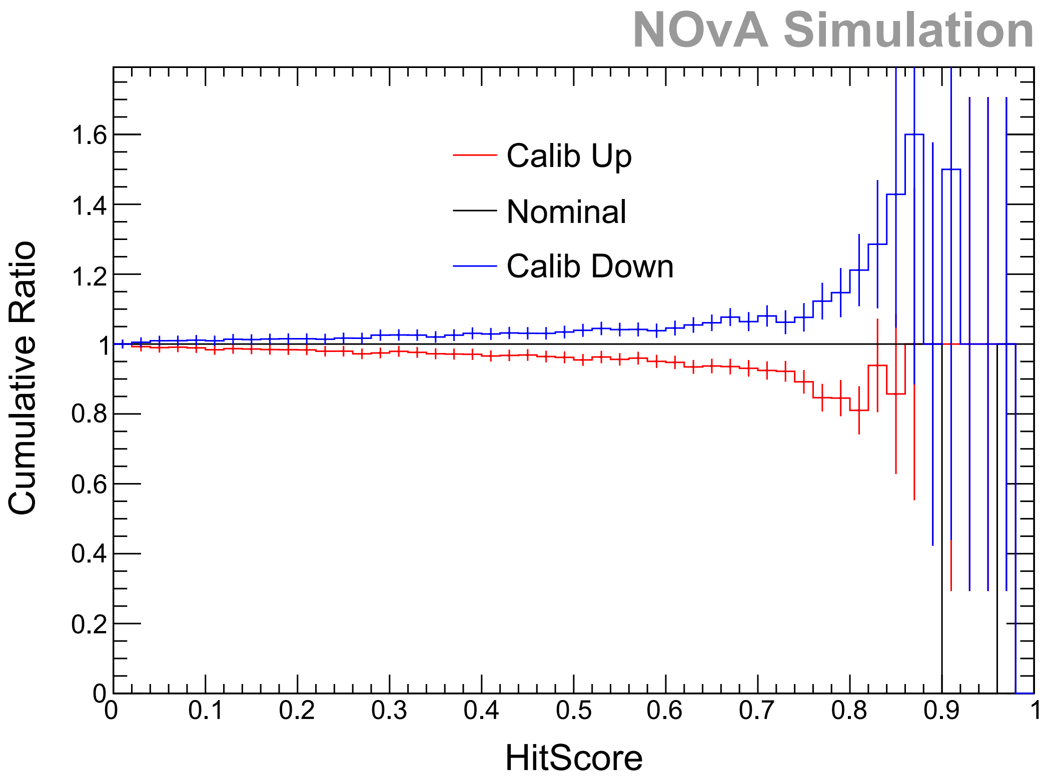

Figure 8.12 Plots of HitID with the presence of Calibration Up, Down and No Shifts

8.12.

The efficiencies at the cut value (i.e. HitID=0.46) were calculated and recorded in Table 8.8

Table 8.8 PionID Cut Efficiency comparison Calibration Up, Down and No Shifts

Cut Name	**CalibUp**	**Nominal**	**CalibDown**	**CalibShape**
HitID > 0.46 Cut	51.99 ± 0.01	53.92 ± 0.01	55.57 ± 0.01	53.48 ± 0.01

Chapter 9

Results and Summary

9.1 Comparing Data to Total MC in Signal Region

After granting permission to look at the data in the signal region, the histogram of reconstructed $|t|$ was made for the data and compared to the total MC histogram shown in Figure 9.1. In order to study data/MC agreement, we also calculated Data/MC ratio.

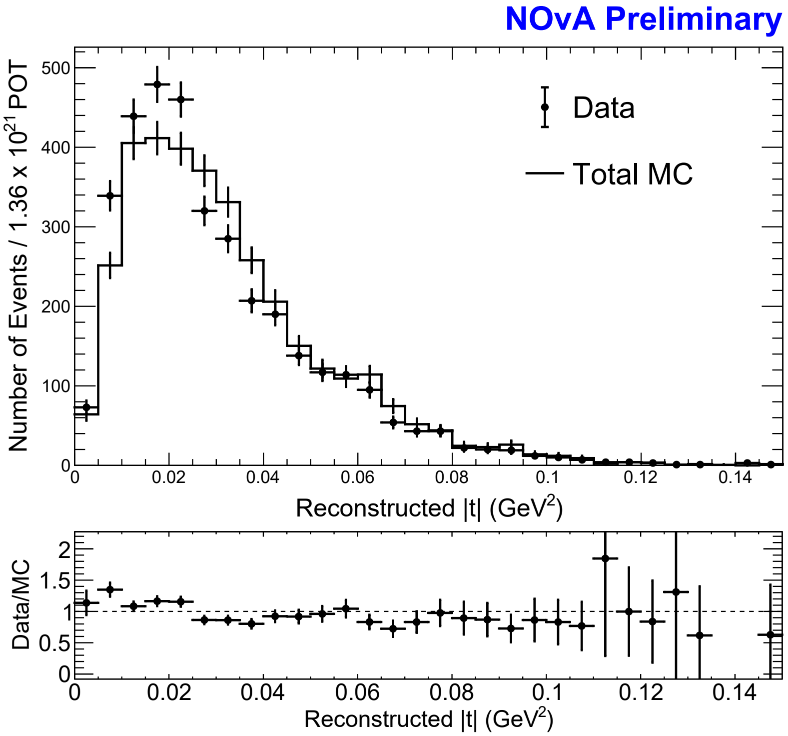

Figure 9.1 Plot of reconstructed $|t|$ Data Vs Total MC in signal region

9.2 Extraction of the Number of Signal Events

In order to extract candidates for the charged current coherent signal, the reconstructed $|t|$ using the data histogram (as explained in Section 9.1) was subtracted by the predicted background based on the data $|t|$ calculated in Section 7.1.4. This is the same procedure as that followed in section 7.2 by replacing the reconstructed $|t|$ total Monte Carlo histogram with the reconstructed $|t|$ histogram made using the data in the signal region.

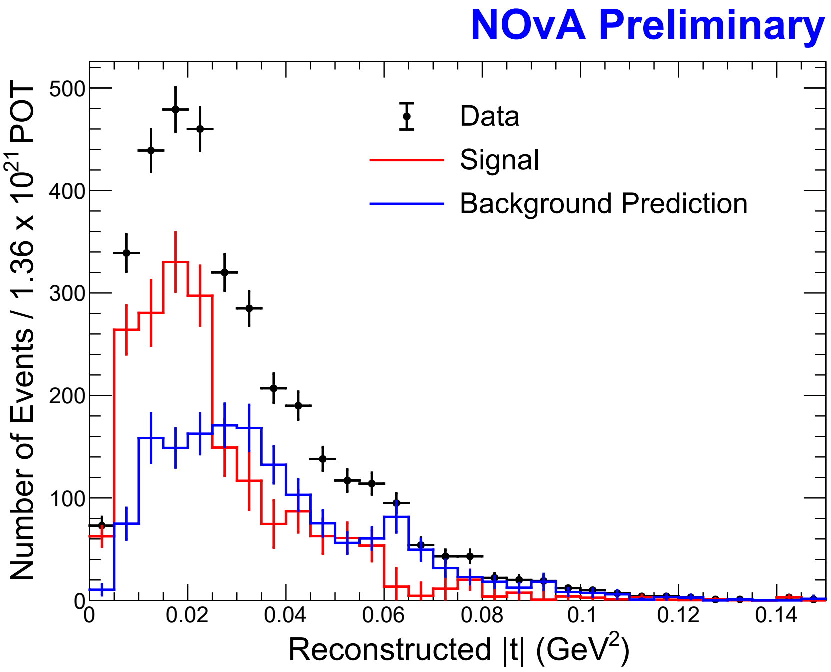

Figure 9.2 Plot of total $|t|$ Data-based prediction using Signal MC

Then the integrals of the following histograms were calculated with errors bin by bin (the final error was calculated by summing the quadrature of errors bin by bin):

- Reconstructed $|t|$ using data
- Data-based prediction
- Extracted Signal $|t|$

Table 9.1 contains integrals of the histograms with errors.

Table 9.1 Integrals of the histograms with errors (signal events extracted by using Figure 9.2)

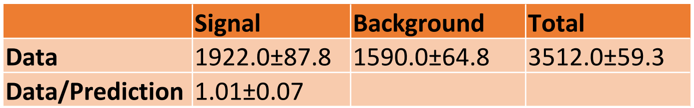

	Signal	**Background**	**Total**
Data	1922.0±87.8	1590.0±64.8	3512.0±59.3
Data/Prediction	1.01±0.07		

9.3 Comparing Signal histograms (Data Vs MC) in Signal Region

The reconstructed $|t|$ histograms for the signal was made using data (already explained in Section 9.2) and compared with the signal histogram calculated in Section 7.2. The data / MC signal ratio is also plotted in Figure 9.3.

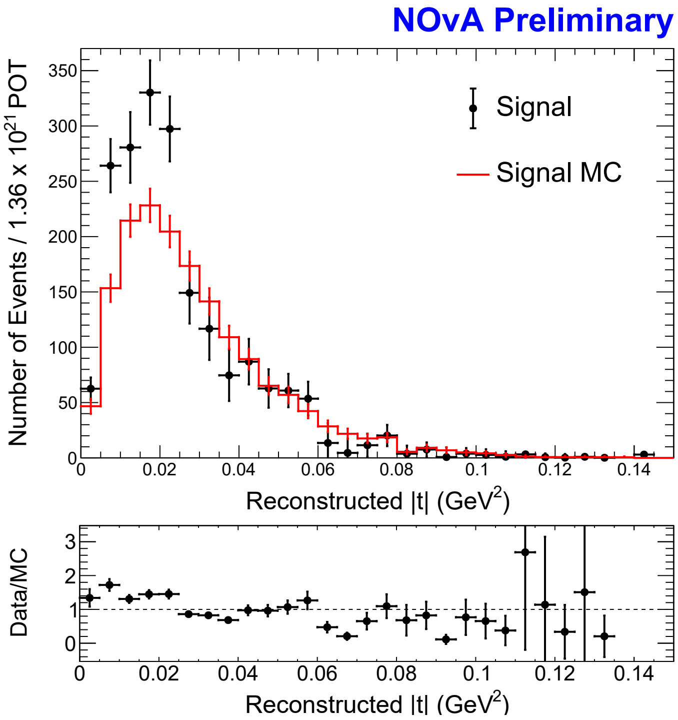

Figure 9.3 Plot of reconstructed $|t|$ histograms for signal Data Vs MC based in signal region

9.4 Cross-Section from extracted Signal Events from Data

By using the number of signal events in Table 9.1 and the details used to calculate the flux average cross-section using fake data in section 7.3.3, the cross-section measurement was calculated and marked in Figure 9.4.

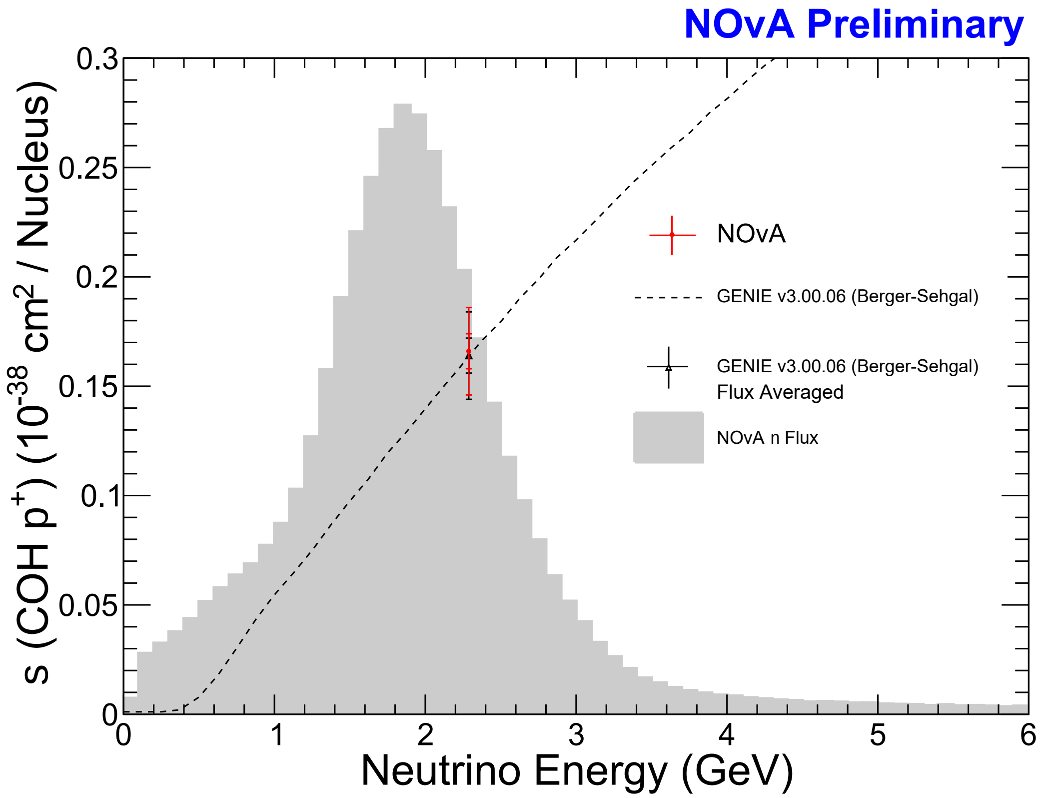

Figure 9.4 Plot of total cross-section as a function of Neutrino Energy

The flux averaged cross-section we obtained is:

$$\sigma = 1.66 \pm 0.08(stat.) \pm 0.17(syst.) \times 10^{-39} cm^2/nucleus \tag{9.1}$$

After scaling to C^{12} target by multiplying $(A/12)^{\frac{2}{3}}$:

$$\sigma = 2.00 \pm 0.08(stat.) \pm 0.17(syst.) \times 10^{-39} cm^2/C^{12} \tag{9.2}$$

9.5 Comparison with world data

After calculating the flux-averaged total cross-section measurement, it was scaled to the C12 target. For the final result obtained for the NOvA experiment, a comparison was made with existing results. Figure 9.5 contains the coherent cross-section measurement of NOvA NuMu CC π^+ (in red) compared to existing measurements as a function of neutrino energy. The dashed line represents the theoretical prediction as a function of neutrino energy, and it was drawn by using the Berger-Sehgal model. Table 8.2 contains details of the existing measurements.

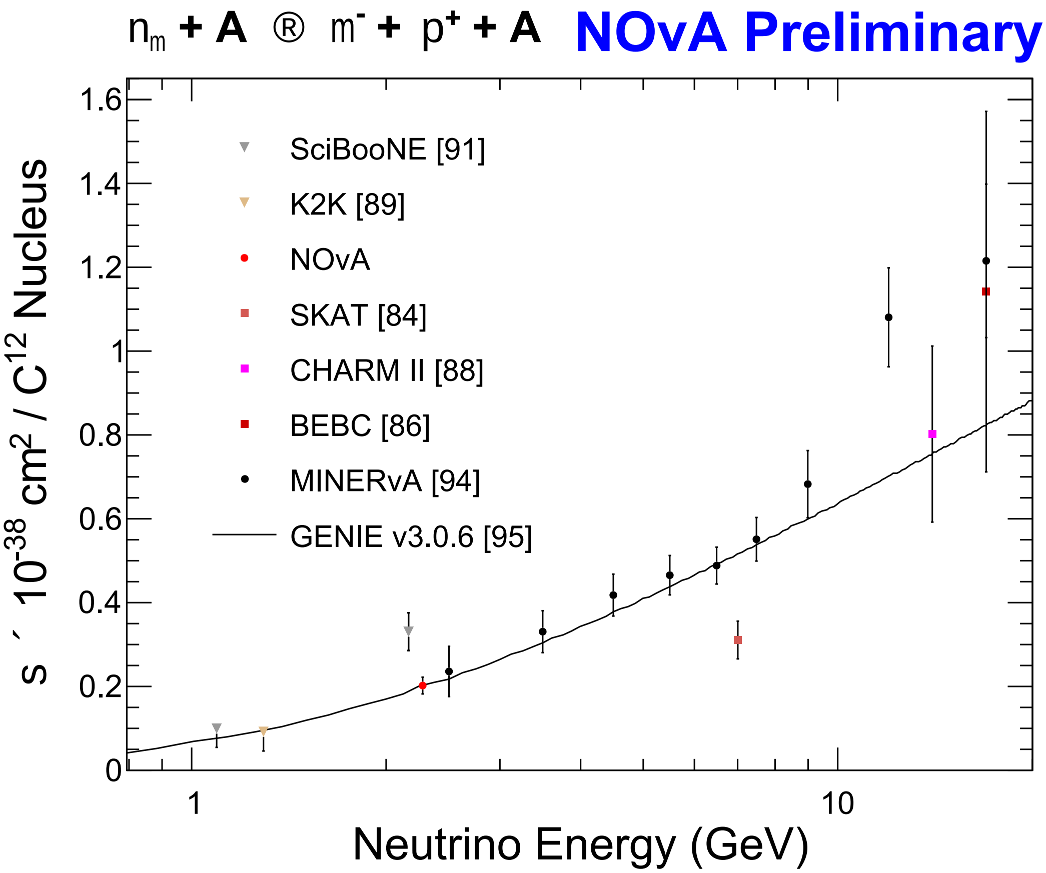

Figure 9.5 Comparing NOvA total cross-section to existing measurements as a function of Neutrino Energy

Table 9.2 Table of existing cross-section measurements

Experiment	Target $\left(\mathbf{A}^{\mathrm{eff}}\right)$	$\mathbf{E}_\nu$ [**GeV**]	Reac.	Cross-Section [10^{-40} cm^2/ nucleus]	Ref
Aachen-Padova	Aluminium (27)	2	NCν_μ	29 ± 10	[81]
Aachen-Padova	Aluminium (27)	2	NC$\bar{\nu}_\mu$	25 ± 7	[81]
Gargamelle	Freon (30)	3.5	NCν_μ	31 ± 20	[82]
Gargamelle	Freon (30)	3.5	NC$\bar{\nu}_\mu$	45 ± 24	[82]
CHARM	Marble (20)	31	NCν_μ	96 ± 42	[83]
CHARM	Marble (20)	24	NC$\bar{\nu}_\mu$	79 ± 26	[83]
SKAT	Freon (30)	7	NCν_μ	52 ± 19	[84]
SKAT	Freon (30)	7	CCν_μ	106 ± 16	[84]
SKAT	Freon (30)	7	CC$\bar{\nu}_\mu$	113 ± 35	[84]
BEBC	Neon (20)	27	CC$\bar{\nu}_\mu$	175 ± 25	[85]
BEBC	Neon (20)	27	CC ν_μ	250 ± 49	[86]
FNAL E632	Neon (20)	91.1	CC$_\mu$	350 ± 80	[87]
FNAL E632	Neon (20)	74.5	CC $\bar{\nu}_\mu$	270 ± 110	[87]
CHARM II	Glass (20.7)	23.7	CC$_{\nu_\mu}$	168 ± 41	[88]
CHARM II	Glass (20.7)	19.1	CC $\bar{\nu}_\mu$	161 ± 40	[88]
K2K	Carbon (12)	1.3	CC$_\mu$	< 0.077(90%CL)	[89]
MiniBooNE	CH$_2$(12)	0.7	NCν_μ	$(0.195 \pm 0.075) \times \sigma_{\mathrm{NC}\pi^0}$	[90]
SciBooNE	Carbon (12)	1.1	CC$_{\nu_\mu}$	< 0.0844(90%CL)	[91]
SciBooNE	Carbon (12)	2.2	CC$_{\nu_\mu}$	< 0.287(90%CL)	[91]
NOMAD	Carbon (12.8)	25	NCν_μ	72.6 ± 10.6	[92]
SciBooNE	Carbon (12)	0.8	NCν_μ	$(0.012 \pm 0.002) \times \sigma_{\mathrm{CC}}$	[93]
MINERvA	CH(12)	2.5	CCν_μ	23.7 ± 6	[94]
MINERvA	CH(12)	3.5	CCν_μ	33 ± 5	[94]
MINERvA	CH(12)	4.5	CCν_μ	41.7 ± 5	[94]
MINERvA	CH(12)	5.5	CCν_μ	46.5 ± 5	[94]
MINERvA	CH(12)	6.5	CCν_μ	48.8 ± 4.4	[94]
MINERvA	CH(12)	7.5	CCν_μ	55 ± 5.2	[94]
MINERvA	CH(12)	9.0	CCν_μ	68.2 ± 7.8	[94]
MINERvA	CH(12)	12.0	CCν_μ	100.8 ± 11.8	[94]
MINERvA	CH(12)	17.0	CCν_μ	121.4 ± 18.3	[94]
NOvA	(15.9)	2.3	CCν_μ	16.6 ± 2.0	

In conclusion, we have measured the most precise ν_μ Charged Current Coherent π^+ total cross-section below 5GeV.!

Bibliography

[1]S. L. Glashow, “Partial-symmetries of weak interactions”, Nuclear physics **22**, 579–588 (1961).

[2]A. Salam, “Weak and Electromagnetic Interactions”, Conf. Proc. C **680519**, 367–377 (1968).

[3]S. Weinberg, “A model of leptons”, Phys. Rev. Lett. **19**, 1264–1266 (1967).

[4]F. Englert and R. Brout, “Broken symmetry and the mass of gauge vector mesons”, Phys. Rev. Lett. **13**, 321–323 (1964).

[5]P. W. Higgs, “Broken symmetries, massless particles and gauge fields”, Phys. Lett. **12**, 132–133 (1964).

[6]P. W. Higgs, “Broken symmetries and the masses of gauge bosons”, Phys. Rev. Lett. **13**, 508–509 (1964).

[7]G. S. Guralnik, C. R. Hagen, and T. W. B. Kibble, “Global Conservation Laws and Massless Particles”, Phys. Rev. Lett. **13**, edited by J. C. Taylor, 585–587 (1964).

[8]G. Aad et al. (ATLAS), “Observation of a new particle in the search for the Standard Model Higgs boson with the ATLAS detector at the LHC”, Phys. Lett. B **716**, 1–29 (2012).

[9]S. Chatrchyan et al. (CMS), “Observation of a New Boson at a Mass of 125 GeV with the CMS Experiment at the LHC”, Phys. Lett. B **716**, 30–61 (2012).

[10]L. Wolfenstein, “Neutrino oscillations in matter”, Phys. Rev. D **17**, 2369–2374 (1978).

[11] A. Mislivec, A. Higuera, L. Aliaga, L. Bellantoni, A. Bercellie, M. Betancourt, A. Bodek, A. Bravar, H. Budd, G. C. V., T. Cai, D. M. Caicedo, M. Carneiro, E. Chavarria, H. da Motta, S. Dytman, G. Dıaz, J. Felix, L. Fields, R. Fine, A. Gago, R. Galindo, H. Gallagher, A. Ghosh, R. Gran, D. Harris, K. Hurtado, D. Jena, J. Kleykamp, M. Kordosky, T. Le, E. Maher, S. Manly, W. Mann, C. Marshall, K. McFarland, B. Messerly, J. Miller, J. Morfın, J. Mousseau, D. Naples, J. Nelson, C. Nguyen, A. Norrick, Nuruzzaman, V. Paolone, G. Perdue, M. Ramırez, R. Ransome, H. Ray, L. Ren, D. Rimal, P. Rodrigues, D. Ruterbories, H. Schellman, C. S. Salinas, M. Sultana, S. S. Falero, N. Tagg, E. Valencia, M. Wospakrik, B. Yaeggy, and G. Z. and, "Measurement of total and differential cross sections of neutrino and antineutrino coherent production on carbon", Physical Review D **97**, `10.1103/physrevd.97.032014` (2018).

[12] R. P. Feynman, M. Kislinger, and F. Ravndal, "Current matrix elements from a relativistic quark model", Phys. Rev. D **3**, 2706–2732 (1971).

[13] K. Kim, H. Gil, and C. H. Hyun, "Quasielastic charged-current neutrino-nucleus scattering with nonrelativistic nuclear energy density functionals", Physics Letters B **833**, 137273 (2022).

[14] S. S. Gershtein and Y. B. Zeldovich, "Meson corrections in the theory of beta decay", Zh. Eksp. Teor. Fiz. **29**, edited by Y. A. Trutnev, 698–699 (1955).

[15] S. L. Glashow, J. Iliopoulos, and L. Maiani, "Weak Interactions with Lepton-Hadron Symmetry", Phys. Rev. D **2**, 1285–1292 (1970).

[16] A. Bodek, S. Avvakumov, R. Bradford, and H. S. Budd, "Extraction of the axial nucleon form-factor from neutrino experiments on deuterium", J. Phys. Conf. Ser. **110**, edited by R. Barlow, 082004 (2008).

[17] H. Gallagher, G. Garvey, and G. P. Zeller, "Neutrino-nucleus interactions", Ann. Rev. Nucl. Part. Sci. **61**, 355–378 (2011).

[18] M. Glück, E. Reya, and A. Vogt, “Dynamical parton distributions revisited”, The European Physical Journal C **5**, 461–470 (1998).

[19] J. Delorme and M. Ericson, “Exploration of the Spin - Isospin Nuclear Response Function by Neutrinos”, Phys. Lett. B **156**, 263–266 (1985).

[20] O. Lalakulich, U. Mosel, and K. Gallmeister, “Neutrino energy reconstruction in quasielastic-like scattering in the MiniBooNE and t2k experiments”, Physical Review C **86**, `10.1103/physrevc.86.054606` (2012).

[21] K. Gallmeister, U. Mosel, and J. Weil, “Neutrino-induced reactions on nuclei”, Phys. Rev. C **94**, 035502 (2016).

[22] O. Lalakulich, K. Gallmeister, and U. Mosel, “Erratum: many-body interactions of neutrinos with nuclei: observables [phys. rev. c 86, 014614 (2012)]”, Phys. Rev. C **90**, 029902 (2014).

[23] U. Mosel, O. Lalakulich, and K. Gallmeister, “Reaction mechanisms at MINERνA”, Phys. Rev. D **89**, 093003 (2014).

[24] A. Bodek, H. S. Budd, and M. E. Christy, “Neutrino quasielastic scattering on nuclear targets”, The European Physical Journal C **71**, `10.1140/epjc/s10052-011-1726-y` (2011).

[25] M. Martini, M. Ericson, and G. Chanfray, “Neutrino energy reconstruction problems and neutrino oscillations”, Phys. Rev. D **85**, 093012 (2012).

[26] M. Martini, M. Ericson, and G. Chanfray, “Energy reconstruction effects in neutrino oscillation experiments and implications for the analysis”, Phys. Rev. D **87**, 013009 (2013).

[27] M. Martini, M. Ericson, G. Chanfray, and J. Marteau, “Neutrino and antineutrino quasielastic interactions with nuclei”, Phys. Rev. C **81**, 045502 (2010).

[28] M. Martini, N. Jachowicz, M. Ericson, V. Pandey, T. Van Cuyck, and N. Van Dessel, “Electron-neutrino scattering off nuclei from two different theoretical perspectives”, Phys. Rev. C **94**, 015501 (2016).

[29] M. Ericson and M. Martini, “Neutrino versus antineutrino cross sections and cp violation”, Phys. Rev. C **91**, 035501 (2015).

[30] J. Nieves, F. Sanchez, I. Ruiz Simo, and M. J. Vicente Vacas, “Neutrino energy reconstruction and the shape of the ccqe-like total cross section”, Phys. Rev. D **85**, 113008 (2012).

[31] J. Nieves, I. Ruiz Simo, and M. J. Vicente Vacas, “Inclusive charged–current neutrino–nucleus reactions”, Phys. Rev. C **83**, 045501 (2011).

[32] J. Nieves, I. Ruiz Simo, and M. J. Vicente Vacas, “The nucleon axial mass and the miniboone quasielastic neutrino-nucleus scattering problem”, Phys. Lett. B **707**, 72–75 (2012).

[33] J. Nieves, I. Ruiz Simo, and M. J. Vicente Vacas, “Two particle-hole excitations in charged current quasielastic antineutrino–nucleus scattering”, Phys. Lett. B **721**, 90–93 (2013).

[34] R. Gran, J. Nieves, F. Sanchez, and M. J. Vicente Vacas, “Neutrino-nucleus quasi-elastic and 2p2h interactions up to 10 gev”, Phys. Rev. D **88**, 113007 (2013).

[35] J. E. Amaro, M. B. Barbaro, J. A. Caballero, T. W. Donnelly, and C. F. Williamson, “Meson-exchange currents and quasielastic neutrino cross sections in the superscaling approximation model”, Phys. Lett. B **696**, 151–155 (2011).

[36] J. E. Amaro, M. B. Barbaro, J. A. Caballero, T. W. Donnelly, and J. M. Udias, “Relativistic analyses of quasielastic neutrino cross sections at miniboone kinematics”, Phys. Rev. D **84**, 033004 (2011).

[37] J. E. Amaro, M. B. Barbaro, J. A. Caballero, and T. W. Donnelly, “Meson-exchange currents and quasielastic antineutrino cross sections in the superscaling approximation”, Phys. Rev. Lett. **108**, 152501 (2012).

[38] I. Ruiz Simo, C. Albertus, J. E. Amaro, M. B. Barbaro, J. A. Caballero, and T. W. Donnelly, “Relativistic effects in two-particle emission for electron and neutrino reactions”, Phys. Rev. D **90**, 033012 (2014).

[39] I. Ruiz Simo, C. Albertus, J. E. Amaro, M. B. Barbaro, J. A. Caballero, and T. W. Donnelly, “Angular distribution in two-particle emission induced by neutrinos and electrons”, Phys. Rev. D **90**, 053010 (2014).

[40] G. D. Megias et al., “Meson-exchange currents and quasielastic predictions for charged-current neutrino-12c scattering in the superscaling approach”, Phys. Rev. D **91**, 073004 (2015).

[41] M. V. Ivanov, G. D. Megias, R. Gonzlez-Jimnez, O. Moreno, M. B. Barbaro, J. A. Caballero, and T. W. Donnelly, “Charged-current inclusive neutrino cross sections in the superscaling model including quasielastic, pion production and meson-exchange contributions”, J. Phys. G **43**, 045101 (2016).

[42] I. Ruiz Simo, J. E. Amaro, M. B. Barbaro, A. De Pace, J. A. Caballero, and T. W. Donnelly, “Relativistic model of 2p-2h meson exchange currents in (anti)neutrino scattering”, J. Phys. G **44**.

[43] H. De Vries, C. W. De Jager, and C. De Vries, “Nuclear charge and magnetization density distribution parameters from elastic electron scattering”, Atom. Data Nucl. Data Tabl. **36**, 495–536 (1987).

[44] C. Juszczak, J. A. Nowak, and J. T. Sobczyk, “Spectrum of recoil nucleons in quasi-elastic neutrino nucleus interactions”, Eur. Phys. J. C **39**, 195–200 (2005).

[45] J. Ż muda, K. Graczyk, C. Juszczak, and J. Sobczyk, "{\tt NuWro} monte carlo generator of neutrino interactions — first electron scattering results", Acta Physica Polonica B **46**, 2329 (2015).

[46] R. Shneor, P. Monaghan, R. Subedi, B. D. Anderson, K. Aniol, J. Annand, J. Arrington, H. Benaoum, F. Benmokhtar, P. Bertin, W. Bertozzi, W. Boeglin, J. P. Chen, S. Choi, E. Chudakov, E. Cisbani, B. Craver, C. W. de Jager, R. J. Feuerbach, S. Frullani, F. Garibaldi, O. Gayou, S. Gilad, R. Gilman, O. Glamazdin, J. Gomez, J.-O. Hansen, D. W. Higinbotham, T. Holmstrom, H. Ibrahim, R. Igarashi, E. Jans, X. Jiang, Y. Jiang, L. Kaufman, A. Kelleher, A. Kolarkar, E. Kuchina, G. Kumbartzki, J. J. LeRose, R. Lindgren, N. Liyanage, D. J. Margaziotis, P. Markowitz, S. Marrone, M. Mazouz, D. Meekins, R. Michaels, B. Moffit, S. Nanda, C. F. Perdrisat, E. Piasetzky, M. Potokar, V. Punjabi, Y. Qiang, J. Reinhold, B. Reitz, G. Ron, G. Rosner, A. Saha, B. Sawatzky, A. Shahinyan, S. Š irca, K. Slifer, P. Solvignon, V. Sulkosky, N. Thompson, P. E. Ulmer, G. M. Urciuoli, E. Voutier, K. Wang, J. W. Watson, L. B. Weinstein, B. Wojtsekhowski, S. Wood, H. Yao, X. Zheng, and L. Zhu, Physical Review Letters **99**, `10.1103/physrevlett.99.072501` (2007).

[47] M. M. Sargsian, T. V. Abrahamyan, M. I. Strikman, and L. L. Frankfurt, "Exclusive electro-disintegration of He-3 at high Q2. II. Decay function formalism", Phys. Rev. C **71**, 044615 (2005).

[48] R. Schiavilla, R. B. Wiringa, S. C. Pieper, and J. Carlson, "Tensor forces and the ground-state structure of nuclei", Phys. Rev. Lett. **98**, 132501 (2007).

[49] G. Co', *Random phase approximation and neutrino-nucleus cross sections*, 2006.

[50] R. Gran, *Model uncertainties for valencia rpa effect for minerva*, 2017.

[51] J. A. Caballero, C. E. Alonso, M. V. Andres, J. E Garcia-Ramos, and F. Perez-Bernal, eds., *Basic concepts in nuclear physics: Theory, experiments and applica-*

tions. Proceedings, International Scientific Meeting on Nuclear Physics, La Rabida, Spain, July 4-10, 2009, Vol. 1231 (2010), pp.1–270.

[52]L. Alvarez-Ruso, M. Sajjad Athar, M. Barbaro, D. Cherdack, M. Christy, P. Coloma, T. Donnelly, S. Dytman, A. de Gouvêa, R. Hill, P. Huber, N. Jachowicz, T. Katori, A. Kronfeld, K. Mahn, M. Martini, J. Morfın, J. Nieves, G. Perdue, R. Petti, D. Richards, F. Sánchez, T. Sato, J. Sobczyk, and G. Zeller, "NuSTEC white paper: status and challenges of neutrino–nucleus scattering", Progress in Particle and Nuclear Physics **100**, 1–68 (2018).

[53]S. L. Adler, "Tests of the conserved vector current and partially conserved axial-vector current hypotheses in high-energy neutrino reactions", Phys. Rev. **137**, AB4–AB4 (1965).

[54]D. Rein and L. M. Sehgal, "Coherent pi0 Production in Neutrino Reactions", Nucl. Phys. B **223**, 29–44 (1983).

[55]C. Berger, F. Sanchez, M. Sorel, and L. Alvarez-Ruso, "PCAC and coherent pion production by neutrinos", in AIP conference proceedings (2009).

[56]P. Adamson, K. Anderson, M. Andrews, R. Andrews, I. Anghel, D. Augustine, A. Aurisano, S. Avvakumov, D. Ayres, B. Baller, et al., "The numi neutrino beam", Nuclear Instruments and Methods in Physics Research Section A: Accelerators, Spectrometers, Detectors and Associated Equipment **806**, 279–306 (2016).

[57]D. S. Ayres et al. (NOvA), "The NOvA Technical Design Report", `10.2172/935497` (2007).

[58]N. A. et al. (NOvA), "NOvA DAQ Data formats-Definitions", (2017).

[59]E. Niner, P. Adamson, G. Deuerling, R. Kwarciany, H. Meyer, A. Norman, R. Rechenmacher, P. Shanahan, and N. Wilcer, "Synchronization of the 14 kTon NOνA neutrino detector with the Fermilab NuMI beam", J. Phys. Conf. Ser. **513**, edited by D. L. Groep and D. Bonacorsi, 012028 (2014).

[60]S. Agostinelli et al. (GEANT4), "GEANT4–a simulation toolkit", Nucl. Instrum. Meth. A **506**, 250–303 (2003).

[61]C. Andreopoulos, A. Bell, D. Bhattacharya, F. Cavanna, J. Dobson, S. Dytman, H. Gallagher, P. Guzowski, R. Hatcher, P. Kehayias, A. Meregaglia, D. Naples, G. Pearce, A. Rubbia, M. Whalley, and T. Yang, "The GENIE neutrino monte carlo generator", Nuclear Instruments and Methods in Physics Research Section A: Accelerators, Spectrometers, Detectors and Associated Equipment **614**, 87–104 (2010).

[62]R. Bradford, A. Bodek, H. Budd, and J. Arrington, "A new parameterization of the nucleon elastic form factors", Nuclear Physics B - Proceedings Supplements **159**, 127–132 (2006).

[63]D. Rein and L. M. Sehgal, "Neutrino Excitation of Baryon Resonances and Single Pion Production", Annals Phys. **133**, 79–153 (1981).

[64]H. Gallagher, "The NEUGEN neutrino event generator", Nucl. Phys. B Proc. Suppl. **112**, edited by J. G. Morfin, M. Sakuda, and Y. Suzuki, 188–194 (2002).

[65]P. A. Cherenkov, "Visible luminescence of pure liquids under the influence of γ-radiation", Dokl. Akad. Nauk SSSR **2**, 451–454 (1934).

[66]I. M. Frank and I. E. Tamm, "Coherent visible radiation of fast electrons passing through matter", Compt. Rend. Acad. Sci. URSS **14**, 109–114 (1937).

[67]J. B. Birks, "Scintillations from Organic Crystals: Specific Fluorescence and Relative Response to Different Radiations", Proc. Phys. Soc. A **64**, 874–877 (1951).

[68]C. N. Chou, "The Nature of the Saturation Effect of Fluorescent Scintillators", Phys. Rev. **87**, 904–905 (1952).

[69]M. Baird, J. Bian, M. Messier, E. Niner, D. Rocco, and K. Sachdev, "Event reconstruction techniques in nova", Journal of Physics: Conference Series **664**, 072035 (2015).

[70]L. A. Fernandes and M. M. Oliveira, “Real-time line detection through an improved hough transform voting scheme”, Pattern Recognition **41**, 299–314 (2008).

[71]M. Ohlsson, “Extensions and explorations of the elastic arms algorithm”, Computer Physics Communications **77**, 19–32 (1993).

[72]R. Krishnapuram and J. M. Keller, “A possibilistic approach to clustering”, IEEE Trans. Fuzzy Syst. **1**, 98–110 (1993).

[73]Y. Hu, C. Zuo, F. Qu, and W. Shi, “Unsupervised possibilistic clustering based on kernel methods”, Physics Procedia **25**, International Conference on Solid State Devices and Materials Science, April 1-2, 2012, Macao, 1084–1090 (2012).

[74]R. Frühwirth, “Application of kalman filtering to track and vertex fitting”, Nuclear Instruments and Methods in Physics Research Section A: Accelerators, Spectrometers, Detectors and Associated Equipment **262**, 444–450 (1987).

[75]E. D. Niner, “Observation of electron neutrino appearance in the numi beam with the nova experiment”, `10.2172/1221353` (2015).

[76]A. R. C. Backhouse, “The attenuation and threshold correction of the nova detectors.”, NOvA Collaboration Internal document 13579.

[77]M. A. Acero et al. (NOvA), “Measurement of the double-differential muon-neutrino charged-current inclusive cross section in the NOvA near detector”, Phys. Rev. D **107**, 052011 (2023).

[78]M. Acero, P. Adamson, G. Agam, L. Aliaga, T. Alion, V. Allakhverdian, S. Altakarli, N. Anfimov, A. Antoshkin, L. Asquith, E. Arrieta-Diaz, A. Aurisano, A. Back, M. Baird, N. Balashov, P. Baldi, B. Bambah, S. Bashar, K. Bays, S. Bending, R. Bernstein, V. Bhatnagar, B. Bhuyan, J. Bian, J. Blair, A. Booth, P. Bour, C. Bromberg, N. Buchanan, A. Butkevich, S. Calvez, M. Campbell, T. Carroll, E. Catano-Mur, S. Childress, B. Choudhary, B. Chowdhury, T. Coan, M. Colo, L. Corwin, L. Cremonesi, G. Davies, P. Derwent, R. Dharmapalan, P. Ding, Z.

Djurcic, M. Dolce, D. Doyle, E. Dukes, D. D. Tonguino, P. Dung, H. Duyang, S. Edayath, R. Ehrlich, G. Feldman, P. Filip, W. Flanagan, M. Frank, H. Gallagher, R. Gandrajula, F. Gao, S. Germani, A. Giri, R. Gomes, M. Goodman, V. Grichine, M. Groh, R. Group, B. Guo, A. Habig, F. Hakl, A. Hall, J. Hartnell, R. Hatcher, A. Hatzikoutelis, K. Heller, V. Hewes, A. Himmel, A. Holin, B. Howard, J. Huang, J. Hylen, F. Jediny, C. Johnson, M. Judah, I. Kakorin, D. Kalra, D. Kaplan, R. Keloth, O. Klimov, L. Koerner, L. Kolupaeva, S. Kotelnikov, A. Kreymer, M. Kubu, C. Kullenberg, A. Kumar, C. Kuruppu, V. Kus, T. Lackey, K. Lang, L. Li, S. Lin, A. Lister, M. Lokajicek, S. Luchuk, K. Maan, S. Magill, W. Mann, M. Marshak, M. Martinez-Casales, V. Matveev, B. Mayes, D. Méndez, M. Messier, H. Meyer, T. Miao, W. Miller, S. Mishra, A. Mislivec, R. Mohanta, A. Moren, L. Mualem, M. Muether, S. Mufson, K. Mulder, R. Murphy, J. Musser, D. Naples, N. Nayak, J. Nelson, R. Nichol, G. Nikseresht, E. Niner, A. Norman, A. Norrick, T. Nosek, A. Olshevskiy, T. Olson, J. Paley, R. Patterson, G. Pawloski, D. Pershey, O. Petrova, R. Petti, D. Phan, S. Phan-Budd, R. Plunkett, B. Potukuchi, C. Principato, F. Psihas, A. Radovic, A. Rafique, V. Raj, R. Rameika, B. Rebel, P. Rojas, V. Ryabov, O. Samoylov, M. Sanchez, S. S. Falero, I. Seong, P. Shanahan, A. Sheshukov, P. Singh, V. Singh, E. Smith, J. Smolik, P. Snopok, N. Solomey, E. Song, A. Sousa, K. Soustruznik, M. Strait, L. Suter, A. Sutton, R. Talaga, B. T. Oregui, P. Tas, R. Thayyullathil, J. Thomas, E. Tiras, D. Torbunov, J. Tripathi, A. Tsaris, Y. Torun, J. Urheim, P. Vahle, J. Vasel, P. Vokac, T. Vrba, M. Wallbank, T. Warburton, M. Wetstein, M. While, D. Whittington, D. Wickremasinghe, S. Wojcicki, J. Wolcott, A. Y. Dombara, K. Yonehara, S. Yu, Y. Yu, S. Zadorozhnyy, J. Zalesak, Y. Zhang, and R. Z. and, "Measurement of charged-current inclusive production in the NOvA near detector", Physical Review D **107**, `10.1103/physrevd.107.112008` (2023).

[79] M. A. Acero et al. (NOvA), "Measurement of neutrino-induced neutral-current coherent π^0 production in the NOvA near detector", Phys. Rev. D **102**, 012004 (2020).

[80] M. Strait, S. Bending, K. Kephart, and P. Lukens, *Nova muon energy scale systematic*, 2019.

[81] H. Faissner et al., “Observation of Neutrino and Anti-neutrino Induced Coherent Neutral Pion Production Off ^{27}Al”, Phys. Lett. B **125**, 230–236 (1983).

[82] E. Isiksal, D. Rein, and J. G. Morfın, “Evidence for neutrino- and antineutrino-induced coherent π^0 production”, Phys. Rev. Lett. **52**, 1096–1099 (1984).

[83] F. Bergsma, J. Dorenbosch, J. V. Allaby, U. Amaldi, G. Barbiellini, W. Flegel, L. Lanceri, M. Metcalf, C. Nieuwenhuis, J. Panman, C. Santoni, K. Winter, I. Abt, J. Aspiazu, F. W. Büsser, H. Daumann, P. D. Gall, T. Hebbeker, F. Niebergall, P. Schütt, P. Stähelin, P. Gorbunov, E. Grigoriev, V. Khovansky, A. Rosanov, A. Baroncelli, L. Barone, B. Borgia, C. Bosio, A. Capone, M. Diemoz, U. Dore, F. Ferroni, E. Longo, L. Luminari, P. Monacelli, F. de Notaristefani, L. Tortora, and V. Valente, “Measurement of the cross section of coherent π^0 production by muon-neutrino and antineutrino neutral-current interactions on nuclei”, Physics Letters B **157**, 469–474 (1985).

[84] H. J. Grabosch et al. (SKAT), “COHERENT PION PRODUCTION IN NEUTRINO AND ANTI-NEUTRINO INTERACTIONS ON NUCLEI OF HEAVY FREON MOLECULES”, Z. Phys. C **31**, 203 (1986).

[85] P. Marage et al. (BEBC WA59), “Coherent Single Pion Production by Anti-neutrino Charged Current Interactions and Test of PCAC”, Z. Phys. C **31**, 191–197 (1986).

[86] P. Marage et al. (BEBC WA59), “Coherent Production of π^+ Mesons in Neutrino - Neon Interactions”, Z. Phys. C **43**, 523–526 (1989).

[87] S. Willocq, M. Aderholz, H. Akbari, P. P. Allport, S. K. Badyal, H. C. Ballagh, M. Barth, H. H. Bingham, E. B. Brucker, R. A. Burnstein, R. J. Cence, T. K. Chatterjee, E. F. Clayton, G. Corrigan, D. De Prospo, Devanand, E. De Wolf, P. J. W. Faulkner, H. Foeth, W. B. Fretter, V. K. Gupta, J. Hanlon, G. Harigel,

F. A. Harris, P. Jacques, V. Jain, G. T. Jones, M. D. Jones, T. Kafka, M. Kalelkar, J. M. Kohli, E. L. Koller, R. J. Krawiec, M. Lauko, J. E. Lys, P. Marage, R. H. Milburn, I. S. Mittra, M. M. Mobayyen, J. Moreels, D. R. O. Morrison, G. Myatt, P. Nailor, R. Naon, A. Napier, D. Passmore, M. W. Peters, V. Z. Peterson, R. Plano, N. K. Rao, H. A. Rubin, J. Sacton, S. S. Sambyal, N. Schmitz, J. Schneps, J. B. Singh, S. Singh, W. Smart, P. Stamer, K. E. Varvell, L. Verluyten, H. Wachsmuth, S. Wainstein, and G. P. Yost, “Coherent production of single pions and ρ mesons in charged-current interactions of neutrinos and antineutrinos on neon nuclei at the fermilab tevatron”, Phys. Rev. D **47**, 2661–2674 (1993).

[88] D. Geiregat et al. (CHARM-II), “First observation of neutrino trident production”, Phys. Lett. B **245**, 271–275 (1990).

[89] M. Hasegawa et al. (K2K), “Search for coherent charged pion production in neutrino-carbon interactions”, Phys. Rev. Lett. **95**, 252301 (2005).

[90] A. Aguilar-Arevalo, C. Anderson, A. Bazarko, S. Brice, B. Brown, L. Bugel, J. Cao, L. Coney, J. Conrad, D. Cox, A. Curioni, Z. Djurcic, D. Finley, B. Fleming, R. Ford, F. Garcia, G. Garvey, C. Green, J. Green, T. Hart, E. Hawker, R. Imlay, R. Johnson, G. Karagiori, P. Kasper, T. Katori, T. Kobilarcik, I. Kourbanis, S. Koutsoliotas, E. Laird, S. Linden, J. Link, Y. Liu, Y. Liu, W. Louis, K. Mahn, W. Marsh, P. Martin, G. McGregor, W. Metcalf, P. Meyers, F. Mills, G. Mills, J. Monroe, C. Moore, R. Nelson, V. Nguyen, P. Nienaber, J. Nowak, S. Ouedraogo, R. Patterson, D. Perevalov, C. Polly, E. Prebys, J. Raaf, H. Ray, B. Roe, A. Russell, V. Sandberg, R. Schirato, D. Schmitz, M. Shaevitz, F. Shoemaker, D. Smith, M. Soderberg, M. Sorel, P. Spentzouris, I. Stancu, R. Stefanski, M. Sung, H. Tanaka, R. Tayloe, M. Tzanov, R. V. de Water, M. Wascko, D. White, M. Wilking, H. Yang, G. Zeller, and E. Zimmerman, Physics Letters B **664**, 41–46 (2008).

[91] K. Hiraide, J. L. Alcaraz-Aunion, S. J. Brice, L. Bugel, J. Catala-Perez, G. Cheng, J. M. Conrad, Z. Djurcic, U. Dore, D. A. Finley, A. J. Franke, C. Giganti, J. J. Gomez-Cadenas, P. Guzowski, A. Hanson, Y. Hayato, G. Jover-Manas, G. Karagiorgi, T. Katori, Y. K. Kobayashi, T. Kobilarcik, H. Kubo, Y. Kurimoto, W. C. Louis, P. F. Loverre, L. Ludovici, K. B. M. Mahn, C. Mariani, S. Masuike, K. Matsuoka, W. Metcalf, G. Mills, G. Mitsuka, Y. Miyachi, S. Mizugashira, C. D. Moore, Y. Nakajima, T. Nakaya, R. Napora, P. Nienaber, V. Nguyen, D. Orme, M. Otani, A. D. Russell, F. Sanchez, M. H. Shaevitz, T.-A. Shibata, M. Sorel, R. J. Stefanski, H. Takei, H.-K. Tanaka, M. Tanaka, R. Tayloe, I. J. Taylor, R. J. Tesarek, Y. Uchida, R. V. de Water, J. J. Walding, M. O. Wascko, H. White, M. J. Wilking, M. Yokoyama, G. P. Zeller, and E. D. Zimmerman, "Search for charged current coherent pion production on carbon in a few-GeV neutrino beam", Physical Review D **78**, `10.1103/physrevd.78.112004` (2008).

[92] C. T. Kullenberg et al. (NOMAD), "A Measurement of Coherent Neutral Pion Production in Neutrino Neutral Current Interactions in NOMAD", Phys. Lett. B **682**, 177–184 (2009).

[93] Y. Kurimoto et al. (SciBooNE), "Improved Measurement of Neutral Current Coherent π^0 Production on Carbon in a Few-GeV Neutrino Beam", Phys. Rev. D **81**, 111102 (2010).

[94] M. A. Ramırez et al. (MINERvA), "Neutrino-induced coherent π^+ production in C, CH, Fe and Pb at $<E_\nu> \sim 6$ GeV", (2022).

[95] C. Andreopoulos, C. Barry, S. Dytman, H. Gallagher, T. Golan, R. Hatcher, G. Perdue, and J. Yarba, "The GENIE Neutrino Monte Carlo Generator: Physics and User Manual", (2015).